Department of Physics and Astronomy

University of Heidelberg

Master thesis

in Physics

submitted by

Marc Schuh

born in Bergisch Gladbach

2014

Simulations of the electrostatic and magnetic field properties and tests of the Penning-ion source at THe-Trap

This Master thesis has been carried out by Marc Schuh

at the

Max-Planck-Institut für Kernphysik, Heidelberg

under the supervision of

Herrn Prof. Dr. Klaus Blaum

Simulationen der elektrostatischen und magnetischen Feldeigenschaften und Tests der Penning-Ionenquelle von THe-Trap:

Das Experiment Tritium-Helium-Trap (THe-Trap) ist ein Penning-Fallen-Massenspektrometer, entworfen um das Massenverhältnis von Tritium und Helium-3 mit einer relativen Genauigkeit von 10^{-11} zu bestimmen. Um diese Genauigkeit zu erreichen, müssen die Eigenschaften der Penning-Falle sehr gut verstanden sein. Geometrische Abweichungen vom Idealfall verursachen Terme höherer Ordnung im elektrostatischen Potential. Ausführliche Simulationen wurden durchgeführt, um zuerst die Abhängigkeit des Simulationswerkzeuges Comsol-Multiphysics von der gewählten Auflösung zu testen und dann die Terme höherer Ordnung zu quantifizieren. Die Simulationen waren erfolgreich und in guter Übereinstimmung mit den experimentellen Beobachtungen. Es war auch möglich den Spiegelladungseffekt zu simulieren. Der simulierte Spiegelladungseffekt bestätigt den experimentellen Wert. Ähnliche Untersuchungen wurden durchgeführt, um den Einfluss des experimentellen Aufbaus auf das Magnetfeld zu untersuchen. Die Einflüsse von ferromagnetischen Materialien konnten verlässlich bestimmt werden.
Der letzte Teil dieser Arbeit befasst sich mit der Charakterisierung der externen Penning-Ionenquelle. Hierfür wurde ein neuer Faraday-Becher entworfen und eingebaut. Das neue Gerät konnte den Ionenstrom der Penning-Ionenquelle messen und half ihre Betriebsparamter zu optimieren.

Simulations of the electrostatic and magnetic field properties and tests of the Penning-ion source at THe-Trap:

The Tritium-Helium-Trap (THe-Trap) is a Penning-trap mass spectrometer dedicated to measure the mass ratio of tritium and helium-3 with a relative precision of 10^{-11}. To reach this precision, the properties of the Penning-trap must be understood very well. Geometrical deviations from the ideal case cause higher-order components in the electrostatic potential. Extended simulations have been carried out to investigate first the dependence of the simulation tool Comsol Multiphysics on the resolution chosen and then to quantify the higher-order terms. The simulations were successful and in good agreement with the experimental observations. It was also possible to simulate the image charge effect. The simulated image charge effect confirms the experimental value. Similar investigations were performed to estimate the influence of the experimental setup on the magnetic field. The influence of ferromagnetic materials was determined reliably.
The final part of this thesis is the characterization of the external Penning-ion source. For this, a new Faraday cup was designed and implemented. The new device can measure an ion beam from the Penning-ion source and helps to improve their operating parameters.

Contents

List of Figures

List of Tables

Chapter 1

Introduction

Mass is a fundamental property and knowing an object's mass is crucial in every branch of physics. In everyday life, mass is usually measured via the gravitational force, for example by using bathroom or kitchen scales. Since the gravitational force is the product of mass and earth acceleration, the mass can be determined. Unfortunately, this method cannot be applied to single atoms, because the force measurement is not sensitive enough. But in atomic and nuclear physics the masses of single particles are needed.

A different mass measurement technique was developed by J. J. Thomson [Tho99], who measured the charge-to-mass ratio of atomic ions and molecular ions for the first time in 1897. In his apparatus, charged particles are accelerated and deflected by a combination of magnetic and electric fields. The angle of deflection is proportional to the charge-to-mass ratio. For this technique, Thomson was awarded the Nobel Prize in 1906. The concept of measuring a charge-to-mass ratio is still in use and has continuously improved [Dem35, Duc50, PvR58]. In the 1960's, H. G. Dehmelt developed the Penning-trap technology at the University of Washington, Seattle as a tool to store single electrons and to investigate their properties [WED73, WD75]. In 1989, together with W. Paul, he received the Nobel Prize for "The development of the ion trap technique" [Deh90, Pau90]. A Penning-trap links the charge-to-mass ratio of a particle to a frequency. A frequency is the most accurately measurable quantity. It can be measured up

to a precision of 10^{-17} and is therefore not the limiting factor for mass ratio measurements [Ger11].

Today's best mass measurements can reach a relative precision of 10^{-11} [VDJPVLZ06, Mye13]. A good overview over mass measurements around the world is given in Reference [Bla06].

Einstein's famous formula $E = mc^2$ [Ein05] links mass measurements to theoretical predictions of energy levels. High precision atomic mass measurements, for example, help to improve theories such as QED by testing the fine structure constant α [KN03] or the electron binding energy. Here Einstein's energy-mass-relation is directly used by measuring the weight of an ion at different charge states [RTM$^+$05]. Of course, mass measurements can directly check nuclear mass models [Wei35, BB36, LPT03, AWW$^+$14], which are needed in nuclear astrophysics [PKTW01, Bos03, Gor05], nuclear structure studies [Bol01, CBCM05, Hof98, HAA$^+$03], neutrino physics [BBB$^+$02, Lob03, Bor05, KBB$^+$05] and many more. But the absolute masses are not the only quantities of interest. Decay energies and particle separation energies, for instance, can be derived from the atomic mass difference of the mother and the daughter particles [EEH$^+$06, EEH$^+$08]. The energy equivalent of such a mass difference is called the Q-value. The determination of a Q-value is the main goal of the experiment presented here, the Tritium-Helium-Trap (abbreviated THe-Trap). It is dedicated to measure the Q-value of tritium with a relative precision of 10^{-6}, which means, the mass ratio of tritium and helium must be determined with a relative precision of 10^{-11}. Tritium has a half-life of 12.3 years and undergoes a β-decay to helium-3 by emitting an electron and an anti-electron neutrino [AM00]. Except for the mass of the anti-electron neutrino, the masses of all constituents are directly measurable. It is known from cosmological observations and reactor experiments that the anti-electron neutrino has a mass [KT01, FFI$^+$01, BBC$^+$01], but only an upper limit has been determined so far. The mass of the anti-electron neutrino is a crucial piece of information in many cosmological theories and one of the fundamental properties that is missing in the Standard Model. An experiment that aims for the measurement of the anti-electron neutrino mass is the Karlsruhe Neutrino Experi-

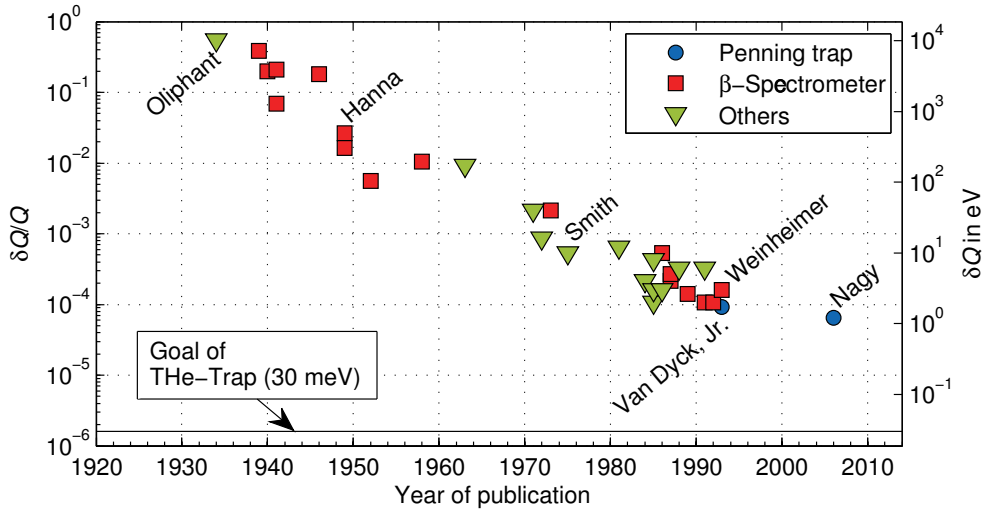

Figure 1.1: Improvements of tritium's Q-value since its discovery in 1934 [OHR34]. Most measurements are performed with β-spectrometers [HP49] and radio-frequency spectrometers, for example [SW75]. The today's most precise measurements are performed by the Penning-trap mass spectrometry method [VDJFS93, NFB$^+$06]. Figure courtesy of [Str14].

ment (KATRIN) [AKC04, Wol10, Par14]. It will also determine the Q-value of tritium. Over the last few decades, the accuracy of tritium's Q-value got improved by orders of magnitude, as it is shown in Figure 1.1. Currently, the most precise measurement is $Q = (18589.8 \pm 1.2)$ eV [NFB$^+$06], obtained at SMILETRAP [BCF$^+$02]. THe-Trap aims to lower the uncertainty of the Q-value to 30 meV in order to provide a consistency check for KATRIN. To reach this goal, a precise understanding of the properties of THe-trap is essential.

In this thesis three main topics are discussed. The first is about simulating the electrostatic properties of the Penning-trap used in THe-Trap. For this, extended simulation studies are performed, and results concerning the shape of the electrostatic potential are derived (Chapter 4). The finite element simulation tool used, Comsol Multiphysics, is validated, and the effect of uncertainties in the simulated model of THe-Trap is investigated. The results obtained with Comsol Multiphysics are compared with those from simulations with Tosca Vector Fields Opera, which also uses the finite element method.

Additionally, the image charge effects in a real Penning-trap are investigated in a simulation. In the second topic (Chapter 5), the magnetic field properties of THe-Trap are studied. The materials in the experimental setup have some magnetic susceptibility. The effect on the homogeneity of the magnetic field is simulated to quantify the deviations from the uniform magnetic field. The last part of this thesis is about the external Penning-ion source available at THe-Trap. The Penning-ion source is designed to create ions from gas at relatively low pressure of 10^{-6} mbar. In December 2013, a new cathode was installed. To test this cathode, as well as to optimize the Penning-ion source, while it is mounted at the experiment, a Faraday cup was designed and installed within this thesis. The Faraday cup is also supposed to work as a gas barrier so that less rest gas from the Penning-ion source contaminates the vacuum of the Penning-trap. The results of the tests with the new cathode and the progress in optimizing the Penning-ion source with the new Faraday cup are given in Chapter 6.

Chapter 2

Theory of Penning-traps

This chapter gives an overview of the underlying physics of the ideal and real Penning-trap (see Sections 2.1 and 2.2, respectively). Since the real Penning-trap always deviates from the ideal case these deviations have to be quantified and the effect on the mass measurement has to be investigated. The strength of the deviations of the electrostatic potential and the magnetic field is determined by finite element simulations. The concept of the finite element simulations used here is presented in Section 2.3.

2.1 Ideal Penning-trap

An ideal Penning-trap consists of a homogeneous magnetic field and a pure electrostatic quadrupole potential. The Penning-trap can be used to determine the mass of a particle by linking it to its characteristic oscillation frequency. In a pure magnetic field this frequency is called cyclotron frequency. In most cases, a mass ratio of particles is measured and hence only their frequency ratio is of interest. As mentioned in the introduction, the most precisely measurable quantity is a frequency. Today's best frequency standards can reach a relative stability of 10^{-15} [Ger11]. To compare two frequencies, which are measured at different times, the reference has to be stable over time. With today's commercially available frequency standards, which have a relative stability of better than 10^{-12} on a time scale of a few seconds [Str14], this is not a limitation for the

mass (ratio) measurement that take up to a few ten or hundred seconds.

To make the charged particle oscillate and to be able to determine its oscillation frequencies, the ion motion must be confined in all three spatial dimensions. The radial confinement is due to the magnetic field. If a charged particle is moving with a velocity $\vec{v}$ perpendicular to a homogeneous and time independent magnetic field $B_0\vec{e}_z$ in absence of an external electric field it experiences the Lorentz force. The resulting circular movement of the particle is called free space cyclotron frequency

$$\nu_c = \frac{1}{2\pi}\frac{q}{m}B_0 \quad , \tag{2.1}$$

where $q = ne$ is the total charge of the ion, with n the charge state, e the elementary charge and m the mass of the ion. Provided that B_0 is known, the $\frac{q}{m}$ ratio can be determined from the measured frequency. Since n is a quantized parameter and usually known, it is the elementary charge and B_0 that remain to be determined. Even though the elementary charge is known to a precision of 10^{-8} [Kar08], this is not sufficient enough for the desired precision in a Penning-trap. Also B_0 cannot be determined reliably enough. Hence, mass-ratios are measured, where the magnetic field B_0 and the elementary charge e cancels out.

Unfortunately, confining a charged particle to a plane perpendicular to the magnetic field $B_0\vec{e}_z$ is not enough, because any velocity in direction of the magnetic field will cause the loss of the particle. Earnshaw's theorem [Ear42] proves that it is impossible to store a charged particle in a purely homogeneous and constant magnetic or purely electrostatic electrostatic potential. Therefore, in a Penning-trap a constant and homogeneous magnetic field is combined with an electrostatic quadrupole potential. The electrostatic quadrupole potential confines the movement along the z-axis and leads to a harmonic oscillation which is independent of the axial amplitude. In the radial direction, the movement is confined by the magnetic field $B_0\vec{e}_z$. The electric field inside the Penning-trap is generated by hyperbolic electrodes (see Figure 2.1), where a voltage V_0 is applied between the endcap electrodes and ring electrode. It is also assumed that

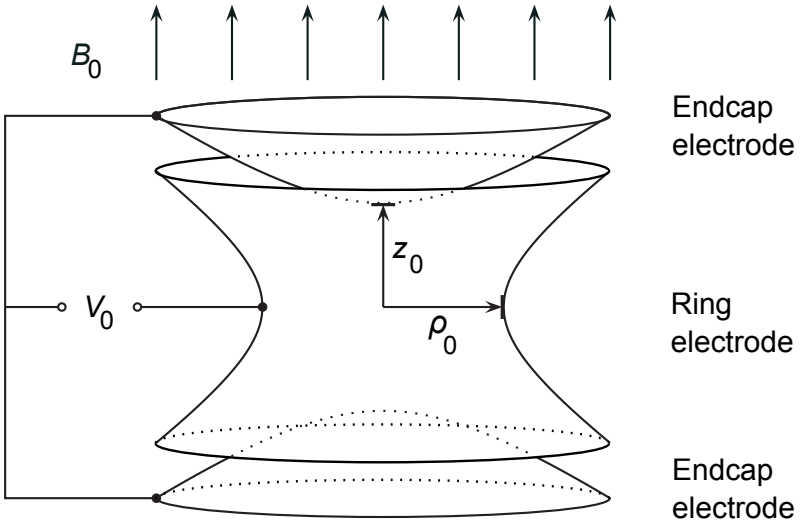

Figure 2.1: Sketch of an ideal hyperbolic Penning-trap. It consists of a hyperbolically shaped ring and two endcap electrodes. To be ideal the electrodes must extend to infinity. B_0 shows the direction of the magnetic field. Figure courtesy of [Str14].

the region inside of the electrodes is free of charge. Hence, it can be described by the Laplace equation [Jac62] for an electrostatic potential Φ

$$\Delta\Phi(x, y, z) = 0 \quad . \tag{2.2}$$

Assuming ideal electrodes which are extended to infinity, these electrodes are equipotential planes of the electrostatic quadrupole potential. Therefore, no higher-order terms than the harmonic order are expected. The general harmonic potential has a form of

$$\Phi(x, y, z) = \Phi_0 + \left(ax^2 + by^2 + cz^2\right) \tag{2.3}$$

with Φ_0 as a constant potential. To solve the Laplace equation $a + b + c$ has to equal zero and to obtain a cylindrical symmetric quadrupole potential $a = b = -\frac{c}{2}$, this leads

to

$$\Phi(x,y,z) = \Phi_0 - c\left(\frac{x^2+y^2}{2} - z^2\right) \quad . \tag{2.4}$$

Hence, the electrode must be hyperbolic (see Figure 2.1) which makes the surfaces of the electrodes to be equipotential surfaces in the quadrupole potential. Introducing the characteristic trap dimension

$$d = \frac{1}{2}\sqrt{2z_0^2 + \rho_0^2} \quad , \tag{2.5}$$

where z_0 and ρ_0 are the distances from the trap center to the endcap and ring electrodes, respectively, and inserting the boundary conditions displayed in Figure 2.1 results in a potential

$$\Phi(x,y,z) = \Phi_0 - \frac{V_0\tilde{C}_2}{2d^2}\left(\frac{x^2+y^2}{2} - z^2\right) \quad . \tag{2.6}$$

The boundary conditions are that the surfaces of the electrodes are equipotential surfaces of a quadrupole potential. $\tilde{C}_2$ is a dimensionless coefficient which scales the quadrupole potential depending on the shape of the electrodes. For an ideal Penning-trap $\tilde{C}_2$ is equal to 1. The basis for the equation of motion for a charged particle in a Penning-trap is again the Lorentz force

$$\vec{F} = q\left(\vec{E} + \dot{\vec{r}} \times \vec{B}\right) \quad , \tag{2.7}$$

where $\vec{E}$ is the electrostatic field, derived from the potential via $\vec{E} = -\vec{\nabla}\Phi$. The magnetic field $\vec{B}$ is $\vec{B} = B_0\vec{e}_z$. Using Newton's second law [NH14] on Equation (2.7) leads to

$$\begin{pmatrix} \ddot{x} \\ \ddot{y} \\ \ddot{z} \end{pmatrix} = \frac{qB_0}{m}\begin{pmatrix} \dot{y} \\ -\dot{x} \\ 0 \end{pmatrix} + \frac{qV_0\tilde{C}_2}{2md^2}\begin{pmatrix} x \\ y \\ -z \end{pmatrix} \quad . \tag{2.8}$$

The way of solving this differential equation is well described in for example [BG86]. The resulting eigenfrequencies are

$$\nu_z = \frac{1}{2\pi}\sqrt{\frac{qV_0R_2}{md^2}} \quad , \tag{2.9}$$

$$\nu_\pm = \frac{1}{2}\left(\nu_c \pm \sqrt{\nu_c^2 - 2\nu_z^2}\right) \quad . \tag{2.10}$$

In order to store the particle, the frequencies have to be real. Hence, for a stable motion $\nu_c > \sqrt{2}\nu_z$ and $qV_0R_2 > 0$ which are called the stability criteria. These frequencies are called axial frequency, ν_z, modified cyclotron frequency, ν_+, and magnetron frequency, ν_-. Summing the three eigenfrequencies calculated above in quadrature leads back to the free space cyclotron frequency [BG86]

$$\nu_z^2 + \nu_+^2 + \nu_-^2 = \nu_c^2 = \left(\frac{1}{2\pi}\frac{qB_0}{m}\right)^2 \quad . \tag{2.11}$$

This relation is also called Brown–Gabrielse invariance theorem, since 1986 when it was discovered by Lowell Brown and Gerald Gabrielse . Typically at THe-Trap ν_- is in the range of a few 100 kHz, ν_z at 4 MHz and ν_+ between 24 – 80 MHz. Hence the following hierarchy between the frequencies is given $\nu_c \approx \nu_+ \gg \nu_z \gg \nu_-$.

2.2 Real Penning-traps

No matter how well a Penning-trap is designed, there will always be deviations from the ideal Penning-trap. Deviations are based on technical reasons, for example that the electrodes are not infinitely large, nor is their shape perfectly hyperbolic. Some deviations are introduced on purpose, like the endcap electrodes may have holes for the ion transfer into the trap. The homogeneous magnetic field is for example disturbed by the magnetic susceptibilities of the materials used. Deviations from the ideal situation can be quantified analyzing higher-order terms of the polynomial approximation of the fields. The real shape of the electrostatic potential and magnetic field is obtained

from simulations and the higher-order coefficients of the polynomial approximation are obtained from fits. When the frequencies of the ion motion are measured to a precision of 10^{-11}, even small deviations from the ideal case become visible in the measurement and can have a significant impact on the measured frequency. This section treats the deviations of a real hyperbolic Penning-trap by showing how they are described and by explaining how these deviations influence the trap frequencies.

2.2.1 Electrostatic potential

The above described deviations of the real from the ideal Penning-trap make it necessary to introduce higher-order components to the harmonic potential (see Equation (2.6)) to describe the real electrostatic potential. If present, these higher-order imperfections shift the frequencies of the motions, but compared to the base frequencies the frequency shifts are usually very small. For parametrizing the imperfection of the electrostatic potential the solutions of the Laplace equation are taken [KEH+14]

$$\Phi_n(r,\theta) = R_n V_{\text{Ring}} r^n P_n(\cos(\theta)) \tag{2.12}$$

where n is a non-negative integer, $P_n(\cos(\theta))$ a Legendre polynomial, R_n gives the strength of the higher-order terms of the electrostatic potential generated by the ring electrode and V_{Ring} is the voltage applied to the ring electrode. For the parametrization, it is also assumed that the imperfections are cylindrically symmetric. This is a valid approximation, because the electrodes are cylindrically symmetric and all their deviations, for example finite space or holes in the endcap electrodes do not violate this symmetry. To describe the whole electrostatic potential, including higher-order deviations from the ideal case, the following function is chosen

$$\Phi_{\text{Ring}}(r,\theta) \approx \sum_{n=0}^{n_{\max}} R_n V_{\text{Ring}} r^n P_n(\cos(\theta)) \quad , \tag{2.13}$$

where $n_{\max}$ gives the highest chosen order to approximate the real electrostatic potential. The parameter $n_{\max}$ is in the scope of this work between six and ten. In this work, the contribution of the ring electrode to the electrostatic potential is denoted with R_n coefficients, where n is the power of the corresponding polynomial approximation. It should be noted that the R_n have a unit of length^{-n}. In this thesis the unit is mm^{-n}. To be consistent with other publications, where these coefficients are dimensionless, they have to be transformed the following way

$$\tilde{R}_n = 2d^n R_n \quad , \tag{2.14}$$

where d is the characteristic trap dimension given in Equation (2.5) and $\tilde{R}_n$ the dimensionless ring coefficient.

The electrostatic potentials of the other electrodes (see Chapter 3) are approximated in the same way. The coefficients related to the guard electrodes are denoted with D_n, for the endcap electrodes with E_n and for the skimmer electrodes with S_n. Finally, contributions from all electrodes are summed up to get the full potential

$$\Phi_{\text{tot}} = \Phi_{\text{Ring}} + \Phi_{\text{Guards}} + \Phi_{\text{Endcaps}} + \Phi_{\text{Skimmers}} \quad . \tag{2.15}$$

The final coefficient which describes the strength of the higher-order terms in the total potential containing the contribution of all electrodes is denoted with C_n and consists of

$$C_n V_0 = R_n V_{\text{Ring}} + D_n V_{\text{Guards}} + E_n V_{\text{Endcaps}} + S_n V_{\text{Skimmers}} \quad , \tag{2.16}$$

where for example R_n and D_n are voltage independent, the resulting C_n is not and hence the total potential can be tuned by setting different voltages to the electrodes. A direct connection between V_{Ring} or any voltage applied to a single electrode and V_0 is difficult, because V_0 can be given only in dependency of all other applied voltages. Also, $C_n V_0$ are directly connected to each other and cannot be calculated individually.

If the coefficient C_n with $n > 2$ is unequal to zero, this leads to amplitude dependent frequency shifts. These are explained in Reference [KEH+14].
In the following, a few characteristic electrostatic parameters for the trap are introduced. The first is the guard constant, c_{guard} which is the ratio of the changes in voltage applied to the ring and guard electrode, to keep the harmonic part of the trap constant. If the ring voltage is shifted and the electrostatic quadrupole potential should not change, the following equation should hold

$$V_{\text{Ring}} R_2 + V_{\text{Guard}} D_2 \stackrel{!}{=} \left(V_{\text{Ring}} + \Delta V_{\text{Ring}}\right) R_2 + \left(V_{\text{Guard}} + \Delta V_{\text{Guard}}\right) D_2 \tag{2.17}$$

$$\Rightarrow \frac{\Delta V_{\text{Guard}}}{\Delta V_{\text{Ring}}} = -\frac{\mathrm{R_2}}{\mathrm{D_2}} =: c_{\text{Guard}} \tag{2.18}$$

where V_{Ring} and V_{Guard} are the voltages applied to the ring and guard electrodes, respectively, and ΔV_{Guard} and ΔV_{Ring} are their changes. It is worth noting that a trap, where D_2 is equal to zero, is called orthogonal, because a change in V_{Guard} does not change the C_2-coefficient. The main intention of the guard electrodes is to cancel out higher-order field components resulting from deviations to the ideal trap, usually R_4. Therefore, the optimal voltage is defined as

$$V_{\text{Guard}} = -\frac{R_4}{D_4} V_{\text{Ring}} \quad . \tag{2.19}$$

But also higher than fourth-order terms occur and since the ratio of for example R_4/D_4, R_6/D_6, ... is not the same, the resulting C_n cannot be zero for all n, but at least C_4 can be minimized.

2.2.2 Magnetic field

As mentioned in Section 2.1, the magnetic field in the ideal Penning-trap is homogeneous and stable. Unfortunately, it is technically very challenging to construct a magnetic field that is uniform and additionally constant at a 10^{-11} level for minutes or hours. Also, a magnetic field can never be shimmed to be perfectly homogeneous.

Higher-order terms in the magnetic scalar potential Ψ can be described similarly by Legendre polynomials [KEH+14]

$$\Psi_n(r,\theta) = -\frac{B_n}{n+1} r^{n+1} P_{n+1}\left(\cos(\theta)\right) \quad , \tag{2.20}$$

where the B_n's give the strength of the higher-order distortion, like in Section 2.2.1 and again the deviations of the magnetic potential from the uniform case are assumed to be cylindrically symmetric. The magnetic field is given by the negative gradient of the potential $\vec{B}_n(\rho,z) = -\vec{\nabla}\Psi_n$. This calculation is performed in Reference [KEH+14] and the axial component of the magnetic field turns out to be

$$B^{(z)}(\rho,z) = B_n \sum_{k=0}^{\lfloor n/2 \rfloor} \frac{(-1)^k}{2^{2k}} \frac{n!}{(n-2k)!(k!)^2} z^{n-2k} \rho^{2k} \tag{2.21}$$

The upper limit of the sum is defined by the floor function

$$\left\lfloor \frac{n}{2} \right\rfloor = \begin{cases} \frac{n}{2} & \text{if } n \text{ is even,} \\ \frac{n-1}{2} & \text{if } n \text{ is odd.} \end{cases}$$

The coefficients B_n must be the same for the axial and radial component of the magnetic field, to obey Maxwell's equation. $\vec{\nabla} \cdot \vec{B} = 0$ is valid in every case and because there are no currents in the center of the trap except for the moving ion, whose magnetic influence is negligible, $\vec{\nabla} \times \vec{B} = 0$ holds true as well. Therefore, it is enough to determine these coefficients for one component. The radial component of the magnetic field as well as the full derivation is given in Reference [KEH+14]. Also in Reference [KEH+14] the resulting amplitude dependent first order frequency shift can be found, if B_n is unequal to zero for $n > 0$.

2.2.3 Image charge shift

One frequency shift which is not based on imperfections of the magnetic field or the electrostatic potential, is caused by image charge effects. In Section 2.1 the space inside

the ideal Penning-trap is treated as source free, so there are no electric charges within the volume. This is of course wrong for the real Penning-trap, because the measurement concept is based on trapping a charged particle. This charged particle, confined in the trap, causes image charges on the surface of the surrounding electrodes. These image charges add an additional electrostatic potential which acts back on the charged particle and causes frequency shifts. In the following, the mathematical treatment of the image charge effect in a sphere and in a hyperbolic Penning-trap is explained which is based on Reference [Ket14].

The image charge frequency shift was estimated for the first time for hyperbolic Penning-trap electrodes in Reference [VDJMFS89]. The problem itself is not to calculate the actual frequency shift, but to know how the electrostatic field generated by the image charge looks like. In Reference [VDJMFS89], the Penning-trap electrodes were approximated by a sphere with a radius of ρ_0, while ρ_0 is used as defined in Figure 2.1. The analytic solution of the field created by the image charge inside a sphere at the location of the point like charge is

$$E_{\text{image}}(r) = \frac{1}{4\pi\epsilon_0} \frac{qar}{\left(a^2 - r^2\right)^2} \quad , \tag{2.22}$$

where $r = |\vec{r}|$ is the distance of the point-like charge from the center of the sphere and ϵ_0 the vacuum permittivity. The parameter a is the radius of the sphere and $q = ne$ is the total charge of the ion, where n is an integer and e the elementary charge. The image charge field is spherically symmetric. Hence, without loss of generality, the field along the x-axis is from now on discussed. For an easier treatment and to compare the results obtained later, Equation (2.22) is approximated by a Taylor expansion to the n-th order along the x-axis

$$E_{\text{image}}(x) \approx \frac{q}{4\pi\epsilon_0} \sum_{k=1}^{n} k \frac{x^{2k-1}}{a^{2k+1}} = \frac{q}{4\pi\epsilon_0 a^2} \left(\frac{x}{a} + 2\frac{x^3}{a^3} + 3\frac{x^5}{a^5} + \dots \right) \quad . \tag{2.23}$$

If the sphere radius $a \gg |x|$, then the image charge shift is proportional to the displacement of the ion in any direction, like Hooke's law [Dem05], but here the force is not

acting back to the center but pushes the ion towards the electrode. Therefore, the image charge field in a sphere can be approximated by a Taylor series to the first order

$$E_{\text{image}}(x) \approx \frac{q}{4\pi\epsilon_0 a^3} x = n\mathcal{E}_x x \quad , \tag{2.24}$$

where $q = ne$ and $\mathcal{E}_x = \frac{e}{4\pi\epsilon_0 a^3}$.
The real image charge field inside of a hyperbolic Penning-trap violates spherical symmetry, because the electrodes are not spherical symmetric. This leads to the fact that the prefactor $\mathcal{E}_x$ which is used in the sphere-case, cannot be used further in the hyperbolic Penning-trap case. Hence, the image charge field needs to be approximated in the different directions individually

$$\vec{E}_{\text{image}}(x, y, z) = n\left(\mathcal{E}_x x\vec{e}_x + \mathcal{E}_y y\vec{e}_y + \mathcal{E}_z z\vec{e}_z\right) \quad , \tag{2.25}$$

where the $\mathcal{E}_i$ are the individual electrostatic field gradients. They represent the electric field gradient of one positive elementary charge. This approximated field for the hyperbolic electrodes looks in principle like the field in the sphere and follows the concept that the image charge field is proportional to the displacement of the ion from the center. Higher-order terms are present in reality as well when the amplitude of the motion becomes comparable to the distance of the electrodes, but they are suppressed by small motional amplitudes. Due to the small effect, around 10^{-10}, on the frequencies of the ion motion only the linear term is treated. This term does not vanish in the limit of small amplitudes. In contrast to Equation (2.23), where an analytical solution for the prefactors exists, here the $\mathcal{E}_i$'s must be determined otherwise. Later, they are calculated by a finite element simulation. This opens the opportunity to take the geometry of hyperbolic electrodes, including deviations from the ideal shape into account. The electrostatic field component of the image charge effect should be the same in the x- and y-direction as the Penning-trap electrodes are cylindrically symmetric. Therefore, the following can be defined $\mathcal{E}_\rho \equiv \mathcal{E}_x = \mathcal{E}_y$. Using Newton's second law leads to an

additional term

$$n\frac{q}{m}\mathcal{E}_\rho \begin{pmatrix} x \\ y \end{pmatrix} \tag{2.26}$$

in the radial equation of motion. Assuming the image charge causes a perturbation ϵ_ρ, this changes the radial equation of motion (see Equation (2.8)) to

$$\begin{pmatrix} \ddot{x} \\ \ddot{y} \end{pmatrix} = \omega_\mathrm{c} \begin{pmatrix} \dot{y} \\ -\dot{x} \end{pmatrix} + \frac{\omega_z^2\left(1+\epsilon_\rho\right)}{2} \begin{pmatrix} x \\ y \end{pmatrix} \quad , \tag{2.27}$$

where ϵ_ρ is chosen as $n\frac{2q\mathcal{E}_\rho}{m\omega_z^2}$. Using that $\left|\epsilon_\rho\right| \ll 1$ and the relation $\nu_\mathrm{c} \approx \nu_+ + \nu_-$ [BG86] finally gives a radial frequency shift of

$$\Delta\nu_\pm = \mp n\frac{\mathcal{E}_\rho}{2\pi B_0} \quad . \tag{2.28}$$

A similar ansatz is taken for the axial motion and leads to an axial frequency shift of

$$\Delta\nu_z = -n\frac{q}{m}\frac{\mathcal{E}_z}{8\pi^2\nu_z} \quad . \tag{2.29}$$

Due to the used frequency detection system which keeps the axial frequency constant (see References [PZVDJ07, Hö10, Str14]), Equation (2.28) becomes

$$\Delta\nu_\pm \approx \mp n\frac{2\mathcal{E}_\rho + \mathcal{E}_z}{4\pi B_0} \quad . \tag{2.30}$$

For mass measurements the free cyclotron frequency is needed (Equations (2.1) and (2.11)). The shift of the free cyclotron frequency, obtained by using the invariance theorem, is calculated as

$$\Delta\nu_\mathrm{c} \approx \pm\Delta\nu_\pm \quad . \tag{2.31}$$

Again, the relation $\nu_\mathrm{c} \approx \nu_+ + \nu_-$ is used. The full derivation is given in Refer-

ence [Ket14].

In general, ν_z and ν_+ decrease and ν_- increases due to the image charge shift. The image charge shift $\Delta\nu_c$ is also defined as $\nu_{c_{Real}} = \nu_{c_{Ideal}} + \Delta\nu_c$, where $\nu_{c_{Real}}$ is the by the image charge perturbed and only measurable frequency. Calculated by the invariance theorem ν_c drops below the value of the ideal trap without image charge effect.

2.3 Finite element simulation

This section gives a brief introduction to simulations with the finite element method. Many physical problems that can be described by partial differential equations (PDE), like the Maxwell equations cannot be solved analytically for every case. Often the boundary conditions are so complex that they prevent the finding of an exact solution. For example, the electrostatic potential produced by hyperbolic electrodes with finite size and holes in the endcap electrodes cannot be derived analytically. One method of obtaining an approximate solution for those PDE's is the finite element method (FEM) [GN08, Ryl13, WSV14].

The FEM is a numerical method and consists of four steps. Before the simulation starts, the problem must first be described, for example the geometry of the THe-Trap electrodes has to be modeled in a computer and the boundary conditions like the applied voltages have to be set. Then, the geometry of the problem is divided in many small subdomains. This is called meshing. The quality of the approximation of the geometry by the mesh depends on the selected mesh size. This leads to the term "resolution" in the simulation. The finer the mesh, the higher the resolution is. Hence, the resolution is proportional to the inverse of the mesh size. Next, all mesh cells are connected to each other obeying the globally set boundary conditions, like the voltages at the electrodes and the boundary conditions to the neighboring cells. This leads to an equation system and is presented in a matrix $\mathcal{A}$. The dimension of $\mathcal{A}$ is $n \times n$, where n is the number of mesh cells. The last step is solving this equation system. This is the most time-consuming step. The matrix $\mathcal{A}$ becomes very large because, in the simulation here,

often meshes with a million cells or more are used. Due to the fact that the direct boundary conditions only affect the neighboring cells the matrix is a so called sparse matrix. Depending on its size and dimension different methods for solving this equation system can be applied. These are for example the Gaussian elimination for solving a linear equation directly, or the conjugate gradient method and generalized minimal residual method as iterative solvers [PTVF92, EM07]. Here, in the performed simulation only a direct solver is applied. This avoids that the simulation result also depends on the step size of the iterative solver, apart from the resolution of the simulation.

Developing a piece of software which offers an easy way of implementing the geometry of THe-Trap and which has efficient algorithms to create and solve the equation system would have been impossible within the time frame of this thesis. Fortunately, there already exists a piece of software designed for these purposes, Comsol Multiphysics. It is a commercially available tool which allows to import external Computer-Aided Design (CAD) models and to create new models directly in a graphical user interface. For the electrostatic potential and magnetic field simulation packages are available, where the boundary conditions, like voltages, charges, magnetic field and many more can be set in an easy way. After the simulation, the result can be displayed in plots directly in Comsol Multiphysics, and these plot can be saved as a picture, or the mesh including the coordinates and the simulated values (electrostatic potential, electric field strength etc.) can be exported and analyzed further by external tools. More information is given in Reference [Com14b].

Chapter 3

Experimental setup THe-Trap

This chapter explains the experimental setup of THe-Trap. In Section 3.1 an overview of how THe-Trap looks like in general is given. Also the deviations of the real trap electrodes from the ideal trap electrodes are introduced. The materials with different thermal shrinking coefficients and magnetic susceptibilities used are denoted. These different shrinking coefficients lead to relative changes in the position of the electrodes when the experiment is cooled down to 4 K. The materials used also have magnetic susceptibilities that deviate from the susceptibility of vacuum and hence cause magnetic distortions. Section 3.2 presents the external Penning-ion source. This source can be used to generate ions of any gaseous element outside of the actual Penning-trap electrodes. In Section 3.3 the custom-designed Faraday cup is presented. This Faraday cup was designed for analyzing and optimizing the Penning-ion source, while it is mounted at the experiment. It is also designed to reduce the gas flow from the Penning-ion source to the actual Penning-trap electrodes.

3.1 THe-Trap

Tritium-Helium-Trap was designed at the University of Washington, Seattle, and shipped to the Max-Planck-Institut für Kernphysik in Heidelberg in 2008 [VDJPVLZ06]. It is dedicated to measure the mass ratio of tritium and helium-3 with a precision of

10^{-11}. An overview of the experimental setup is shown in Figure 3.1. THe-Trap consists of a part that is operated at room temperature which starts at the electrical connections and goes to the top. The parts below the electrical connections are located inside a magnet charged to 5.26 T. This part contains the trap chamber with the hyperbolic Penning-trap electrodes and the cryogenic electronics which are cooled down to 4 K. A more detailed sketch of the contents of the trap chamber is displayed in Figure 3.2. The trap chamber contains an ion capture segment and two Penning-traps. The ratio of ρ_0/z_0 describes ratio of the distance from the center to the ring- and endcap electrode, respectively and should be 1.16 in the ideal case [BG86], but it is 1.22. Furthermore, the holes in the endcap electrodes for injecting and ejecting the ions are deviating from the ideal shape, too. These imperfection lead to higher-order terms in the electrostatic potential (see Section 2.2.1). To tune the electrostatic potential guard electrodes are used. The guard electrodes are radially cut in half (not shown in Figure 3.2). This allows to insert radio frequencies for manipulating, exciting and especially for coupling the radial to the axial motion of the ion [SBB$^+$91, KBK$^+$95]. The skimmer electrodes shown protect the vacuum from rest gas at the Penning-ion source and reflect the electron beam created by the field emission point (FEP). This electron beam is used to create ions in the actual Penning-trap. In general, there are two methods available to load ions in the trap. Commonly the FEP that is located below the experiment trap is used. For this, a high voltage is applied to the FEP and a voltage between FEP, and EbSkim accelerates the emitted electrons to the experiment trap. They are reflected at the EtSkim electrode. Since the generated electron beam does not stay fully focused, it also hits the endcap electrodes. There, atoms from the rest gas that are frozen on the electrodes are released and can be ionized by the electron beam. Unfortunately, this method also creates electron patch charges on the endcap electrodes which changes the electrostatic behavior. This is one of the limiting factors for the mass measurements presently.

For avoiding these patch potentials and also to reduce the amount of tritium that will be introduced to the experiment, THe-Trap has an external Penning-ion source installed (see Section 3.2). Ions created here are sent down to the ion capture segment. Properly

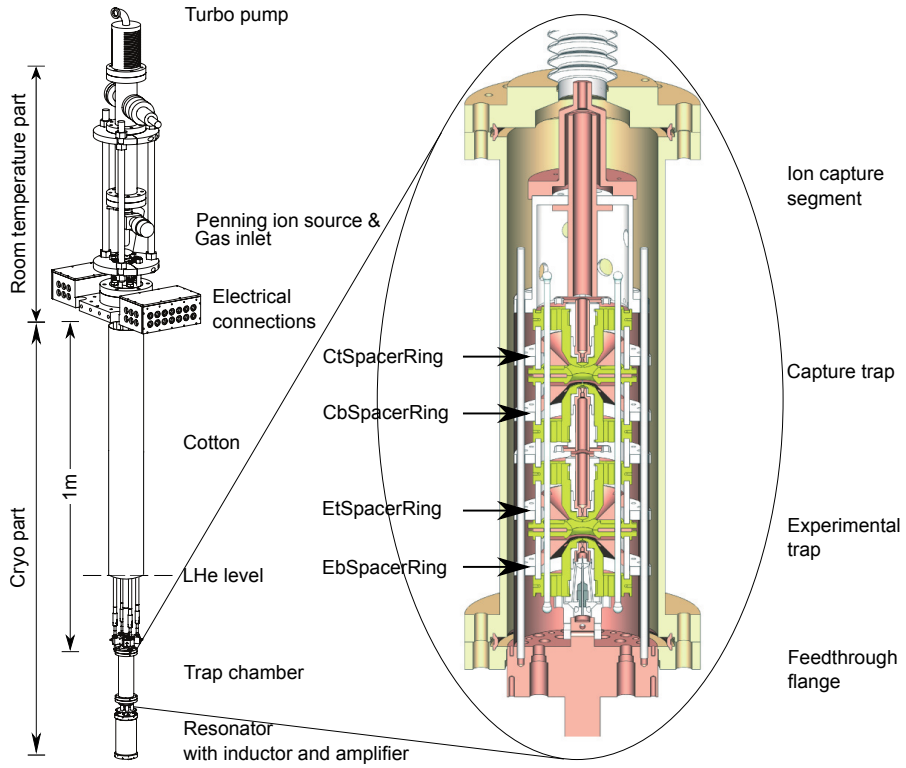

Figure 3.1: Experimental setup of THe-Trap. On top, a turbo molecular pump is mounted. Beneath it is the Penning-ion source, followed by the header containing the electrical connections for the wires going down to the cryogenic electronics. The rest of the experiment is inside a of 5.26 T [Str14] magnet with a cold bore. At the bottom is the trap chamber which is displayed enlarged at the right-hand side. Finally, at the very bottom the cryogenic electronics with the amplifier and the resonator with the inductor coil are located. Macor spacer ring elements are marked. The color coding for the enlarged trap chamber is that all white colored parts are made of Macor, light salmon colored are made of oxygen-free high thermal conductivity copper (OFHC) and green yellow colored components are made of phosphor bronze. This means that the trap electrodes are made of phosphor bronze, the skimmer and the feedthrough flange of OFHC and the supporting structure, for instance the spacer rings of Macor. The holes in the spacer ring guide the wires for the electrical connections of the electrodes. The explanation of the naming is given in Figure 3.2.

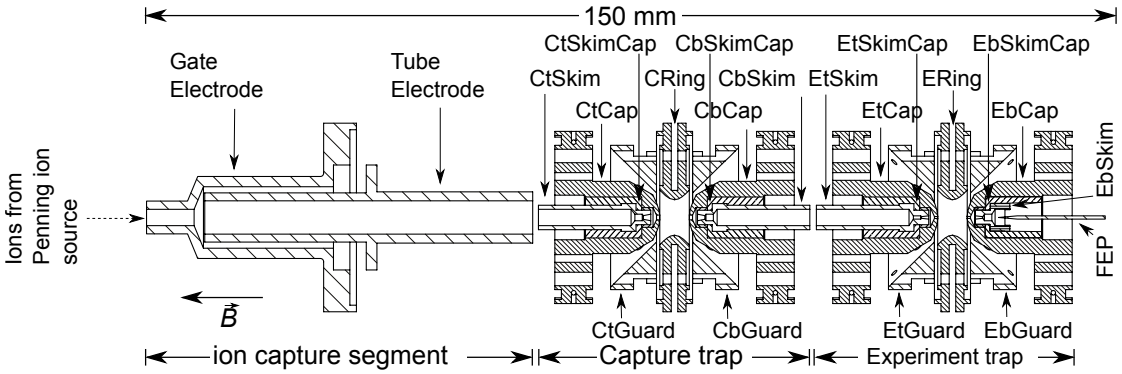

Figure 3.2: Schematic drawing of the content of the trap chamber, introduced in Figure 3.1. The abbreviations C and E stand for Capture trap and Experiment trap, respectively, and t and b for top and bottom. The field emission point is abbreviated by FEP. Figure from [Str14].

switching of the voltages at the ion capture segment and the following skimmer electrodes will hopefully lead in the future to an ion transfer to the capture trap.

Due to the cooldown of the lower part of the experimental setup, the dimensions of the trap electrodes change. A length ℓ at room temperature is transformed in the following way

$$\ell' = (1 - \alpha_{\text{material}}) \cdot \ell \quad , \tag{3.1}$$

where ℓ' is the new length at 4 K and α_{material} the thermal shrinking coefficient of the material for the transition from room temperature to 4 K. Unfortunately, there is not much data available regarding the thermal properties of the materials used (Macor [Cor13], copper and phosphor bronze). Some thermal shrinking coefficients are found in Reference [VDJ91] and validated by the References [RAJ54, CWr64, Cla68, Whi73, Eki06, Spr13, Cor13]. In the end, the following thermal expansion coefficients are used: $\alpha_{\text{macor}} = 0.0018$ and $\alpha_{\text{copper}} = \alpha_{\text{phosphor bronze}} = 0.00326$ because these are the values given by the manufacturer of the Penning-traps. During the investigation the values could be confirmed but mostly an uncertainty is not given. The spread of α_{copper} is 0.0031 – 0.0050 (see References [Whi73] and [RAJ54], respectively) and for α_{Macor}

Table 3.1: Overview of characteristic trap parameters. The different materials and their thermal expansion coefficients are taken into account for the thermal shrinking. The parameters r_E and r_C denote the radius of the hole in the endcap electrodes in the experiment and capture trap, respectively. The estimate of the uncertainties is taken from Reference [Pin07]. Here the upper limit of the uncertainty is shown.

Room temperature		Cryogenic Temperature	
Trap parameter	length	Trap Parameter	length
ρ_0	2.78(1) mm	ρ_0'	2.77(1) mm
z_0	2.28(1) mm	z_0'	2.27(1) mm
d	2.13(3) mm	d'	2.13(3) mm
r_E	201(5) µm	r_E'	200(5) µm
r_C	250(5) µm	r_C'	249(5) µm
		z_{0b}'	2.29(1) mm

0.0018 – 0.0024 (see References [VDJ91] and [Cor13], respectively). Characteristic trap parameters at room temperature and 4 K are given in Table 3.1. Values at room temperature are found in Reference [VDJ90] and at 4 K in [Pin07]. They agree with each other, when the thermal shrinking coefficient is used except for ρ_0. It should be noted that ρ_0 in Reference [VDJ90] is found to be 2.74 mm. In newer CAD drawings $\rho_0 = 2.78$ mm is found. Because $\rho_0' = 2.77$ mm is used in all publications of this group, $\rho_0 = 2.78$ mm and $\rho_0' = 2.77$ mm are used for the simulation. Unfortunately, it cannot be stated yet which value is correct and the values deviate significantly. z_0' describes the hyperbolic shape of the endcap electrode at 4 K. Since Macor has a different thermal shrinking coefficient than copper, z_0' does not describe the distance of the endcap electrode to the center of the trap. For this z_{0b}' is introduced. Based on Equation (3.1), z_{0b}' can be calculated as follows

$$z_{0b}' = \left(1 - \alpha_{\text{Copper}}\right) \left[\underbrace{\left(2.29 - 0.51\right)}_{\text{ring}} - \underbrace{\left(1.08 + 3.61 + 6.73\right)}_{\text{endcap}} \right] + \left(1 - \alpha_{\text{Macor}}\right) \cdot \underbrace{11.92}_{\text{Macor holder}} , \tag{3.2}$$

where all lengths are in millimeter and the values are taken from Figure 3.3.
The effect of the thermal shrinking on the electrode geometry is displayed in Figure 3.3.

Table 3.2: Magnetic susceptibilities for the materials used in the experiment at 4 K. A general uncertainty of 20 % is assumed. It should be noted that nickel's magnetization saturates at 0.645 T [Stu12].

Material	Susceptibility
Macor	$2 \cdot 10^{-5}$ [LFLM90]
Nickel	$6 \cdot 10^{+2}$ [Com14a]
OFHC	$-9 \cdot 10^{-6}$ [Eki06]
Phosphor Bronze	$-6 \cdot 10^{-6}$ [Eki06]
Titanium	$2 \cdot 10^{-4}$ [Eki06]
Tungsten	$7 \cdot 10^{-5}$ [Eki06]

It should be noted that the ring electrode is shrinking and comes closer to the trap center, while the ring electrode is shifting upwards. This leads to the fact that the surface of the endcap electrode is not an equipotential surface of a quadrupole potential anymore. A countersink is indicated in the endcap electrode hole. This widens the hole for the experiment trap from a radius of 152.5(5) µm to 200.2(5) µm. The countersink is 255 µm deep. The purpose of the countersink is that if the electron beam from the FEP widens up, it does not hit the inner surface of the endcap electrodes. This would lead to patch charges and further electrostatic field distortions. Since the FEP is only located at the experiment trap, a countersink for the capture trap is installed. Further, magnetic susceptibilities of the important parts of the experimental setup are given in Table 3.2. An estimation of the uncertainty is difficult, but again the values should be within 20 % of the provided values.

3.2 Penning-ion source

THe-Trap is equipped with an external Penning-ion source which was first described in [Pin07] and was further investigated by [Hö10] and [Tre11]. The Penning-ion source allows the ion production of any gaseous element outside of the Penning-trap electrodes. For the final goal of this experiment, the measurement of the Q-value of tritium, the external ion source has the advantage that the trap region will be less exposed to tritium gas. This is crucial because tritium is radioactive, and a contamination of the trap

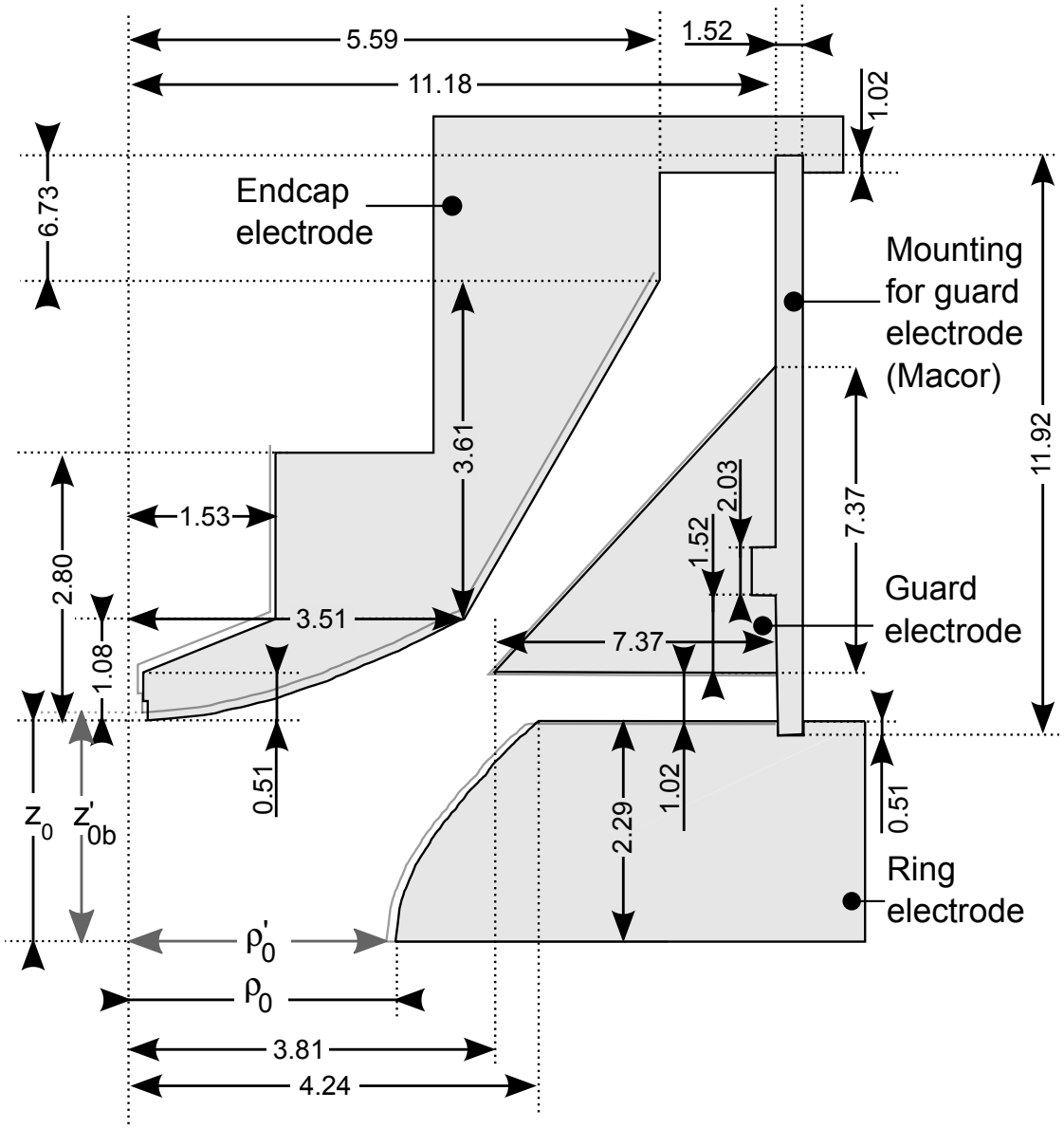

Figure 3.3: Schematic drawing (not to scale) of a cut through the upper right part of the Penning-trap electrodes, including the Macor mounting for the guard electrodes. The shape of the electrodes after cooling down to 4 K is indicated with gray lines. The corresponding arrows are also gray. This shown effect is not to scale. All given dimensions are in millimeters and based on Reference [VDJ90]. Values for z_0, z'_{0b}, ρ_0 and ρ'_0 are given in Table 3.1.

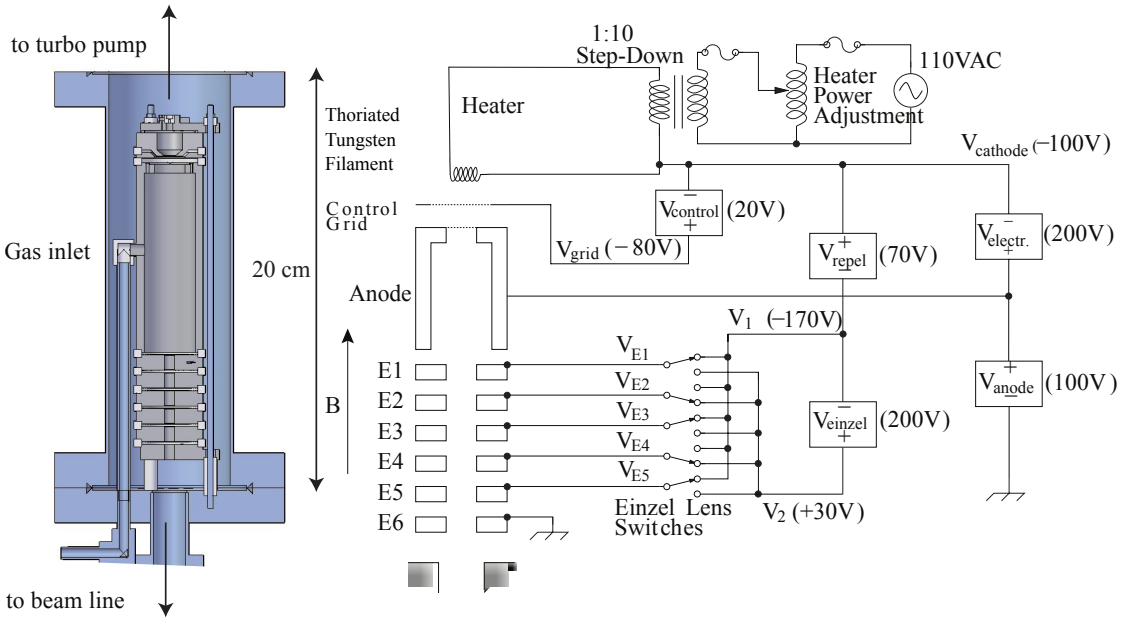

Figure 3.4: On the left-hand side a model of the Penning-ion source is shown. To generate specific ions the corresponding gas can be fed through the gas inlet. The ions are sent down towards the ion capture section. The volume is pumped by the turbo pump located on top. On the right-hand side the circuit diagram of the Penning-ion source including a usable set of voltages is given. This picture is taken from [DBH+11].

.

electrodes with tritium has to be prevented under any circumstance. If tritium gas contaminates the trap, tritium itself will prevent precise measurements, because of rest gas interactions with the charged tritium. Like hydrogen, tritium gets absorbed by the trap electrodes and thus it is hard to remove again. But also the emitted β decay electrons will ionize other rest gas particles, thereby loading the trap with additional ions and the resulting ion-ion interaction will prevent a precise mass measurement as well. With a half life of 12.3 years, the contamination would not reduce significantly in the expected life time of the experiment. Another advantage is that by creating the ions outside of the Penning-trap electrodes, less or no patch charges are created on the electrodes.

The schematics and electrical circuit of the ion source can be found in Figure 3.4. Ions are produced as follows. First, gas is inserted through the gas inlet. Applying proper voltages (shown in parenthesis in Figure 3.4) and a heating current for the thoriated

tungsten filament creates an electron beam towards the anode. A thoriated tungsten filament is chosen because a bare tungsten filament would require a too large heating current which would be out of the specification of the feedthroughs used. Before, a barium dispenser cathode was used that got poisoned quickly and could not generate enough electrons if it was used at a pressure higher than 10^{-6} mbar. The emitted electrons are accelerated downwards and forced on a spiral orbit by an external magnetic field. While electrons hit the gas molecules, the inserted gas is ionized. The external magnetic field is produced by a solenoid which has a strength of 10 mT at the center of the ion source with 1 A of current [Pin07]. The solenoid is wound around the vacuum envelope of the ion source, indicated in blue at the left-hand side of Figure 3.4. In Reference [Pin07] it is shown that the magnetic field of the superconducting magnet drops to roughly 4 mT at the location of the Penning-ion source and hence cannot influence the magnetic field by the Penning-ion source solenoid significantly. To investigate the properties of the thoriated tungsten filament and to optimize the production of the ion beam a Faraday cup was designed and installed right below the ion source.

3.3 Custom made Faraday cup

This section is about the design of a custom made Faraday cup. The purpose of this cup is to analyze and optimize the Penning-ion source, as well as to reduce the risk of contaminating the traps with tritium. The Faraday cup is placed directly under the ion source. A sketch is shown in Figure 3.5. The Faraday cup can be moved in and out of the beam line. The design is chosen such that, when the Faraday Cup is moved in the beam line completely, the diameter of the beam line is reduced from the full tube diameter of 16 mm to 2.1 mm. This is one of the precautions taken to minimize the risk of contaminating the traps with tritium. Further gas barriers at the mounting arm prevent that the gas can take other paths to the traps.

For analyzing the Penning-ion source, the Faraday cup consists of a collimator plate and a cup plate (detailed technical drawing is given in Figure 3.6). The collimator plate

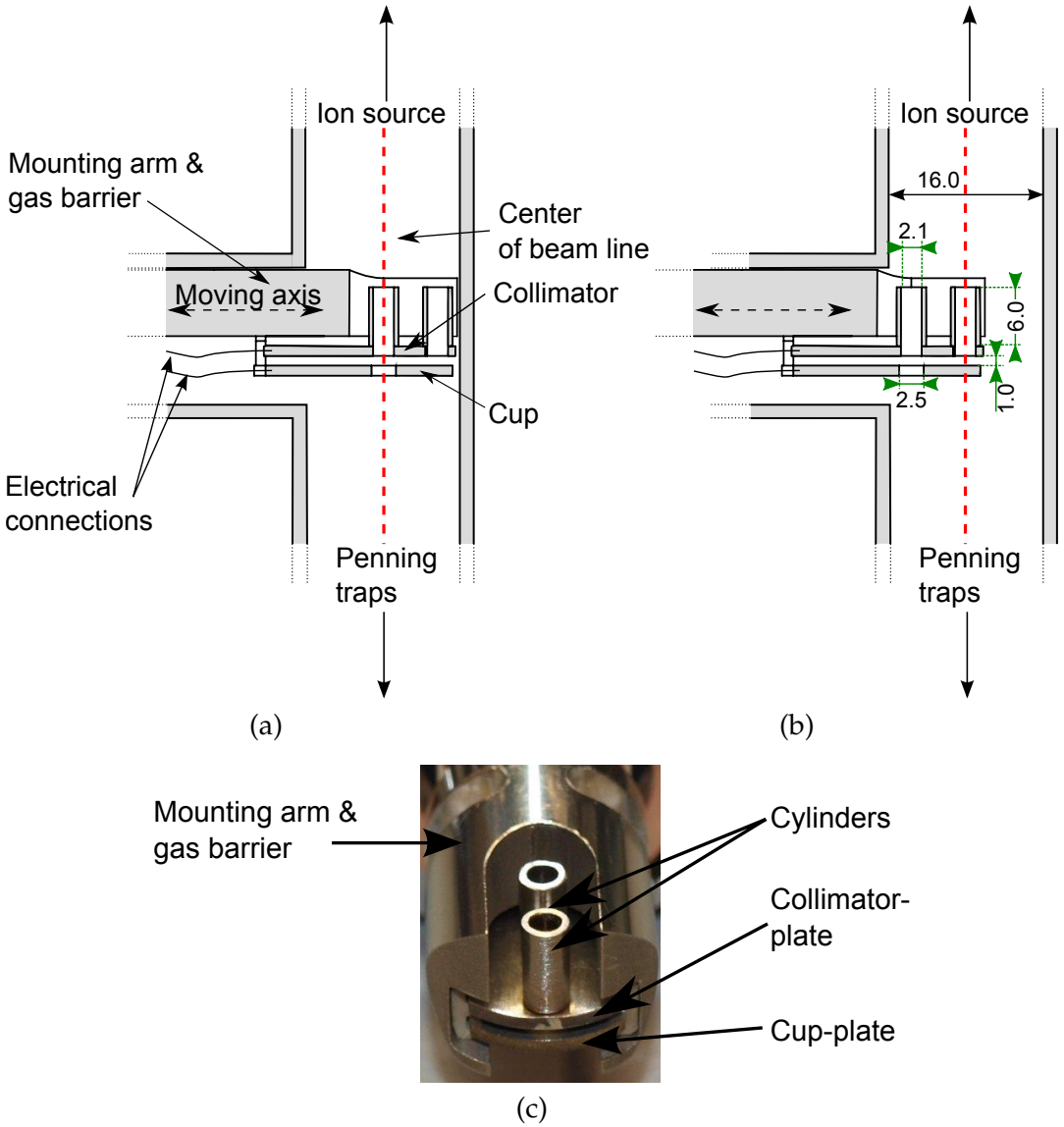

Figure 3.5: The custom-designed Faraday cup consists of two plates which have an electrical connection to the outside of the vacuum. The collimator-plate has two holes (see also Figure 3.6), each with a cylinder on top to reduce the gas flow further. The cup-plate has one hole which is located under the left hole of the collimator-plate. In (a), the Faraday cup is moved in completely and additionally working as a gas barrier. For the investigation of the ion beam, produced by the Penning-ion source, the Faraday cup is moved out by 5.5 mm, seen in (b). Then, the collimator's second hole is placed in the middle of the beam line and the current that flows in the middle of the beam tube is detected at the cup-plate. The Faraday cup can be moved in continuous steps, too. It is pulled out of the beamline completely, called fully-out, for pumping. All dimensions are in mm. In (c) a picture of the Faraday cup including the two plates with the cylinders on top from the front is shown.

is located closer to the Penning-ion source than the cup plate and has two holes, each with a diameter of 2.5 mm. On top of each hole a cylinder with a height of 6 mm and an inner diameter of 2.1 mm is welded. The cup plate is located 1 mm under the collimator plate and has one hole with a diameter of 2.5 mm that is placed under the hole closer to the mounting arm. Both plates are electrically insulated from each other and each has an electrical connection via feedthroughs to the outside of the vacuum. It is useful to measure the current at both plates, because the ratio in the current measurement can be compared with the geometrical ratio of the surface area of the plates that can be seen in a top view. From this further conclusions on the width of the beam can be drawn. The cup is designed to be operated in one of three positions.

1. "Fully-in" as shown in Figure 3.5 (a): This position is used to load the trap. The beam of the ions from the source has a direct access through the cup. The diameter of the beam line is reduced to 2.1 mm and ions flying in the center of the beam line can reach the Penning-traps.

2. "Diagnostics" as shown in Figure 3.5 (b): The cup is moved out by 5.5 mm from the fully-in position and the right hole of the collimator plate is located in the center of the beam line. All ions that would have passed in the fully-in position will be detected by measuring the current at the cup plate. In this position, the Penning-ion source is optimized.

3. "Fully-out": The cup is pulled completely out from the beamline. This position is used when the setup is being pumped.

When the Faraday cup is moved along its axis, the spatial distribution of the ion beam can be measured along that axis.

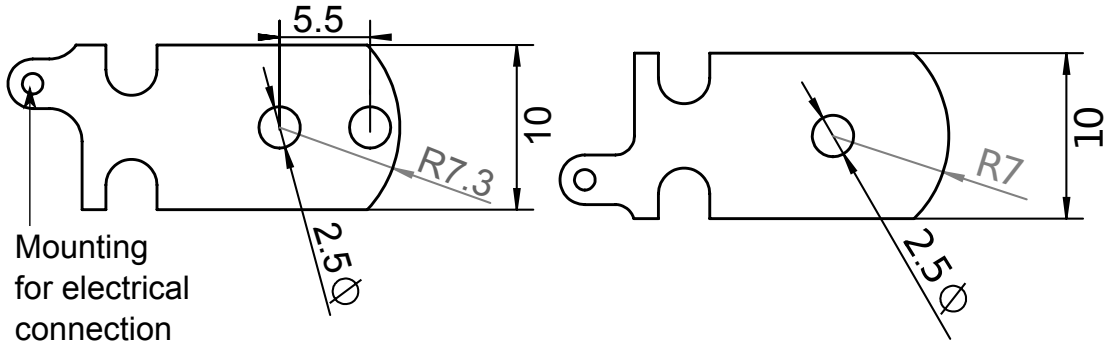

Figure 3.6: On the left side the collimator and on the right side the cup plate is shown. The right hole in the collimator and the hole in the cup are located in the center of the vacuum tube if the Faraday cup is moved in completely. The plates are made of stainless steel and 1 mm thick. The two notches at each plate are for fixing the plates in the mounting arm. All dimensions are given in mm.

Chapter 4

Simulations of the electrostatic properties of the THe-Trap Penning-trap

In the previous chapters, the reasons of the deviations from an ideal Penning-trap are discussed, their deviations approximated by higher-order Legendre polynomials and quantified by the corresponding coefficients. The Legendre polynomials are chosen because they are the solutions for the occurring Laplace equation [Jac62]. This chapter presents the results of extended simulations to determine the values of the higher-order coefficients. For a better understanding, the influences of each electrode on the electrostatic potential is investigated separately. In Section 4.1 the final results of the simulation and the resulting fit-coefficients are given. For this, all known systematic shifts are taken into account and moreover, the reliability of chosen simulation parameters like the mesh size is verified. This section is followed by the explanation of the determination of the statistical and systematic uncertainties (see Sections 4.1.2 and 4.1.3, respectively), as well as the uncertainty induced by inaccuracies of the simulated model (see Sections 4.1.4 – 4.1.6). The results obtained with Comsol Multiphysics are compared with those obtained with Vector Fields Opera in Reference [Sch11] (see Section 4.2). In

addition to the determination of the influence of the deviations, the image charge effect is simulated, and from this the related frequency shift is calculated (see Section 4.3). In Section 4.4, the conclusions from the simulation for the experiment are given.
For the numerical simulations Comsol Multiphysics 4.2 up to version 4.4 including the "AC/DC Module" and the "CAD Import Module" is used. The software is run on a server having the following system properties:

- Operating system: Scientific Linux 6.2
- RAM: 256 GB
- Intel® Xeon® CPU E5-2670 0 @ 2.60 GHz .

4.1 Final coefficients

In this section the final results of the simulations on the electrostatic properties of the THe-Trap electrodes are presented, using the best approximation of the geometry that could be made (see Section 4.1.1). The simulations are carried out to investigate how the deviations in the shape of the electrodes from the ideal case influence the electrostatic potential. It is the first time that the electrostatic properties of THe-Trap are investigated so thoroughly. Most of the coefficients have never been determined before. Hence, the result itself is most important. Additionally, great efforts are taken to estimate the uncertainty of the simulation result. These uncertainties are just investigated to give an estimate of the reliability of the fit-coefficients. This has never been done before for THe-Trap. The definitions of fit-coefficient are given in Table 4.1. For testing the reliability of the fit-coefficients, various tests and consistency checks are performed with the simulation. To investigate the software's numerical stability, a resolution study is performed (Section 4.1.2). In this study, the dependency of the fit-coefficient on the resolution chosen is investigated. The deviations between different resolutions are taken as statistical uncertainty.
To check if the results obey the linearity of Maxwell's equations, the potential generated

Table 4.1: Definitions of the fit-coefficients for fitting the electrostatic potential created by the corresponding electrode with Equation (2.13). The index n is a non negative integer indicating the order of the Legendre polynomial. If n is even, for example both endcap electrodes are set to 1 V. For n odd, only the upper endcap electrode is set to 1 V.

Coefficients mm^{-n}	Electrode(s)
S_n	Skimmer(s)
E_n	Endcap(s)
D_n	Guard(s)
R_n	Ring

by setting the endcap electrodes to 1 V individually and added up later should be the same as when both endcap electrodes are set to 1 V (see Section 4.1.3). These deviations are taken as systematic uncertainty.

Also, great effort is taken to figure out the influence of geometrical uncertainties on the fit-coefficients. The guard electrodes are moved along the z-axis and fillets are added to the otherwise sharp inner edges of the guard electrodes (Section 4.1.4).

The electrostatic potential of each electrode is simulated with and without taking the thermal shrinking into account. The radius of the hole in the endcap is varied and the influence of the countersink is evaluated. The final uncertainty caused by inaccuracies of the simulated model is chosen to be 50 % of the shift due to the added fillets to the guard electrode edges, similarly 50 % of the shift due to uncertainty of thermal shrinking, the guard position having an uncertainty of 50 µm and the hole radius in the endcap electrodes of 5 µm. These individual uncertainties are summed up by Gaussian error propagation and lead to the final model uncertainty, given in the fourth column of Table 4.2 and 4.3. The final uncertainty given in parenthesis additionally includes the statistical and systematic uncertainty, but compared to the model uncertainty the statistical and systematic uncertainties are negligible. It turns out that for all fit-coefficients, the uncertainty due to the model uncertainties is two or more orders of magnitude bigger than the uncertainty due to statistical or systematic influences. This success of the simulation is based on the use of a two-dimensional model with cylindrical symmetry instead of a three-dimensional one (see Section 4.2). It is possible to reduce the numer-

ical influence so far that the uncertainties are dominated by the simulated model and not by the numerical precision of the simulation.

Choosing 50 % of the fillet shift as uncertainty is a conservative choice, allowing bending radius between 2.5 – 7.5 µm. If it were larger, it would be visible in the technical drawings [VDJ90], and smaller would require more precise manufacturing than it was available. Also the uncertainty of the thermal shrinking coefficient is unknown. But the found spread of the thermal shrinking coefficients of up to 50 % leads to the conclusion that the shift of the coefficients due to thermal shrinking should have the same uncertainty. All these model uncertainties should just give an estimate of the influence of the different simulation parameters. The number of adjustable parameters are so high that only a few can be tested to see their influence on the result. Testing more parameters would not improve the result because the simulation model would not necessarily become a better description of the real experiment. For this the exact parameters of the experiment must be known.

In general, the relative model uncertainties are generally 5 % or slightly larger. At first glance, this seems to be disappointing, but this is not the fault of the simulation but the massive influence of the model uncertainties. In the next sections the shifts due to the model changes are given and can be adapted, if necessary. Therefore also coefficients, such as D_5 or R_6 are given which do not significantly deviate from zero, but maybe the choice of the model uncertainties is too conservative and in the future it turns out that the fit-coefficients are significant. In the simulation itself the fit-coefficients can be obtained clearly and deviate significantly from zero in the fit. The relative change of every coefficient by every model uncertainty like the guard electrode position or thermal shrinking is given. Also the weighting factor for the final uncertainty is presented and if it turns out in the future that the uncertainty is estimated too conservatively, then it is possible to calculate the new final uncertainty with new weighting factors based on the values given here.

As expected, the skimmer S_n-coefficients are many orders of magnitude smaller than the coefficients of the other electrodes, because the skimmer electrodes are well

Table 4.2: Final fit-coefficients of the electrostatic simulations of the capture trap, with a hole radius of 250 µm in the endcap electrodes. The full precision with the statistical and systematic uncertainties is given in Appendix A. There, also coefficients of seventh and eighths order are given which are not significant if model uncertainties are taken into account. More information in the text.

	Value	Absolute uncertainties		
		Stat	Sys	Model
	/ mm^{-n}	/ mm^{-n}	/ mm^{-n}	/ mm^{-n}
S_1	$2.47(89) \cdot 10^{-06}$	$1.00 \cdot 10^{-14}$	$1.54 \cdot 10^{-10}$	$8.87 \cdot 10^{-07}$
S_2	$3.0(10) \cdot 10^{-06}$	$1.60 \cdot 10^{-12}$	$1.26 \cdot 10^{-08}$	$1.08 \cdot 10^{-06}$
S_3	$8.4(30) \cdot 10^{-07}$	$8.60 \cdot 10^{-14}$	$5.36 \cdot 10^{-11}$	$2.99 \cdot 10^{-07}$
S_4	$8.7(31) \cdot 10^{-07}$	$9.00 \cdot 10^{-12}$	$3.54 \cdot 10^{-09}$	$3.08 \cdot 10^{-07}$
E_1	$1.65944(67) \cdot 10^{-01}$	$1.70 \cdot 10^{-11}$	$4.66 \cdot 10^{-08}$	$6.62 \cdot 10^{-05}$
E_2	$1.0987(60) \cdot 10^{-01}$	$1.00 \cdot 10^{-10}$	$1.14 \cdot 10^{-06}$	$5.96 \cdot 10^{-04}$
E_3	$1.038(80) \cdot 10^{-02}$	$1.50 \cdot 10^{-10}$	$1.67 \cdot 10^{-08}$	$8.02 \cdot 10^{-05}$
E_4	$2.07(17) \cdot 10^{-04}$	$5.70 \cdot 10^{-10}$	$3.15 \cdot 10^{-07}$	$1.68 \cdot 10^{-05}$
E_5	$-1.809(73) \cdot 10^{-04}$	$6.80 \cdot 10^{-10}$	$4.26 \cdot 10^{-09}$	$7.29 \cdot 10^{-06}$
E_6	$-2.341(80) \cdot 10^{-05}$	$2.70 \cdot 10^{-09}$	$7.87 \cdot 10^{-08}$	$7.82 \cdot 10^{-07}$
D_1	$3.18(33) \cdot 10^{-03}$	$1.20 \cdot 10^{-12}$	$4.18 \cdot 10^{-08}$	$3.30 \cdot 10^{-04}$
D_2	$-2.46(52) \cdot 10^{-04}$	$6.10 \cdot 10^{-10}$	$1.12 \cdot 10^{-08}$	$5.20 \cdot 10^{-05}$
D_3	$-6.02(35) \cdot 10^{-04}$	$1.00 \cdot 10^{-11}$	$8.57 \cdot 10^{-09}$	$3.32 \cdot 10^{-05}$
D_4	$-5.33(36) \cdot 10^{-04}$	$3.40 \cdot 10^{-09}$	$6.30 \cdot 10^{-09}$	$3.61 \cdot 10^{-05}$
D_5	$-3.21(138) \cdot 10^{-05}$	$4.70 \cdot 10^{-11}$	$5.63 \cdot 10^{-10}$	$1.38 \cdot 10^{-05}$
D_6	$2.59(19) \cdot 10^{-05}$	$1.60 \cdot 10^{-08}$	$1.40 \cdot 10^{-08}$	$1.87 \cdot 10^{-06}$
R_2	$-1.0963(63) \cdot 10^{-01}$	$3.70 \cdot 10^{-10}$	$7.41 \cdot 10^{-07}$	$6.32 \cdot 10^{-04}$
R_4	$3.26(27) \cdot 10^{-04}$	$2.10 \cdot 10^{-09}$	$2.11 \cdot 10^{-07}$	$2.64 \cdot 10^{-05}$
R_6	$-2.68(148) \cdot 10^{-06}$	$9.80 \cdot 10^{-09}$	$4.37 \cdot 10^{-08}$	$1.48 \cdot 10^{-06}$

Table 4.3: Final fit-coefficients of the electrostatic simulations of the experiment trap electrodes, with a hole radius of 200 µm including countersink in the endcap electrodes. The full precision with the statistical and systematic uncertainties is given in Appendix A. There, also coefficients of seventh and eights order are given which are not significant if model uncertainties are taken into account. More information in the text.

	Value	Absolute uncertainties		
		Stat	Sys	Model
	/ mm^{-n}	/ mm^{-n}	/ mm^{-n}	/ mm^{-n}
S_1	$4.1(15) \cdot 10^{-07}$	$1.90 \cdot 10^{-15}$	$1.15 \cdot 10^{-10}$	$1.48 \cdot 10^{-07}$
S_2	$5.1(18) \cdot 10^{-07}$	$4.20 \cdot 10^{-13}$	$6.30 \cdot 10^{-10}$	$1.81 \cdot 10^{-07}$
S_3	$1.41(50) \cdot 10^{-07}$	$1.70 \cdot 10^{-14}$	$3.92 \cdot 10^{-11}$	$5.02 \cdot 10^{-08}$
S_4	$1.48(52) \cdot 10^{-07}$	$2.30 \cdot 10^{-12}$	$1.80 \cdot 10^{-10}$	$5.22 \cdot 10^{-08}$
E_1	$1.66032(67) \cdot 10^{-01}$	$2.60 \cdot 10^{-11}$	$3.02 \cdot 10^{-08}$	$6.57 \cdot 10^{-05}$
E_2	$1.0996(60) \cdot 10^{-01}$	$7.40 \cdot 10^{-11}$	$2.55 \cdot 10^{-07}$	$5.97 \cdot 10^{-04}$
E_3	$1.041(80) \cdot 10^{-02}$	$2.30 \cdot 10^{-10}$	$1.09 \cdot 10^{-08}$	$8.04 \cdot 10^{-05}$
E_4	$2.31(19) \cdot 10^{-04}$	$4.10 \cdot 10^{-10}$	$7.20 \cdot 10^{-08}$	$1.86 \cdot 10^{-05}$
E_5	$-1.732(70) \cdot 10^{-04}$	$1.00 \cdot 10^{-09}$	$2.80 \cdot 10^{-09}$	$6.95 \cdot 10^{-06}$
E_6	$-1.733(52) \cdot 10^{-05}$	$1.90 \cdot 10^{-09}$	$1.87 \cdot 10^{-08}$	$5.07 \cdot 10^{-07}$
D_1	$3.18(33) \cdot 10^{-03}$	$1.80 \cdot 10^{-12}$	$4.11 \cdot 10^{-08}$	$3.30 \cdot 10^{-04}$
D_2	$-2.48(53) \cdot 10^{-04}$	$6.80 \cdot 10^{-10}$	$6.52 \cdot 10^{-09}$	$5.24 \cdot 10^{-05}$
D_3	$-6.02(35) \cdot 10^{-04}$	$1.60 \cdot 10^{-11}$	$8.22 \cdot 10^{-09}$	$3.32 \cdot 10^{-05}$
D_4	$-5.34(36) \cdot 10^{-04}$	$3.80 \cdot 10^{-09}$	$1.30 \cdot 10^{-09}$	$3.61 \cdot 10^{-05}$
D_5	$-3.2(14) \cdot 10^{-05}$	$7.20 \cdot 10^{-11}$	$4.74 \cdot 10^{-10}$	$1.38 \cdot 10^{-05}$
D_6	$2.58(19) \cdot 10^{-05}$	$1.80 \cdot 10^{-08}$	$2.40 \cdot 10^{-08}$	$1.86 \cdot 10^{-06}$
R_2	$-1.0971(63) \cdot 10^{-01}$	$3.00 \cdot 10^{-10}$	$1.16 \cdot 10^{-06}$	$6.32 \cdot 10^{-04}$
R_4	$3.02(26) \cdot 10^{-04}$	$1.70 \cdot 10^{-09}$	$3.37 \cdot 10^{-07}$	$2.62 \cdot 10^{-05}$
R_6	$-8.5(17) \cdot 10^{-06}$	$8.00 \cdot 10^{-09}$	$8.45 \cdot 10^{-08}$	$1.65 \cdot 10^{-06}$

screened by the adjacent endcap electrode. This also explains why some of the S_n-coefficients in Table 4.3 are almost compatible with zero. The influence of the different hole radii in the endcap electrodes is visible, as seen in Tables 4.2 and 4.3. The influence of the hole radius in the other coefficients is not visible within the final uncertainty. Statistically these influences are clearly visible in the simulation, as it is shown later. The guard electrodes are designed to cancel out the R_4 coefficient and to have only a small D_2 coefficient compared to R_2. Unfortunately, D_2 has an uncertainty of 21 % due to model uncertainties, which leads to a similar uncertainty when the conclusions for the experiment are drawn in Section 4.4. The other important fit-coefficients R_2, R_4 and D_4 that are used in the daily work at the experiment have an uncertainty of roughly 10 % or less. Hence, simulating the electrostatic properties of the THe-Trap electrodes is successful.

4.1.1 Simulated model

For simulating the electrostatic properties of the THe-Trap electrodes, the electrodes must be modeled in the simulation as accurately as possible. This section describes the properties of the model used. For the modeling, the dimensions of the electrodes must be known. Unfortunately, the only way to get this information is a section view of the CAD model and References [VDJ90, VDJ91]. It is very difficult to measure the dimensions of the geometry, when the electrodes are assembled and impossible when they are cooled down to 4 K. Possible errors in the relative position of the electrodes or the absolute size will occur in the two-dimensional model again. Therefore, the dependency of the fit-coefficients on the model parameters is tested and from this possible uncertainties in the fit-coefficients are assumed. A sketch of the two-dimensional model in Comsol Multiphysics is given in Figure 4.1. In the simulation the cylindrical symmetry of the electrode geometry is used. For this the slits in the guard electrodes are ignored. Using the rotational symmetry reduces the dimensions of the simulation from three to two and saves hours or even days of computation time. It is not shown that the entire simulated model is surrounded by a box which is 8.2 mm wide and 20 mm high.

The rim of this box is defined to be at ground potential and gives the global boundary condition of the simulation. The dimensions of the box are chosen so that the defined ground potential does not change the potential in the center of the trap.
To ensure that the surfaces of the electrodes are hyperbolic, the trap electrodes are modeled in Comsol Multiphysics based on the dimensions given in Table 3.1. The software offers tools to form geometries based on mathematical formulas which guarantee the exact shape.
After the simulation, the nodes of the mesh including their coordinates (ρ,z) along with the electrostatic potential values are exported and fitted by Equation (2.13). All points that are used for fitting are inside a rectangle with a height of 1 mm and a width of 0.5 mm (see Figure 4.1). This choice is reasonable, because the motional amplitudes of the ion are usually a few 10 µm [Str14] or less when they are cooled. The final fit-coefficients (see Table 4.2 and Table 4.3) are obtained by fitting the electrostatic potential with a sum of Legendre polynomials up to the tenth order, as defined in Equation (2.12). Here in the two-dimensional case the coordinates are $r^2 = \rho^2 + z^2$ and $\cos(\theta) = z/\sqrt{\rho^2 + z^2}$.

4.1.2 Resolution study

The resolution study is for proving that the simulations will converge to the same value regardless of the mesh chosen. For this, the resolution in the whole simulation is increased stepwise, which means that the mesh size becomes smaller and thus more points will fall within the fit area. The electrostatic field of the skimmers, endcaps, guards and the ring electrode is simulated. To obtain a symmetric setup regarding the mirror symmetry to the $z = 0$ plane (see Figure 4.1), for example both skimmer or both endcaps are set to 1 V and for an asymmetric setup only the upper electrode is set to 1 V. The setup is always treated with cylindrical symmetry. How the ring electrode fit-coefficient R_2 changes as a function of the mesh size is shown in Figure 4.2. All plots are created with gnuplot [Gnu14]. This study of the behaviour at different resolutions is performed for every electrostatic potential produced by the individual electrodes (see

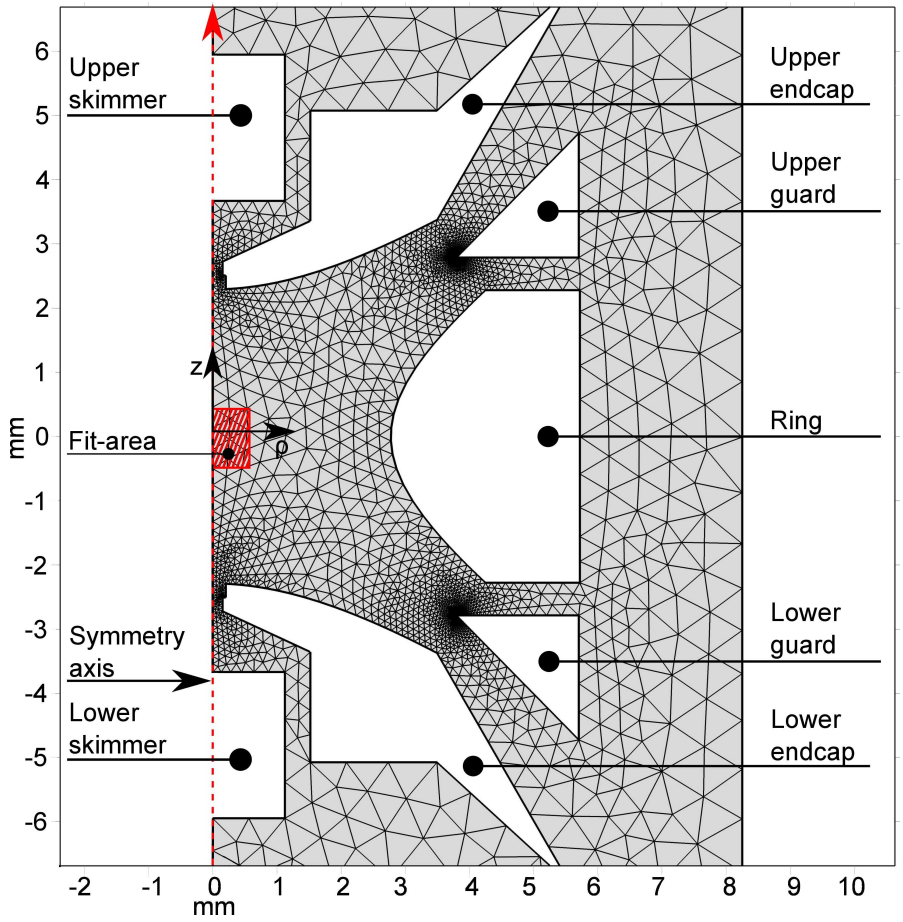

Figure 4.1: Cutview of the THe-Trap Penning-trap electrodes. The full trap is obtained by rotating the view around the z-axis. The skimmer electrodes are simplified, their hole is removed because their influence on the electric potential in the center of the trap is heavily screened by the endcap electrodes. The outer part of the other electrodes is removed because their outer parts do not influence the electrostatic potential in the center of the trap significantly. For clarity, only a coarse mesh is shown. The actual mesh used in the simulations is up to 10^2 times finer, and 10^4 times more points in the fit-area. The electrodes are assumed to be field-free and hence are not meshed.

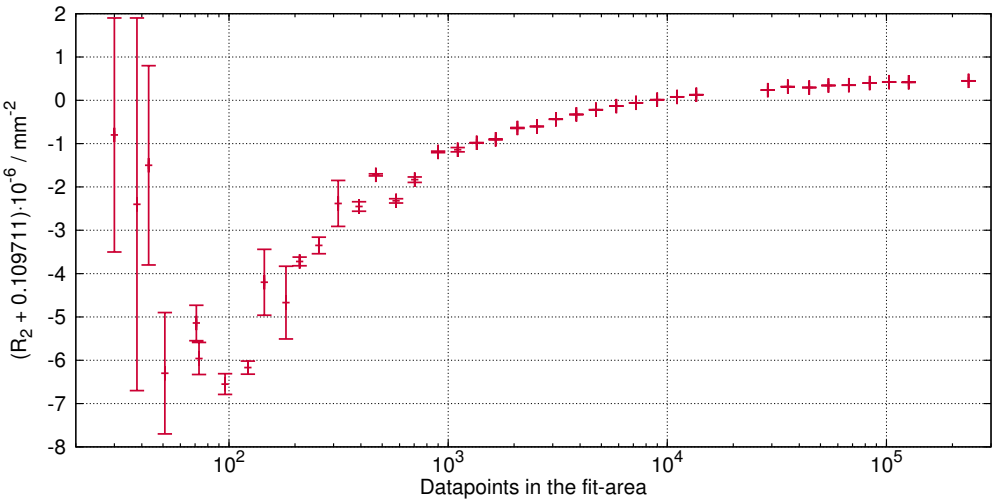

Figure 4.2: R_2 fit-coefficient (see Table 4.1) extracted for different resolutions, when a tenth order Legendre polynomial fit (see Equation (2.13)) is applied. The higher the number of datapoints in the fit-area is, the higher the resolution gets. The simulation is done with the geometry shown in Figure 4.1. The uncertainty of the fit is calculated as explained in Section B.1. Gaps in the plot come from failed meshes attempts. More information in the text.

Table 4.1) so that each neighboring point to the right has an increase of 20 % in the number of datapoints in the fit-area. The gaps in the plot come from failed meshing. The scatter of R_2 from the lowest to the highest resolution value is around $2 \cdot 10^{-5}$. To take into account that the simulation results still scatter or possibly have not fully converged in other cases, five resulting coefficients with the highest resolution are averaged using the uncertainty of the coefficients as weight. The standard deviation of this average is given as statistical uncertainty. Higher orders than tenth Legendre polynomial for fitting were tried, but the next additional higher fit-coefficients are compatible with zero. The clear convergence of the simulation is based on the use of a two-dimensional model. Before, a three-dimensional model was tried and the numerical stability is way worse (see Section 4.2).

The meshing algorithm of Comsol Multiphysics failed four times at high resolutions due to a so called “inverted mesh failure”. Comsol Multiphysics starts to build the mesh at multiple points in the model. When the mesh grows, these meshes from the

different starting points meet each other. Before the meshing starts upper and lower limits of the mesh size are set. Hence, the algorithm cannot reduce the mesh size so far that the mesh cells fit for sure. If the meshes cannot match each other, the simulation tries to rebuild the mesh with a different configuration. If the mesh is too fine, the algorithm needs too many iteration steps to find a proper mesh and thus stops. The self-written analysis software is able to determine these cases reliably and the influence on the final result is negligible. It can be concluded that in the two-dimensional case the fit-coefficients converge and the resulting statistical uncertainty is much smaller than the model uncertainty and hence can be neglected.

4.1.3 Consistency checks

Except for the uncertainty due to different resolutions chosen (see Section 4.1.2) it is also reasonable to check if the result given by Comsol Multiphysics obey the linearity of Maxwell's equations. Hence two consistency checks are made. The first check makes use of the fact that electrostatic potentials can be superimposed. To verify the electrostatic potential, first the upper endcap is set to 1 V, then the lower endcap is set to 1 V, and finally both endcaps are set to 1 V. Superimposing the potential obtained from the first and second simulations, should give the electrostatic potential of the last simulation (see Figure 4.3). Every time the electrostatic potential is fitted by the Legendre polynomials. The deviation of the fit-coefficients from each other in the different cases is taken as systematic uncertainty for the even fit-coefficients. In Figure 4.3 (d) the deviations from the linearity of Maxwell equations is shown. It should be noted that they are at the 10^{-15} V level. The visible structures are not explained yet, but the deviations shown are so small that their influence on the fit-coefficient is completely dominated by the model uncertainties. For estimating the systematic uncertainty of the odd fit-coefficients, the following is assumed. For example, the potential generated by the upper endcap electrode $\Phi_{\text{Upper endcap}}(z, \rho)$ should be equal to $\Phi_{\text{Lower endcap}}(-z)$. Hence, first $\Phi_{\text{Upper Endcap}}(z)$ is simulated and then fitted, followed by $\Phi_{\text{Lower endcap}}(z)$. The resulting coefficients should be $E_{n_{\text{Upper endcap}}} = E_{n_{\text{Lower endcap}}}$ for n

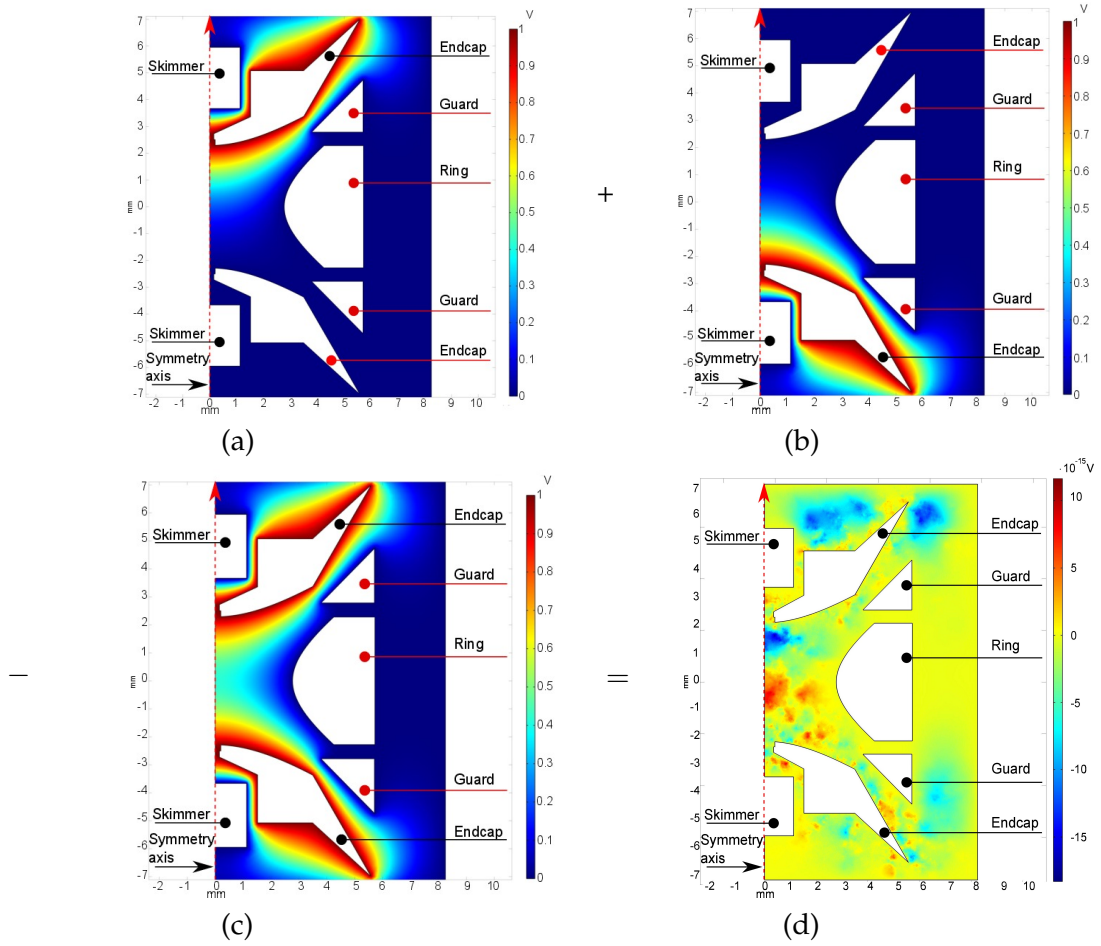

Figure 4.3: Models used as explained in Section 4.1. In the upper left figure (a) the electric potential is displayed with the upper endcap electrode set to 1 V, while in the upper right one (b) 1 V is set to the lower endcap electrode. These should sum up to the electrostatic potential in the lower figure (c), where both endcap electrodes are set to 1 V. The difference of the electrostatic potential in figure (c) from the sum of the electrostatic potentials in figure (a) and (b) is displayed in figure (d) and shows to which precision the result of the simulation obey the linearity of Maxwell's equations.

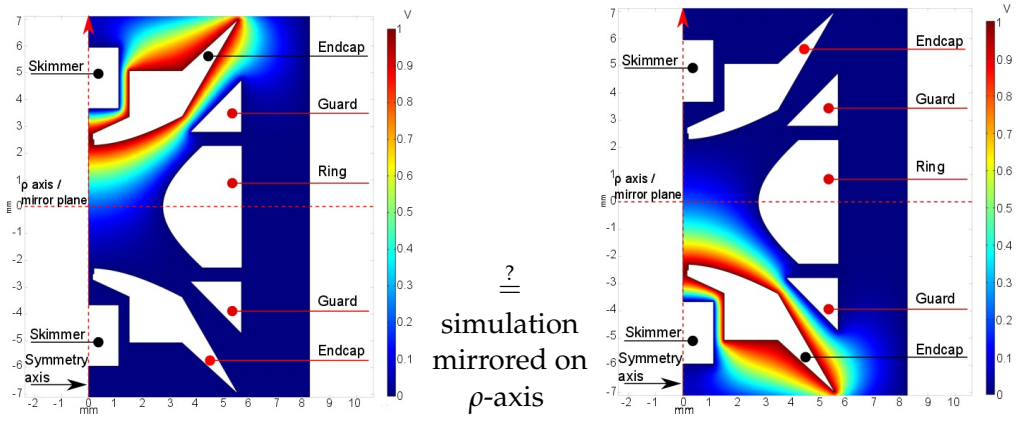

Figure 4.4: Model used as explained in Section 4.1. This test uses the mirror symmetry of the model with respect to the $z = 0$ plane (see Figure 4.1). The electric potential in the left and right figure should have the same absolute value and differ just by a factor of (-1) for odd fit-coefficients. A plot of the differences looks qualitatively the same as in Figure 4.3 and hence is not given again.

even and $E_{n_{\text{Upper endcap}}} = -E_{n_{\text{Lower endcap}}}$ for n odd. This concept is displayed in Figure 4.4. Another consistency check is $E_{n_{\text{Upper endcap}}} = E_{n_{\text{Lower endcap}}} = 1/2 E_{n_{\text{Both encdaps}}}$ for n even. Symmetric setups are also fitted once with odd coefficients and once without, and here never an influence is found. These methods work only for the electrostatic potential of the guard, skimmer and endcap electrodes. The geometry of the ring electrode is symmetric with respect to $z = 0$ plane and therefore it always generates a symmetric electrostatic potential. Fitting with and without odd coefficients of the Legendre polynomial shows no difference in the resulting even coefficients and the odd coefficients are compatible with zero. To estimate the systematic uncertainty here, all other electrodes are set to -1 V. This should be the same as setting the ring electrode at 1 V. It provides a good tool so that the analysis of the quality of the simulation does not only rely on the behavior of the simulation through changing the resolution, but also checks if the result obeys the linearity of the Maxwell equations. In most of the cases the systematic uncertainty is larger than the statistical uncertainty. The reason for the systematic uncertainty is unknown but it is probably based on limited numerical precision or on the meshing algorithm. Although the geometry is made to be perfectly symmet-

ric regarding mirroring at the $z = 0$ plane, Comsol Multiphysic's meshing algorithm starts simultaneously at different points to build the mesh. It is not mandatory that the resulting mesh is symmetric. On top the limitation of the numerical precision adds up of course. But even though the systematic uncertainty is up to 10000 times larger than the statistical uncertainty, they are always 1000 times less than the model uncertainties and hence can safely be omitted.

4.1.4 Influence of the guard electrodes

This section describes how the uncertainties of the guard electrodes propagate through the simulation into the resulting electrostatic potential. It is shown how smoothing the edges of the guard electrodes and moving the guard electrodes axially changes the electric potential.

When the guard electrodes are constructed in Comsol Multiphysics the edges are sharp. To some degree, this is compensated for by the mesh which cannot reproduce edges with a bending radius of zero. But still, the edges are much sharper than they are in reality and this affects the electrostatic potential in the trap center. Therefore a fillet with a radius of 5 µm is added to the inner edge, as shown in Figure 4.5. This edge is chosen because it is the closest to the trap center. It changes the mesh significantly at the edges of the guard electrodes but not in the center of the trap. The value of 5 µm is used because the manufacturing tolerances are of the same order [VDJ90]. The relative change of the fit-coefficients in case this fillet is added is given in Table 4.4. In Table 4.2 and 4.3 the fit-coefficients are simulated with fillet added to the inner guard electrode edge. As expected, the biggest shift occurs for the D_n-coefficients, which all decrease by roughly 1.5 %. The coefficients with and without fillets are related via $D_{\text{with fillet}} = (1 + \mathcal{F}_{\text{rel}})D_{\text{without fillet}}$, where $\mathcal{F}_{\text{rel}}$ is the shift factor. There is no large deviation from this 1.5 % value for all D_n. Due to the results of Section 4.1.2, a mesh influence can be excluded as a reason for this change, so this deviation must stem from the shape change of the guard electrodes caused by the usage of the fillet. Probably the very small bending radius increases the strength of the higher-order terms. If the fillets are added,

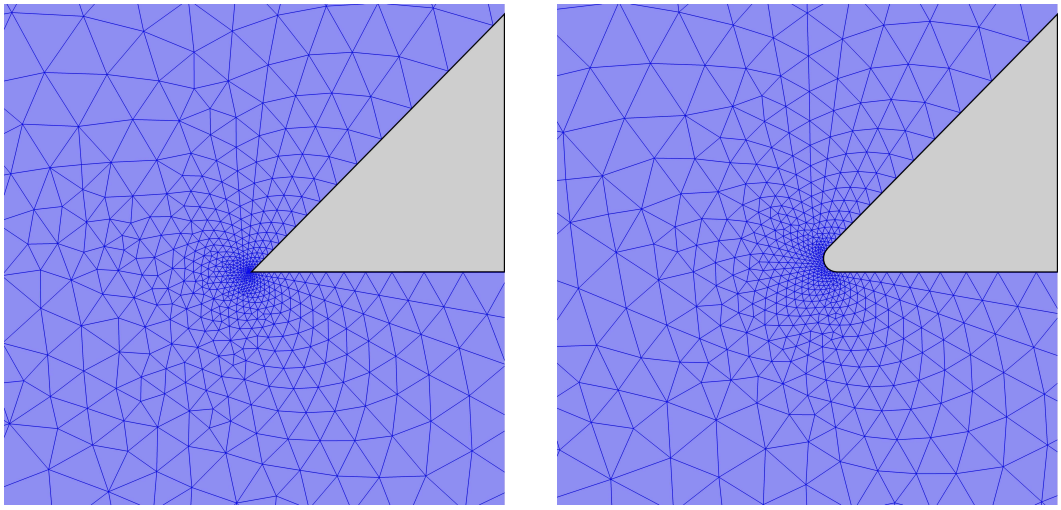

Figure 4.5: Zoom into the inner edge of the guard electrodes in the geometry shown in Figure 4.1, including just a coarse mesh for clarity. In the left picture the edge has a bending radius of zero. Since the mesh cannot reproduce this bending radius it rounds the edge a little. In the right picture a fillet with a radius of 5 µm is introduced.

the strength of these higher-order terms drop. Also, as expected, S_n and E_n do not change in the regime of a few percent, because their electrostatic potential is not much affected by the shape of the guard electrodes. The only other change in a range of a few percent occurs for R_4, which decreases by 1.2 %. The reason for this is unknown, but possibly because the guards are close to the ring electrode, the shape of the guard electrode also matters for the higher-order terms of the potential generated by the ring electrode. Anyhow, this shift compensates for the shift of D_4 almost completely. In general, adding the fillet of 5 µm is an improvement of the model, since the machining tolerances of the real electrodes are of the same order of magnitude. The exact bending radius of the inner edges is unknown, but it is known that there is a bending radius and 5 µm is in the right order. Even today manufacturing tolerances are not much better. Hence, adding the fillets shifts the fit-coefficients in the right direction. To give an uncertainty for this shift is difficult. A bending radius of more than 10 µm would be visible in the technical drawing [VDJ90] and below 2.5 µm was technically not possible when the electrodes were manufactured. Hence, the bending radius is likely to be between 2.5 – 7.5 µm, and hence half of the observed shift due to adding the fillets contributes to

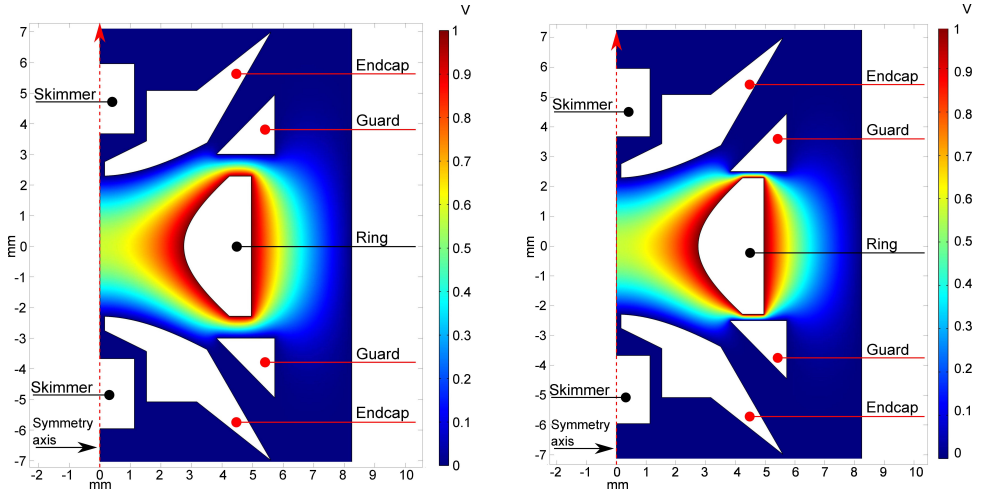

Figure 4.6: Rotationally symmetric model as described in Figure 4.1. The ring is set to 1 V. On the left hand side, the guards are at their normal position, on the right hand side the guard electrodes are moved exemplarily 300 µm closer to the ring electrode, which has a visible impact on the electrostatic potential, at least near the guard electrodes.

the final model uncertainty of the fit-coefficients, shown in Tables 4.2 and 4.3.

As a next test the potential is calculated when the guards are moved closer and further away from the ring electrode as displayed in Figure 4.6. It is expected that such a displacement will affect coefficients of every electrode. To give an example, the effect on the R_2 coefficient is shown in Figure 4.7. For each specific guard position a resolution study is performed and the statistical uncertainty is calculated as explained in Section 4.1.2. The guards are moved by $\pm 150\,\mu\text{m}$ in steps of $50\,\mu\text{m}$. On the fitted coefficients (see Figure 4.7) a linear fit is applied with $f(z) = a_\text{G}\, z + b$. The resulting a_G-coefficients for each S_n, E_n, D_n and R_n are given in Table 4.4. The product $a_\text{G} \cdot z$ describes by which total amount the corresponding coefficient changes, if the guard electrodes are moved by z from their default position. Within the chosen limits of $\pm 150\,\mu\text{m}$, the linear approximation is valid. For even larger displacements, a quadratic term becomes visible, but these kind of large shifts are geometrically unrealistic, and hence the quadratic term is ignored. For the final fit-coefficients an uncertainty of $50\,\mu\text{m}$ in the guard position is assumed. This is again a conservative choice, because the distance between the guard and ring electrode is measured to be around 1 mm and the uncertainty

Table 4.4: Dependence of the fit-coefficients on adding fillets and position shifts to the guard electrodes. See text for the definitions of a_G, $\mathcal{P}_{rel}$ and $\mathcal{F}_{rel}$. The second column gives the relative shift of the final fit-coefficients (Tables 4.2 and 4.3), if the guard electrodes position is shifted by 50 µm. The third column gives the relative shift of the fit-coefficients, if the fillets with a radius of 5 µm are added to the inner edges of the guard electrodes.

	a_G mm^{-1-n}	Position shift $\mathcal{P}_{rel}$	Fillet shift $\mathcal{F}_{rel}$
S_1	$2.88 \cdot 10^{-10}$	$3.49 \cdot 10^{-05}$	$-1.11 \cdot 10^{-03}$
S_2	$1.94 \cdot 10^{-11}$	$1.90 \cdot 10^{-06}$	$-3.91 \cdot 10^{-04}$
S_3	$5.52 \cdot 10^{-11}$	$1.95 \cdot 10^{-05}$	$-1.10 \cdot 10^{-03}$
S_4	$5.81 \cdot 10^{-12}$	$1.97 \cdot 10^{-06}$	$-3.69 \cdot 10^{-04}$
E_1	$-1.31 \cdot 10^{-03}$	$3.94 \cdot 10^{-04}$	$1.39 \cdot 10^{-04}$
E_2	$2.24 \cdot 10^{-05}$	$1.02 \cdot 10^{-05}$	$-1.18 \cdot 10^{-05}$
E_3	$-6.30 \cdot 10^{-04}$	$3.02 \cdot 10^{-03}$	$-4.07 \cdot 10^{-04}$
E_4	$1.87 \cdot 10^{-04}$	$4.04 \cdot 10^{-03}$	$-1.87 \cdot 10^{-02}$
E_5	$1.81 \cdot 10^{-04}$	$5.22 \cdot 10^{-03}$	$1.32 \cdot 10^{-03}$
E_6	$-1.98 \cdot 10^{-06}$	$5.72 \cdot 10^{-03}$	$-1.42 \cdot 10^{-02}$
D_1	$5.71 \cdot 10^{-03}$	$8.98 \cdot 10^{-02}$	$-1.49 \cdot 10^{-02}$
D_2	$-2.37 \cdot 10^{-04}$	$4.77 \cdot 10^{-02}$	$-1.44 \cdot 10^{-02}$
D_3	$-1.10 \cdot 10^{-04}$	$9.12 \cdot 10^{-03}$	$-1.49 \cdot 10^{-02}$
D_4	$-5.55 \cdot 10^{-04}$	$5.19 \cdot 10^{-02}$	$-1.49 \cdot 10^{-02}$
D_5	$-2.76 \cdot 10^{-04}$	$4.28 \cdot 10^{-01}$	$-1.50 \cdot 10^{-02}$
D_6	$2.76 \cdot 10^{-05}$	$5.35 \cdot 10^{-02}$	$-1.49 \cdot 10^{-02}$
R_2	$2.07 \cdot 10^{-04}$	$9.41 \cdot 10^{-05}$	$1.15 \cdot 10^{-05}$
R_4	$5.15 \cdot 10^{-04}$	$8.51 \cdot 10^{-02}$	$-1.22 \cdot 10^{-02}$
R_6	$-2.52 \cdot 10^{-05}$	$1.48 \cdot 10^{-01}$	$-1.49 \cdot 10^{-02}$

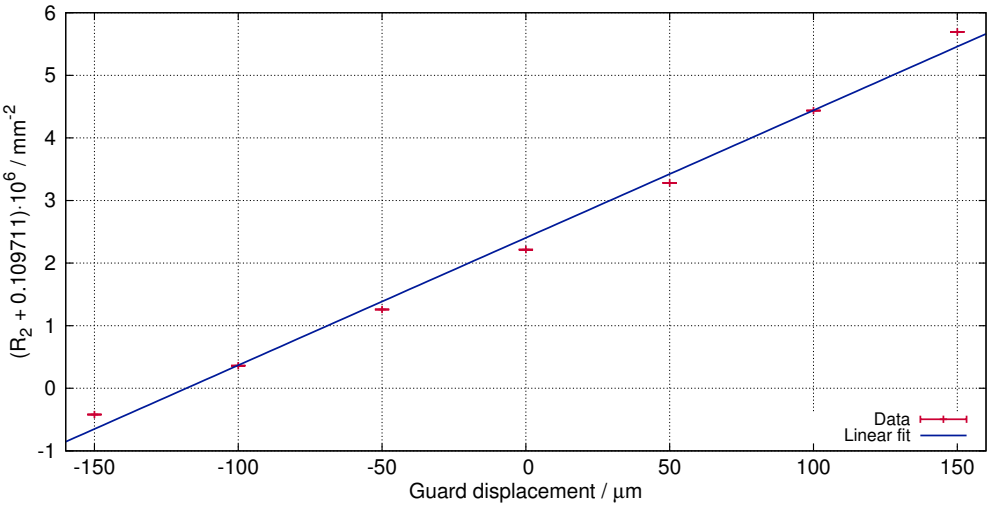

Figure 4.7: R_2 fit-coefficient (see Table 4.1) at different distances of the guard electrodes from the ring electrode. The solid line is a linear fit to the data. The simulation is done with the geometry shown in Figure 4.1. The uncertainty of each individual point is calculated as explained in Sections 4.1.2 and 4.1.3. A positive guard displacement means that the guards are shifted further away from the ring electrode, a negative the opposite. At zero the guard electrode position is as in Figure 4.1.

is assumed to be 5 % of this value. In the assembling procedure possibly some play is introduced and position shifts occur. For completeness, this would shift the endcap electrodes as well. But since not all shifts can be investigated, only the guard position shift is taken into account. Probably this one is overestimated, but it should give a sense for the influence of model uncertainties on the final fit-coefficients. The second column in Table 4.4 shows the relative shift factor $\mathcal{P}_{\text{rel}}$ of the fit-coefficients, if the guard electrodes are shifted by 50 µm. The coefficients with and without shift are related via $D_{\text{with shift}} = (1 + \mathcal{P}_{\text{rel}}) D_{\text{without shift}}$, where $\mathcal{P}_{\text{rel}}$ is the shift factor. The fit-coefficients in Table 4.2 and 4.3 are given without the 50 µm shift. Like in the case of the added fillet, the D_n change the most and here they change even more. This is reasonable, because the electrostatic potential in the center of the trap generated by the guard electrodes depends of course on the distance of the guard electrodes. The shift of R_4 is also significant and, again, larger than by adding the fillets. This validates the claim that the electrostatic potential by the ring electrodes depends also on the shape and distance of

the guard electrodes, because they are only 1 mm apart. Again, D_4 and R_4 are shifted in the same direction, but here they do not compensate each other completely. The S_n coefficients are less affected, because the electrodes are further away and covered up by the endcap electrode. Fortunately, the main coefficients R_2, R_4, D_2 and D_4 are changed by a few percent or even less, because from these coefficients direct conclusions for the experiment are drawn in Section 4.4.

4.1.5 Thermal shrinking

The design of the trap electrode geometry is documented in Reference [VDJ90]. These design values are specified for the trap electrodes at room temperature. When the Penning-traps are used in the experiment, they are at 4 K. This cooldown changes the geometry as explained in Section 3.1. Due to the different thermal shrinking coefficients of oxygen-free high thermal conductivity copper (OFHC) and Macor, these changes are not a pure rescaling of the trap electrodes, but also their position relative to each other changes. This leads to the problem that the surface of the endcap electrodes is not an equipotential surface of a quadrupole potential anymore. In this section the changes of the electrostatic potential, when the trap is cooled down from room temperature to 4 K, are discussed.

It should be noted that if the geometry is just rescaled because it assumed that all materials have the same thermal shrinking coefficient α, the resulting change of the dimensionless fit-coefficients is not statistically significant. The new fit-coefficients can be calculated via the relation $R_{n_{\text{shrunken}}} = (1 - \alpha_{\text{copper}})^n R_{n_{\text{not shrunken}}}$. In the case with different shrinking coefficients the effect is tremendous. In Table 4.5 the factor is given by which the fit-coefficients change, if thermal shrinking is taken into account. Calculating the coefficients after shrinking can be done as follows:

If the shift factor is called $\mathcal{S}$, then $R_{n_{\text{shrunken}}} = (1 + \mathcal{S}_n) R_{n_{\text{not shrunken}}}$. For the simulation of the fit-coefficients in Table 4.2 and 4.3 thermal shrinking is applied. To be compatible with the uniform shrinking the resulting shift should be between $-0.33\,\%$ for $n = 1$ and $-1.62\,\%$ for $n = 6$. For none of the fit-coefficients, this is the case. The S_n coefficients

Table 4.5: Relative change of the fit-coefficients in %, with thermal shrinking applied. The different thermal shrinking coefficients of copper and Macor are taken into account. The shift factor $\mathcal{S}$ can be obtained by dividing the values with 100. More information in the text.

S_1	S_2	S_3	S_4	E_1	E_2	E_3	E_4	E_5	E_6
71.8	71.0	71.1	70.7	−0.01	−1.09	−1.43	16.0	−7.93	0.54
R_2	R_4	R_6		D_1	D_2	D_3	D_4	D_5	D_6
−1.15	3.12	22.4		10.4	41.1	10.9	8.66	4.54	9.71

are changed the most with about 70 %. This is probably based on the fact that their absolute value is the smallest one. While the second order ring coefficient R_2 is shifted by 1.2 %, the fourth and sixth order coefficient are shifted by 3 % and 22 %, respectively. D_2 is shifted by 40 %. This comes from the different kind of materials that is used in the trap setup. Due to the difference in z_0' and z_{0b}' (see Table 3.1) the endcap electrode surfaces are not an equipotential plane in a quadrupole potential anymore. The simulation shows that the thermal shrinking and especially the shift of the endcap position has to be taken care of. In future traps, the Macor holder should be designed in the way that after the cooldown the endcap electrode surface is an equipotential surface of a quadrupole potential. Now, the relative change of the fit-coefficients of up to 40 % compared to the non-shrunken trap electrodes influences the conclusions for the experiment, such as the guard constant and the optimal guard voltages (see Section 2.2.1) up to 40 % as well. For the final fit-coefficients S_n, E_n, D_n and R_n (see Tables 4.2 and 4.3) half of the shift due to the thermal shrinking is taken as contribution for the model uncertainty. This choice is reasonable because the thermal shrinking coefficients have a spread of up to 50 % and the given uncertainty for the fit-coefficient should just give an estimate of their reliability.

4.1.6 Effect of the holes in the endcap electrodes

For any ion transfer between the traps, the ion must pass through the holes in the endcaps. The transfer was and still is a challenging task, and hence the idea came up to enlarge the holes in the experiment trap. This section discusses the influence of the

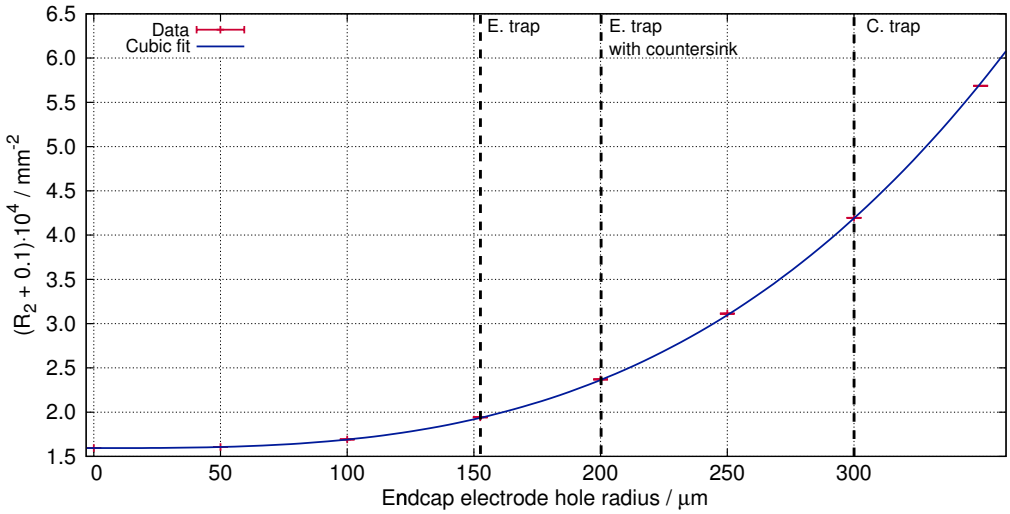

Figure 4.8: R_2 fit-coefficient (see Table 4.1) with different radii of the hole in the endcap electrodes. The solid blue line is a cubic fit to the data. The simulation is done with the geometry shown in Figure 4.1. For each datapoint also a resolution study as described in Section 4.1.2 is done. The vertical lines indicate the hole radii of the different traps.

hole in the endcap electrodes on the fit-coefficients. For this, the radius of the hole in the endcap electrodes is varied from 0 to 300 µm. For each voltage setup defined in Table 4.1, a resolution study is performed like in Section 4.1.2. For R_2, the results are plotted in Figure 4.8. The coefficients have a cubic dependence on the hole radius. Thus, for fitting a cubic polynomial of the kind $f(r) = a_{\mathrm{H}}\, r^3 + b_{\mathrm{H}}$ is used. The resulting a_{H} and b_{H}-coefficients for different voltage setups and different fit-coefficients are given in Table 4.6. In the second and third column of Table 4.6, the relative shift $\mathcal{H}$ of the fit-coefficients is shown, if the hole radius is increased by 5 µm. The coefficients are related as follows $R_{n_{\mathrm{new}}} = (1 + \mathcal{H}) R_{n_{\mathrm{old}}}$, where $R_{n_{\mathrm{new}}}$ has the enlarged hole. For the experiment trap $R_{n_{\mathrm{old}}}$ is 200 µm and for the capture trap 300 µm. This is taken as contribution for the final fit-coefficient as model uncertainty (see Tables 4.2 and 4.3), because the uncertainty of the hole radius is of the same size. It is a proof of the reliability of the simulations that the cubic dependency of the fit-coefficients on the radius of the hole in the endcap electrodes as predicted in Reference [BG86] is now confirmed by simulations. The most dominant effect occurs for the E_n fit-coefficients. They shift 0.03 ‰

Table 4.6: Dependency of the fit-coefficients on the hole radius in the endcap electrodes. The coefficients a_{H} and b_{H} are defined in the text. The fourth and fifth column show the relative change of the final fit-coefficient for the capture and experiment trap (Tables 4.2 and 4.3), respectively, if the hole radius is varied by 5 µm.

Coeff$_n$	a_{H} mm^{-3-n}	b_{H} mm^{-n}	C. trap $\mathcal{H}_{\mathrm{c}}$	E. trap $\mathcal{H}_{\mathrm{e}}$
E_1	$-1.15 \cdot 10^{-2}$	$1.661 \cdot 10^{-1}$	$-6.48 \cdot 10^{-5}$	$-4.15 \cdot 10^{-5}$
E_2	$-1.12 \cdot 10^{-2}$	$1.100 \cdot 10^{-1}$	$-9.53 \cdot 10^{-5}$	$-6.09 \cdot 10^{-5}$
E_3	$-3.86 \cdot 10^{-3}$	$1.044 \cdot 10^{-3}$	$-3.49 \cdot 10^{-4}$	$-2.23 \cdot 10^{-4}$
E_4	$-3.21 \cdot 10^{-3}$	$2.569 \cdot 10^{-4}$	$-1.40 \cdot 10^{-2}$	$-8.33 \cdot 10^{-3}$
E_5	$-1.02 \cdot 10^{-3}$	$-1.648 \cdot 10^{-4}$	$5.29 \cdot 10^{-3}$	$3.54 \cdot 10^{-3}$
E_6	$-8.25 \cdot 10^{-4}$	$-1.066 \cdot 10^{-5}$	$3.30 \cdot 10^{-2}$	$2.86 \cdot 10^{-2}$
D_1	$1.77 \cdot 10^{-4}$	$3.178 \cdot 10^{-3}$	$5.21 \cdot 10^{-5}$	$3.34 \cdot 10^{-5}$
D_2	$3.08 \cdot 10^{-4}$	$-2.508 \cdot 10^{-4}$	$-1.17 \cdot 10^{-3}$	$-7.45 \cdot 10^{-4}$
D_3	$5.93 \cdot 10^{-5}$	$-6.024 \cdot 10^{-4}$	$-9.24 \cdot 10^{-5}$	$-5.91 \cdot 10^{-5}$
D_4	$8.67 \cdot 10^{-5}$	$-5.347 \cdot 10^{-4}$	$-1.52 \cdot 10^{-4}$	$-9.74 \cdot 10^{-5}$
D_5	$1.56 \cdot 10^{-5}$	$-3.232 \cdot 10^{-5}$	$-4.56 \cdot 10^{-4}$	$-2.90 \cdot 10^{-4}$
D_6	$2.17 \cdot 10^{-5}$	$2.556 \cdot 10^{-5}$	$7.86 \cdot 10^{-4}$	$5.06 \cdot 10^{-4}$
R_2	$1.07 \cdot 10^{-2}$	$-1.098 \cdot 10^{-1}$	$-9.12 \cdot 10^{-5}$	$-5.83 \cdot 10^{-5}$
R_4	$3.05 \cdot 10^{-3}$	$2.779 \cdot 10^{-3}$	$8.78 \cdot 10^{-3}$	$6.05 \cdot 10^{-3}$
R_6	$1.90 \cdot 10^{-4}$	$-1.485 \cdot 10^{-5}$	$-2.70 \cdot 10^{-1}$	$-5.44 \cdot 10^{-2}$

– 20 ‰ for both traps. This is expected because if the hole radius changes, the surface of the electrode changes. The influence seems to grow with the order n. This is probably based on the fact that E_n decreases with increasing order and hence, the relative shift grows. The same occurs for R_6. It shifts relatively by $-17.3\,\%$ for the capture and $-5.44\,\%$ for the experimental trap and R_6 passes zero roughly at 270 µm hole radius. The D_n are less affected by the hole radius, probably because the guard electrodes are screened by the side of the endcap electrodes. The dependency of the S_n could not be determined reliably, because there the screening by the endcap electrodes is way larger. But the absolute values of S_n are so small that those are already challenging to determine. If they are more screened by the endcap electrodes because of a smaller hole, these coefficients are lost in numerical uncertainties.
Additionally, the influence of the countersink in the endcap electrodes is investigated. For this, the electrostatic potential of the endcap electrodes is simulated once with and without the countersink. The countersink behaves in the same way as a bigger hole in the endcap does. No additional higher-order terms are visible or other shifts occur that are larger than the statistical and systematic uncertainties.

4.2 Vector Fields Opera - Tosca 13.0 vs. Comsol Multiphysics 4.2a

Another test of Comsol Multiphysics' reliability is the comparison of the results obtained with a two-dimensional model with those obtained with a three-dimensional model. For the three-dimensional case, there already exist fit-coefficients from simulations performed with Vector Fields Opera [Sch11]. There, a CAD model was used that is based on the technical hand-drawings which were used for manufacturing the trap electrodes. In this section this CAD model is used in Comsol Multiphysics again to evaluate the results with Vector Fields Opera and to check if the applied rotational symmetry in Section 4.1 brings any benefits. It should be noted that in the CAD model the segmentation of the guard electrodes is also removed to avoid meshing problems.

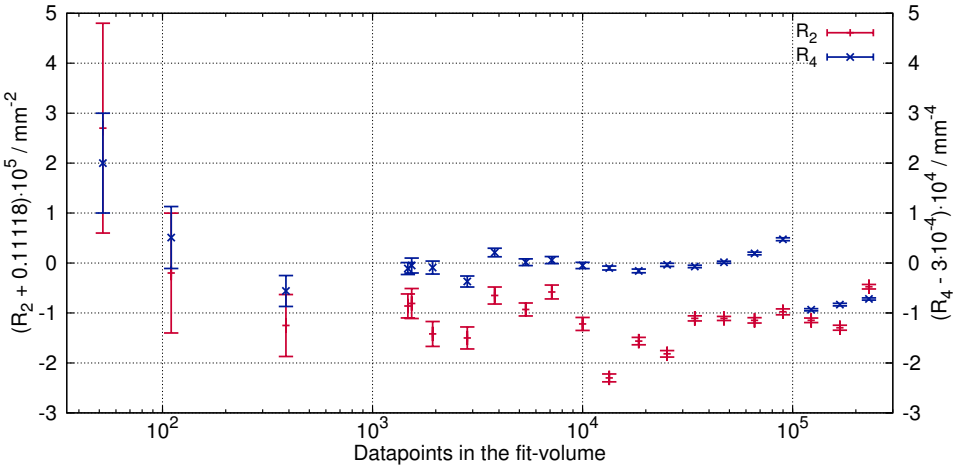

Figure 4.9: R_2 and R_4 fit-coefficients (see Table 4.1) at different resolutions, when a sum to the sixth-order of Legendre polynomial (see Equation (2.13)) is applied as fit. The resolution of the simulation is increasing with the "Datapoints in the fit-volume". The simulation is done with the CAD geometry shown in Reference [Sch11]. The uncertainties are calculated as explained in Section B.1.

In the following, a resolution study is performed as explained in Section 4.1.2, but no further tests, for example guard displacements. After the simulation has finished, the coordinates of the mesh, including the electrostatic potential values, are exported and fitted by Equation (2.13), as in the two-dimensional case in Section 4.1.2. The fit is applied on datapoints inside of a cylinder whose geometrical center is equal to the origin of the simulation. The cylinder has a diameter of 1 mm and a height of 1 mm, similar to the rectangle in the two-dimensional case (see Section 4.1.2), rotated around the symmetry axis (see Figure 4.1). The fit function is used as defined in Equation (2.13), where in the three-dimensional case the coordinates are $r^2 = x^2 + y^2 + z^2$ and $\cos(\theta) = z/\sqrt{x^2 + y^2 + z^2}$. The fit-coefficients are named in Table 4.1. A sum to the sixth-order of Legendre polynomials is chosen as fit function. As in Section 4.1.2, the R_2-coefficient is chosen to be the displayed case (see Figure 4.9). At the step to the highest resolution a large scatter is visible. Overall, there is no clear convergence to a certain value, unlike for the two-dimensional simulation. This indicates that the simulation is still unstable and dependent on the resolution. It becomes more obvious for

R_4. First it seems that the simulation converges for 10^4 elements in the fit volume, but then a jump of 15 – 20 % occurs. At the same number of datapoints in the fit-volume, the two-dimensional simulation has converged already. But the comparison is not completely fair because the datapoint density is higher in the two-dimensional case. The reason for this scatter is unknown, but due to the three dimensions in the simulation, the linear equation system (LES) that needs to be solved in the simulation grows with the power of three with the number of points in the fit volume, instead of two as for the two-dimensional case. Even though the number of datapoints used for fitting is the same as in the two-dimensional case, at this resolution the three-dimensional model around the fit-volume needs a lot more mesh cells to be approximated as accurately as in the two-dimensional case. This is known under the name of "curse of dimensionality". Hence the LES becomes way larger than in the two-dimensional case and depending on the algorithm for solving the LES, possibly variables that are needed to store the intermediate data in the process have an overflow. Also, when the values that are stored in the variables become larger the absolute precision drops [BM08] and the numerical uncertainty increases. It is plausible that the overflow is corrected to some degree due to underlying software, so it does not affect the R_2 and D_2 as much as R_4. It was not possible to increase the resolution further, because the simulations failed for a higher number of points. The reason for this is also unknown. One explanation is that the size of a mesh becomes too small and numerical uncertainties dominate or the Java runtime environment, where Comsol Multiphysics runs, fails if more than 16 GB of RAM is used.

Compared with the simulations performed with the two-dimensional model the statistical uncertainties are up to three orders of magnitude larger (see Table 4.7). The sixth-order coefficient is not given, because due to its uncertainty it is almost compatible with zero. The two-dimensional simulation is a lot better: even the tenth-order fit-coefficient is statistically significant. This validates the choice to simulate the electrostatic properties with the two-dimensional model.

Table 4.7 shows the comparison of R_2, R_4 and D_2, D_4 obtained with different simulation

Table 4.7: Comparison between Tosca, Comsol-3D and Comsol-2D. The values for Tosca are taken from [Sch11], the values for Comsol-3D are explained here, and values for Comsol-2D are taken from Table 4.3.

Coeff. / mm^{-n}	Tosca	Comsol-3D	Comsol-2D
R_2	$-0.11118(2)$	$-0.1111902(2)$	$-0.10995768209(7)$
$R_4 \cdot 10^4$	$3.0(2)$	$2.649(6)$	$3.02494(2)$
$D_2 \cdot 10^4$	$-2.13(4)$	$-1.976(1)$	$-2.482813(7)$
$D_4 \cdot 10^4$	$-4.88(4)$	$-4.861(4)$	$-5.34031(4)$

programs. The values in the column denoted "Tosca" are based on Reference [Sch11], Comsol-3D results are from the simulation with the three-dimensional model explained here, and the values for Comsol-2D are from Table 4.3. For Comsol-3D the same model as in Comsol-2D is used, additionally rotated by 360° around the z-axis. In the simulations using Tosca Vector Fields Opera an investigation of the systematic uncertainties did not take place. Hence for all fit-coefficients only the statistical uncertainty is given. Tosca and Comsol-3D are consistent with each other for R_2, R_4 and D_4. For D_2 they deviate by 8 %. Nevertheless for both the same model is used and thus the differences are mainly due to different meshing algorithms. Especially the guard electrodes have sharp edges which need to be reproduced by the mesh. The statistical uncertainties of Comsol-3D are one order of magnitude smaller than in Tosca. This is expected, because in Tosca Vector Fields Opera the meshing algorithm needed manually-set fixed points to be able to mesh the model. These manually-set fixed mesh points propagate through the simulation and are evident as structure in the residuals of the fits. Compared with Tosca, the meshing algorithm in Comsol Multiphysics is more robust. There is no need to set manually fixed points to help Comsol Multiphysics build the mesh for the simulation. Also no structure is found in the residuals of the fits. In the three-dimensional simulation the mesh never failed, and in the two-dimensional simulation it failed four times at very high resolutions. Also the opportunity to fit multidimensional Legendre polynomials on the raw data of the simulation directly solves a problem that occurred in Reference [Sch11]. In that work, a one dimensional polynomial is used for fitting the

electrostatic potential along the z-axis. It was necessary to interpolate the potential values on the z-axis, because the potential is only calculated at the position of the vertices of the mesh. This leads to the problem that neither the mechanism of the interpolation nor the total number of mesh cells in the Tosca Vector Fields Opera simulation are known. However the assumed overflow (see Figure 4.9) increases the uncertainty. It can be said that Tosca and Comsol-3D give the same result within the combined uncertainty, but Comsol-3D is better.

The deviation of the two-dimensional and three-dimensional model is both statistically and systematically significant. The relative deviation between Comsol-3D and Comsol-2D varies between 1 % for R_2 and 21 % for D_2. This is caused by the model systematic shifts that are already taken into account in the Comsol-2D case. This is not as bad as it seems at first glance. The whole comparison should compare Tosca with Comsol-3D, because there the same model is used. Between Comsol-3D and Comsol-2D the absolute value is not of the main interest. Here, the same fit routines are used to estimate the statistical error and it turns out that the two-dimensional model is more reliable, because the numeric influence could be reduced and the statistical uncertainty dropped by one order of magnitude. From the options available, it can be concluded that Comsol 2D is the most suitable tool to simulate the electrostatic properties of THe-Trap. Even though it is not proven that the numerical influence on the fit-coefficients is removed completely in the two-dimensional simulation, compared to the three-dimensional case, it is heavily suppressed. With the two-dimensional simulation, it is possible to simulate higher-order-terms ($n > 4$) reliably which are otherwise hidden by statistical and systematic uncertainties of the three-dimensional simulation.

4.3 Image charge simulations

In the sections before, the simulations investigated electrostatic effects that are based on the deviation from the ideal Penning-trap electrodes. The image charge effect, explained in Section 2.2.3, occurs in the ideal as well as in the real Penning-trap. In this

section the simulated image charge shift for THe-Trap including the uncertainties is presented. For the simulation the same model as in Section 4.1 is used. In addition to the electrostatic simulations before, here a point-charge with one elementary charge is placed in the trap. This point-charge violates the cylindrical symmetry, if it is not placed on the z-axis and hence a three-dimensional model of the THe-Trap electrodes is needed. To obtain this model, the two dimensional model described in Section 4.1 is rotated by 360° around the z-axis. In the simulation, the point-charge is moved in steps of 100 µm from -500 µm to 500µm along the x-, y- and z-axes. As usual, the origin of the coordinate system is in the center of the Penning-trap electrodes. In each step, first, the electric field of the point-charge and the resulting surface charge density on the surface of the electrodes is simulated. Then the point-charge is removed, and based on the surface charge density the resulting image charge field is calculated. The electric field components of the image charge field are evaluated at the former position of the point-charge. After the whole sweep from -500 µm to 500 µm is performed, the electric field components are fitted by $f(x_i) = c_i x_i^3 + \mathcal{E}_i x_i$, where i denotes the direction of the displacement of the point-charge. The cubic term is just taken to improve the fit quality. In the calculations later on it is neglected, because it is dominated by the linear term for small ion amplitudes and would require a more complicated mathematical treatment, which would not lead to an improved result of $\mathcal{E}_i$ because the change of the result is smaller than its uncertainty. Since $\mathcal{E}_x$ and $\mathcal{E}_y$ are simulated individually, the resulting $\mathcal{E}_\rho$ is calculated as $\mathcal{E}_\rho = 1/2\,(\mathcal{E}_x + \mathcal{E}_y)$. The final result including the uncertainties is given in Table 4.8. The reached accuracy of 2 % for $\mathcal{E}_\rho$ and $\mathcal{E}_z$ is excellent. It has to be taken into account that in order to obtain the image charge shift, two simulations have to be performed, where the second is based on the result of the first one, and the uncertainty of the simulations add up. Also the need for a three-dimensional model decreases the accuracy of the simulation, as seen in the electrostatic simulations before. In Table 4.8 the influence of the different sources of uncertainty like thermal shrinking, hole radius in the endcap and systematic deviations is given. To estimate the systematic uncertainty, Comsol Multiphysics is tested on a case with a known analytic solution.

Table 4.8: Final values and uncertainties of electric field gradients $\mathcal{E}_\rho$, $\mathcal{E}_z$ and $\Delta\nu_c$ for the experiment trap. The image charge shift $\Delta\nu_c$ is calculated by Equation (2.31) with $B_0 = 5.26\,\mathrm{T}$. The second column gives the final value including the final uncertainty. The third and the fourth column give the uncertainty due to thermal shrinking and hole radius in the endcap electrode, respectively. The fifth column describes the uncertainty of the fit which determines $\mathcal{E}_i$ (see Table 4.9) and the sixth column gives the uncertainty due to systematic deviation in the spherical simulation. The frequency shift $\Delta\nu_c$ is given per elementary charge. More details in the text.

	Final	Uncertainty			
	Value	thermal	hole	stat	systematic
$\mathcal{E}_\rho$ /mVm^{-2}	42.3(9)	0.8	0.06	0.04	0.4
$\mathcal{E}_z$ /mVm^{-2}	80.4(1.3)	1.0	0.04	0.05	0.8
$\Delta\nu_c$ /mHz	−2.50(3)	0.029	0.0019	0.0014	0.017

This is the image charge field effect inside a sphere. Investigating the image charge effect for different hole radii in the endcap electrodes and assuming an uncertainty of the hole radius of 5 µm also leads to a 1 % uncertainty for $\mathcal{E}_i$. Taking the thermal shrinking into account and using 50 % of the shift due to thermal shrinking as uncertainty leads to 2 % uncertainty of $\mathcal{E}_i$.

In the following the individual investigations are explained in more detail. Even though for the image charge effect in a real Penning-trap no analytic description exists, the image charge effect of a point-charge in a sphere (see Section 2.2.3) has an analytic solution. Hence this case is simulated with Comsol Multiphysics for a sphere with a radius of $r = 2.77\,\mathrm{mm}$, which is equal to the distance from the center to the ring electrode ρ_0' of THe-Trap. This tests the general reliability of the simulation of the image charge effect. For the simulation, the point-charge is moved along the x-axis within ± 500 µm in 100 µm steps. The x-axis is chosen without loss of generality. To compare the simulation with the analytical solution, the electric field components obtained from the simulation with the point-charge being placed at different positions are fitted by a cubic polynomial $f(x) = a_{\mathrm{Sphere}} x^3 + b_{\mathrm{Sphere}} x$, where x is the position of the point-charge and a_{Sphere} and b_{Sphere} the fit-coefficients. The influence of the cubic coefficient is clearly visible (see Figure 4.10), but only at ion amplitudes that are unlikely and even there the cubic term is dominated by the linear term, and hence the cubic term is safely omitted.

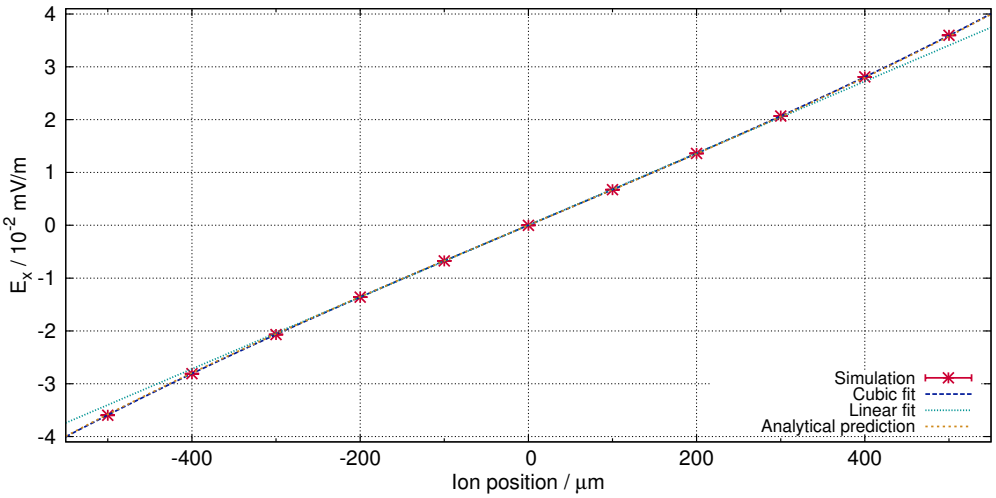

Figure 4.10: Electrostatic field component of the image charge in the x-direction, if the ion is placed at different positions along the x-axis. For the simulation, a sphere with a radius of 2.77 mm is assumed. The analytical solution is calculated from Equation (2.23).

The constant and quadratic term can be neglected due to symmetry reasons. The **analytical prediction** for b_{Sphere} is 67.77 mV/m^2, based on Equation (2.23). The uncertainty of the analytical prediction, which is based on the uncertainty of the elementary charge and the vacuum permittivity is negligible on the here given precision. The **simulated value** is $67.28(1)$ mV/m^2, if a cubic polynomial is used for fitting and $68.1(3)$ mV/m^2, if only the linear term is used. The uncertainties denoted in parenthesis are the $1\,\sigma$ uncertainty of the fit. The deviation of b_{Sphere} between the simulation, where a_{Sphere} is taken into account for the fit, and the analytical prediction is 0.9 %. The deviation of the cubic term is 2.7 %. To obtain the coefficient, a resolution study is performed. As in Section 4.2 already, the three-dimensional simulation is still visibly influenced by the resolution chosen, even at the highest available resolution. But the result approaches the analytical solution. Hence, the coefficients simulated at the highest resolution are taken.

In the following, for the linear coefficient also in the simulation of the Penning-trap case an systematic uncertainty of 1 % is assumed. Even though the deviation of the hyperbolic geometry in THe-Trap from a sphere is obvious, it is difficult to estimate the

Table 4.9: Simulated electrostatic field gradient components of the experiment trap of THe-Trap created by an elementary point charge at different positions and fitted by a cubic polynomial with and without thermal shrinking being applied.
The $1\,\sigma$ uncertainty of the fit is given in parenthesis. More details in the text.

Model	$\mathcal{E}_x$	$\mathcal{E}_y$	$\mathcal{E}_z$
	$\mathrm{mV/m^2}$	$\mathrm{mV/m^2}$	$\mathrm{mV/m^2}$
Design	41.44(4)	41.44(5)	82.38(5)
4 K	42.24(7)	42.25(4)	80.36(5)

systematic uncertainty of the simulation in a different way. The applied tests from the electrostatic simulations (Section 4.1.3) are not usable here, because all electrodes are grounded.

In the next test, the three-dimensional model of the THe-Trap electrodes is used. To estimate how model uncertainties affect the result also the non-shrunken trap electrodes are simulated. The result is given in Table 4.9. As expected, $\mathcal{E}_x$ and $\mathcal{E}_y$ are compatible within the fit uncertainty because even though the cylindrical symmetry is broken by the point-charge, the resulting image charge effect should be the same for displacements in the x- and y-direction. Therefore the relation $\mathcal{E}_x = \mathcal{E}_y \equiv \mathcal{E}_\rho$ introduced in Section 2.2.3 is validated. The difference between $\mathcal{E}_z$ and $\mathcal{E}_\rho$ in the shrunken and not shrunken model is significantly larger than the statistical uncertainty. The shift of the $\mathcal{E}_z$ and $\mathcal{E}_\rho$ goes in different directions, because during the cool-down the ring electrode surface comes closer to the trap center while the endcap electrodes are shifted further away. For the final cyclotron shift, half of the deviation of $\mathcal{E}_\rho$ and $\mathcal{E}_z$ between the shrunken and not shrunken case is taken as uncertainty. The reasons for this choice are the same as in the investigation of the thermal shrinking effect on the fit-coefficients (see Section 4.1.5). That is the biggest input with 1.6 % of the total value of $\mathcal{E}_\rho$ and $\mathcal{E}_z$, but compared with the electrostatic simulations before, where for example D_2 changed by 40 % upon thermal shrinking, the image charge simulations seem to be more robust against the influence of the model uncertainties. To investigate the other geometric influences, the hole radius in the endcap electrodes in the shrunken model is varied from 0 µm to 300 µm in 50 µm steps and a quadratic

dependency is found to be $\mathcal{E}_\rho(\tilde{r}) = \left(5.8(1.2) \cdot 10^{-6}\,\tilde{r}^2\,\mu\mathrm{m}^{-2} + 42.25(3)\right)\ \mathrm{mVm}^{-2}$ and $\mathcal{E}_z(\tilde{r}) = \left(-1.78(23) \cdot 10^{-5}\,\tilde{r}^2\,\mu\mathrm{m}^{-2} + 80.92(8)\right)\ \mathrm{mVm}^{-2}$, where $\tilde{r}$ is the radius of the hole in the endcap electrode. The $1\,\sigma$ uncertainty of the fit is given in parenthesis. A quadratic dependency is expected because the image charge effect depends on the surface area where the image charge effect occurs and the area of the hole in the endcap depends quadratically on the radius. Also $\mathcal{E}_z$ changes more rapidly than $\mathcal{E}_\rho$ if the hole radius is enlarged because the endcap electrodes generate mainly an electrostatic field gradient in z-direction ($\mathcal{E}_z$). The uncertainty of the gradients for the experiment trap having a hole radius of 200 µm including the countersink with an uncertainty of 5 µm is given in the fourth column of Table 4.8. In general, it can be stated that the image charge simulation is successful. Even though a three-dimensional model has to be used, the statistical uncertainty is negligible and the deviation in the spherical test case is sufficiently low with 1 % to assume that the simulation gives a reasonable result. The result obtained here is compared with experimental values in Section 4.4.

4.4 Conclusions for the experiment

In the previous section the method to obtain the final fit-coefficients to describe higher-order terms in the electrostatic potentials as well as the investigations to prove their reliability were discussed. It turned out that the influence of the mesh size and the uncertainties based on the violation of the superposition principle in the electrostatics are negligible. The effect of uncertainties in the simulated model on the final fit-coefficients are orders of magnitude higher. Nevertheless, it is possible to reliably determine the fit-coefficients up to fourth order. These coefficients are also used to calculate trap-specific parameters (see Section 2.2.1). In the following, based on the final fit-coefficients of the experiment trap these specific parameters are calculated and compared with the experimental values.

The simulated **guard constant**, c_{guard}, defined in Equation (2.18) turned out to be $-440(95)$ for the experimental trap. This is based on the 21 % uncertainty of D_2 which

is caused by the uncertainty of the thermal shrinking effect. An extra measurement of the guard constant at the experiment gives a result of $-806(30)$. This is a deviation of 89 % or $\sim 4\,\sigma$ of the simulation result. This significant difference cannot be explained by any failure in the simulation. Probably a detail is missing in the simulated model causing the D_2 to shift even further. It is shown that especially this coefficient is sensitive to model changes. But so far there is no indication which detail is missing. Further experimental effects like patch charges and high radial amplitudes are not taken into account and can also at least partly explain the deviation. The patch charges were not simulated because for this the amount and the distribution of the patch charges must be known. Unfortunately there is not any reliable piece of information available about this but first tests of simulating this effect have shown that the result depends strongly on the distribution and amount of patch charges.

The **optimal guard voltage** is introduced in Section 2.2.1. In THe-Trap mass measurements with $^{16}O^{5+}$ using $^{12}C^{4+}$ as a reference mass are performed to test and understand the apparatus [SEH+14]. These ions are used because their mass ratio is known very well. For $^{12}C^{4+}$, a ring electrode voltage of $-87.63\,\mathrm{V}$ and a guard electrode voltage of $-42.98\,\mathrm{V}$ is used [Str14]. From the simulated R_4 and D_4 the optimal guard voltage should be $-49(5)\,\mathrm{V}$. This is a deviation of 12 % or approximately $2\,\sigma$ of the simulation. For $^{16}O^{4+}$, a ring electrode voltage of $-93.46\,\mathrm{V}$ and a guard electrode voltage of $-46.36\,\mathrm{V}$ is used [Str14]. Here, the simulation predicts an optimal guard voltage of $-53(6)\,\mathrm{V}$. This is a deviation of 13 % or $1.1\,\sigma$. The optimal guard voltage for $^{16}O^{5+}$ almost agrees with the simulation within $1\,\sigma$. In the experiment the optimal guard voltage is not independent of the ion species, as it should. This indicates that there are other effects involved that are not taken into account. Possibly further deviations of the geometry or also patch charges can cause this difference. Even though the simulation gives a result of the optimal guard voltage which is in the right order of magnitude, it not possible to predict the optimal guard voltage by a simulation because, in the experiment, the guard voltages has to be adjusted to a few 10 meV to be optimal. This requires a 100 times better precision in the simulated fit-coefficients. From the statisti-

cal and systematic uncertainty this is possible, but it will not be possible to describe the model simulated accurately enough. Also, the fact that the simulated optimal guard voltages is systematically too high indicates that possibly some effects in the model are overlooked.

The **simulated image charge shift** turned out to be $2.50(3)$ mHz per elementary charge for the experimental trap. The uncertainty of 1 % is sufficiently low, because the image charge shift in the experiment is a 10^{-10} effect. An uncertainty of 1 % is therefore at a level of 10^{-12}. The result is in perfect agreement with the experimental value. In Reference [VDJPVLZ06], where a trap is used that has the same geometry as THe-Trap, the image charge shift was measured as $2.23(9)$ mHz per charge at a magnetic field of 5.9 T, which corresponds to 2.5(1) mHz per charge in the lower magnetic field of THe-Trap. Simulating the image charge effect in the THe-Trap geometry directly confirms this measurement. This helps the experiment directly, because the image charge effect is a systematic frequency shift that has to be corrected for.

In general, the simulated values agree well with the experiment. The largest deviation occurs in the guard constant. The D_2 has shown its strong dependence on model parameters, and it could be that there are other influences that have not been taken into account yet.

It is shown that increasing the hole radius in the endcap – which may help in the transport of the ion – will also increase the non-harmonic part of the electrostatic potential.

Generally, the simulation can be used for a better understanding of electrostatic properties of the trap geometry and to estimate, if a measured effect is of the right order of magnitude. The reliability of the simulated coefficients, as for example R_n and D_n is probably not good enough to be used for correcting the measured data for some effects that are for example described in Reference [KEH$^+$14]. For this, the knowledge of the real trap geometry itself is insufficient.

Chapter 5

Magnetic field simulations

In this chapter the influence of the THe-Trap setup on a homogenous magnetic field is discussed. As introduced in Section 2.2.2, the higher order field deviations of the magnetic field shift the frequencies of the ions. For these simulations a full three-dimensional CAD model as described in [Sch11] is used, because also other parts of the setup in addition to the already introduced electrodes can influence the magnetic field. Unlike in the electrostatic simulations, the exact dimensions of structures used are not of high relevance, but the amount and the magnetic the susceptibility of the material is. Therefore, the existing CAD model is suitable. For the simulation the concept of superimposing magnetic fields is used. Each part of the beam line and the trap electrodes (see Section 3.1) is simulated individually, while all others are removed completely from the simulation model. It is assumed that the distortion by the individual parts is so small that the change in the boundary conditions for the other simulated parts can safely be ignored.

The used magnetic susceptibilities χ are given in Table 3.2. The relative permeability μ_r is defined as $\mu_\mathrm{r} = 1 + \chi$. Unfortunately, the crucial parameter χ has an uncertainty of 20 %. This uncertainty is based on the fact that the exact amount of the constituents of the alloys used are unknown and this can have a massive influence on the resulting χ. Independent of the chosen mesh size, the simulation result is more precise than 20 % and hence a resolution study, as in Section 4.1.2 to investigate the influence of the mesh

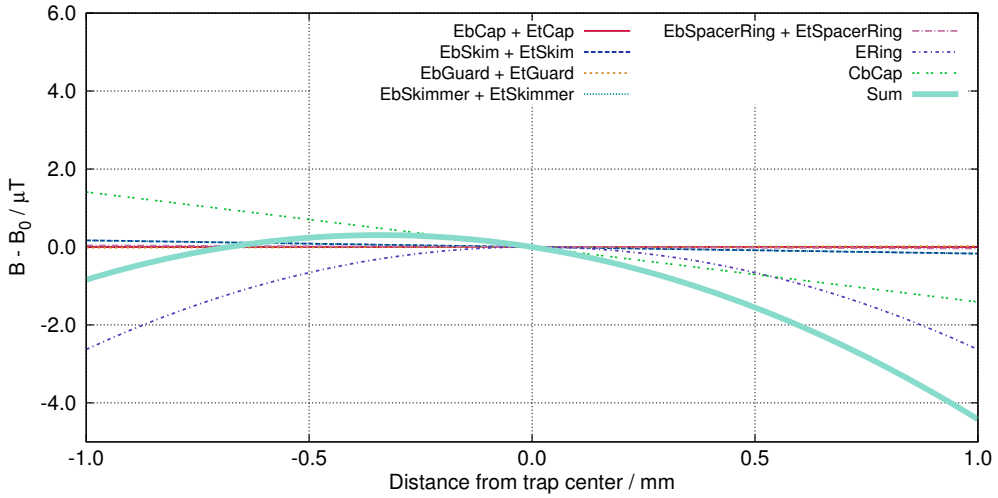

Figure 5.1: Deviation from B_0 around the center of the experiment trap caused by the different parts of the experimental setup. The thickest line displays the sum of the influences of all parts that have a significant impact. Insignificant parts, like the ion capture segment and FEP, are not included.

size on the result is deemed unnecessary and thus is not performed.

The results of the simulation are fitted with the function defined in Equation (2.21) up to second order. The fit is applied along the z-axis only and hence radial terms (ρ-terms) can be neglected. The actual fit function looks as follows

$$\tilde{B}^{(z)}(z) = \tilde{B}_0 + \tilde{B}_1\, z + \tilde{B}_2\, z^2 \quad . \tag{5.1}$$

All coefficients are normalized to the constant magnetic field term B_0, where $\tilde{B}_i = B_i / B_0$. It is assumed that the constant term B_0 is equal to 1 T and pointing upwards, as indicated in Figure 2.1. This function is fitted on the simulation results for the trap center of the capture and experiment trap in a range of ± 0.5 mm around the center. This range is chosen because the ion amplitude is well within this limit (see Reference [Str14]). The statistical significant contribution to the magnetic field distortion in the experiment trap is shown in Figure 5.1. The impact is considered to be statistically significant, if the value of the resulting fit-coefficient, obtained from fitting Equation (2.21) to the simulated magnetic field, is statistically significantly different from zero. Therefore many

parts, as for example the ion capture segment, the feedthrough flange and most of the holding structure made of Macor displayed in Figure 3.1, are not listed. Due to their large distance from the trap center their influence is negligibly small. For all parts except for ERing the $\tilde{B}_1$-coefficient dominates. This is caused by the individual positions with respect to the trap center (see Figure 3.2). ERing has only a $\tilde{B}_2$-coefficient due to its symmetrical position and shape around the trap center. The resulting fit-coefficients for the experiment and the capture trap are given in Table 5.1. To estimate the systematic uncertainty, it can be assumed that for example the change of the magnetic field by the ring electrode of the experimental trap in the center of the experiment trap should be the same as the change of the magnetic field by the ring electrode of the capture trap in the center of the capture trap. The deviation is taken as uncertainty of the simulation. For $\tilde{B}_2$ only the ring electrode appears to have a significant impact. For $\tilde{B}_1$ multiple part contributions are found which are shown in Figure 5.1. Summing up the $\tilde{B}_1$ terms and calculating the resulting uncertainty by Gaussian error propagation leads to a value that is compatible with zero within the calculated uncertainty. This is not unexpected, because the experiment and capture trap are made to be symmetric regarding their horizontal plane. This leads to the fact that for example the $\tilde{B}_1$ created by the upper endcap electrode is canceled out by the $\tilde{B}_1$ of the lower endcap electrode. That symmetry is only broken by CbCap (see Figure 3.2). But its $\tilde{B}_1$-term is partly compensated by the other electrodes and the remaining $\tilde{B}_1$-term is not significant. The parts of the experimental setup which violate this symmetry further, for example beamline and feedthrough flange, do not create a significant $\tilde{B}_1$. The different absolute value of EbCap and EtCap, as well as CbSkimmer and CtSkimmer is within 2σ and hence not significant. A simulation of the whole trap geometry at once is not possible, because building the mesh failed every time. This is caused by the mounting holes in the setup which are already included in the CAD model, and whose properly remodeling in the mesh is difficult. To avoid this, every single hole must be closed or an approximation of the whole setup has to be modeled in Comsol Multiphysics. The 0.4 % relative uncertainty of $\tilde{B}_2$ is underestimated.

Table 5.1: Influence of different parts of the experiment setup on the magnetic field at the center of the experiment and capture trap. In the simulation the magnetic field is pointing upwards. The names are defined in Figure 3.2. The magnetic susceptibilities used for the individual materials are given in Table 3.2. The abbreviation OFHC stands for oxygen-free high thermal conductivity copper and PB for phosphor bronze. The coefficients $\tilde{B}_1$ and $\tilde{B}_2$ are defined in Equation (5.1).

Name	Material	Experimental Trap		Capture Trap	
		$\tilde{B}_1$ $\cdot 10^{-4}\,\mathrm{m}^{-1}$	$\tilde{B}_2$ $\cdot 10^{-1}\,\mathrm{m}^{-2}$	$\tilde{B}_1$ $\cdot 10^{-4}\,\mathrm{m}^{-1}$	$\tilde{B}_2$ $\cdot 10^{-1}\,\mathrm{m}^{-2}$
CbCap	PB	$-1.41(36)$	-	$4.66(24)$	-
CtCap	PB	-	-	$-4.66(24)$	-
CbSkimCap	Macor	-	-	$-3.08(6)$	-
CtSkimCap	Macor	-	-	$2.88(5)$	-
CbSkimmer	OFHC	-	-	$1.21(7)$	-
CtSkimmer	OFHC	-	-	$-1.33(2)$	-
CbGuard	OFHC	-	-	$-2.83(8)$	-
CtGuard	OFHC	-	-	$2.81(12)$	-
CbSpacerRing	Macor	-	-	$1.43(1)$	-
CtSpacerRing	Macor	-	-	$-1.45(4)$	-
CRing	PB	-	-	-	$-2.64(1)$
EbCap	PB	$4.42(24)$		-	-
EtCap	PB	$-4.42(24)$		$1.77(36)$	-
EbSkimCap	Macor	$-3.02(6)$		-	-
EtSkimCap	Macor	$2.83(5)$		-	-
EbSkimmer	OFHC	$1.14(7)$		-	-
EtSkimmer	OFHC	$-1.31(2)$		-	-
EbGuard	OFHC	$-2.91(8)$		-	-
EtGuard	OFHC	$2.93(12)$		-	-
EbSpacerRing	Macor	$1.43(1)$	-	-	-
EtSpacerRing	Macor	$-1.47(2)$	-	-	-
ERing	PB	-	$-2.63(1)$	-	-
	Σ	$-0.38(53)$	$-2.63(1)$	$-2.64(1)$	$-0.36(53)$

Table 5.2: Influence of a nickel coating used in the feedthroughs, when the nickel coating has saturated. The influence coefficients do not scale for stronger magnetic fields. The used magnetic susceptibility for nickel is given in Table 3.2. The coefficients $\tilde{B}_1$ and $\tilde{B}_2$ are defined in Equation (5.1). The last column gives the total volume of nickel in the simulation. The dimensions of the nickel coating are given in the text.

Nickel coating thickness / μm	Experiment trap $\tilde{B}_1$ $\cdot 10^{-1}\mathrm{m}^{-1}$	Experiment trap $\tilde{B}_2$ m^{-2}	Capture trap $\tilde{B}_1$ $\cdot 10^{-1}\mathrm{m}^{-1}$	Capture trap $\tilde{B}_2$ m^{-2}	Amount mm^3
50	−1.71	4.85	−0.23	0.44	104
25	−1.55	4.40	−0.20	0.38	52

The only purpose of the simulation is to give a rough estimate of the influence of the different parts of the experimental setup on the magnetic field. For more reliable values greater effort in analyzing the materials used is needed.

A measurement with a single ion led to an experimental $\tilde{B}_1$ of $17 \cdot 10^{-4}\,\mathrm{m}^{-1}$ [Str12]. This deviation cannot be explained by incorrectly chosen magnetic susceptibilities. Clearly something is missing. A $\tilde{B}_2$ value has not been measured so far, but is in progress and will be published in Reference [Hö15]. In Seattle a $\tilde{B}_2$ of $0.08\,\mathrm{m}^{-2}$ was measured [VL04], but afterwards the experiment was shipped to Heidelberg and the value is not reliable anymore. It should be noted that there are other influences on the magnetic field, such as manufacturing imperfections in the coils of the superconducting solenoid and possibly alloys used that are not known so far. Also some parts of the beamline are welded and this can influence the magnetic susceptibility as well [AJ86]. For an estimate, it is assumed that all 24 feedthroughs in the feedthrough flange are covered by a 50 μm and in a second estimate by a 25 μm nickel coating. This coating is represented by a cylinder with a height of 7 mm and an outer radius of 2 mm. Nickel is sometimes added to improve the soldering properties of the feedthroughs. The resulting magnetic field terms are given in Table 5.2. In this case these results are not to scale to the 5.3 T magnet used. Nickel is a ferromagnetic material. The field inside of the nickel coating saturates, when it is exposed to external fields that have a strength of a few Tesla. For nickel at 4 K the maximal magnetization is found to be 0.645 T [Stu12].

As expected, the ferromagnetic material has an influence which is one order of mag-

nitude larger for $\tilde{B}_2$. In addition, a significant $\tilde{B}_1$ occurs in the experimental trap. The effect on the magnetic field in the capture trap is smaller, because it is 41 mm further away. Since these massive $\tilde{B}$-coefficients are not seen experimentally, it looks like no nickel coating was used in the feedthroughs. But it shows that even a tiny amount of ferromagnetic material as a constituent of an alloy can significantly influence the magnetic field.

In general, the simulation gives reasonable results that agree with the applied consistency checks but the simulation does not confirm the experimental value. It is shown in the simulations that the different parts of the THe-Trap setup cannot create the experimentally seen higher order magnetic field distortions, if the assumed magnetic susceptibilities are correct. Also already tiny amounts of ferromagnetic alloys can change the magnetic field more than it has been experimentally seen. This leads to the conclusion that with the simulation, assumed or feared contaminants by ferromagnetic materials can be investigated and, for the nickel coating at the feedthroughs, also excluded. To correct for the effects explained in Section 2.2.2 with the simulated $\tilde{B}$-coefficients is not possible, because the knowledge on the alloys used and on the magnetic susceptibilities is not sufficient. Probably other effects are more dominant like soldering and welding, magnetic materials or inhomogeneities in the magnet itself.

Chapter 6

Characterization of the Penning-ion source

THe-Trap is equipped with an external Penning-ion source. This ion source helps to reduce the contamination of the traps with the gas to be ionized, by creating the ions outside of the actual Penning-traps. Especially for the use of tritium gas this is crucial because the emission of β-decay electrons ionize rest gas and releases particles from the electrodes. The ionized rest gas interacts with the ion of interest and disturbs the measurement at a level of 10^{-9} which is 1000 times higher than the aimed precision.
When ions are created in the Penning-traps directly an electron beam is emitted by the FEP and accelerated towards the trap center of the experiment Penning-trap. The beam spreads out and hence not all electrons are reflected by the EtSkimmer electrode and a few hit and stick to the surface of the endcap electrode. These are the patch charges which influence the electrostatic potential and their creation can be prevented by using the external Penning-ion source.
This chapter is about the characterization of the external Penning-ion source, using the the Faraday cup described in Section 3.3. At first a cathode for creating milliamperes of electron current is analyzed in Section 6.1 and in Section 6.2 a beam of ^{4}He ions is produced, investigated and optimized. The vacuum part of the experiment where the

Penning-ion source is located is separated by a gate valve from the vacuum part where the Penning-traps are located. This avoids spoiling the vacuum with the gas from the Penning-ion source.
It should be noted that the main focus is not put on the efficiency of the Penning-ion source, but to analyze the Penning-ion source for the first time while it is mounted at the experiment, and to investigate the dependency of the created ion beam on the operating parameters of the Penning-ion source. The efficiency is not of such a big interest because all is needed in the trap is a single ion.

6.1 Cathode characterization

To generate ions in the Penning-ion source, first an electron beam is produced by applying a current of roughly 2 A through a thoriated tungsten filament (see Section 3.2). The emitted electrons are accelerated by setting proper voltages to the electrodes and by electron impact ionization the ions are created. This section discusses the characterization of the thoriated tungsten filament used as cathode. The filament has a diameter of 0.15 mm and contains 1 % thorium.
The characterization is one of the first tests of the functionality of the custom-designed Faraday cup. For measuring the current at the Faraday cup a Keithley 6514/E picoamperemeter is used. It is of interest how stable the electron emission is on the scale of a few minutes up to an hour, as this is the timescale for loading ions. The timescale of an hour is of interest for testing and optimizing ion loading procedures. For investigating the stability of the thoriated tungsten filament, different heating currents is applied and the current of the extracted electron beam is measured at the collimator-plate. Before the measurement is started, 1.9 A are applied to the filament to preheat the ion source. The Penning-ion source is operable after a few minutes. After each measurement, the heating current is switched off for one minute. It is observed that the heating current drops by roughly 2 % over the first 30 minutes, even when the voltage of the heater source is kept constant. But it does not effect the emitted electron current (see

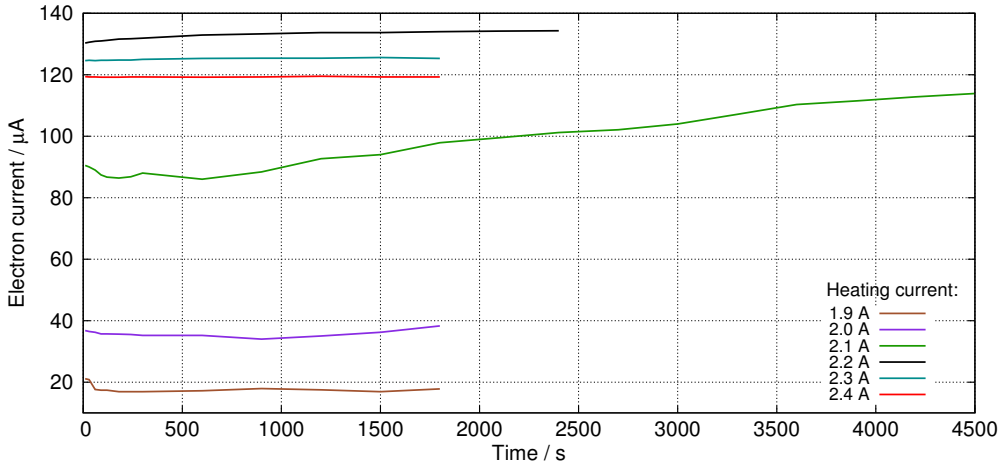

Figure 6.1: The electron current measured at the collimator plate as a function of time for different heating currents applied to the thoriated tungsten filament cathode.

Figure 6.1). An explanation is that the thoriated tungsten filament heats up its surrounding structure. It takes some minutes to reach an thermal equilibrium. The heated surrounding structure also acts back on the thoriated tungsten filament and increases its temperature further. If the electrical resistance rises with the filament's temperature which is a likely behaviour for metal wires, and the voltage is kept constant the heating current has to drop. Another explanation is that the thoriated tungsten filament expands thermally, becomes thinner and hence has a bigger electrical resistance. Also in this case the heating current drops. The measured electron current is stable within a drift of less than 5 % for all chosen heating currents and durations, and less than 2 % after the first 5 minutes, except for 2.1 A. The strong drift for an applied heating current of 2.1 A, with an increase of 13 %, can be repeated in other measurements within two following days. This effect is clearly not an error in the measurement and is well reproducible. Possibly the thorium atoms rearrange themselves over a longer period of time. It is shown in Reference [Lan23] that the amount of thorium influences the emission current by many orders of magnitude and due to the heating of the filament, the thorium atoms at the surface move and evaporate. Also, the thickness of the thoriated tungsten filament can change over time by thermal expansion.

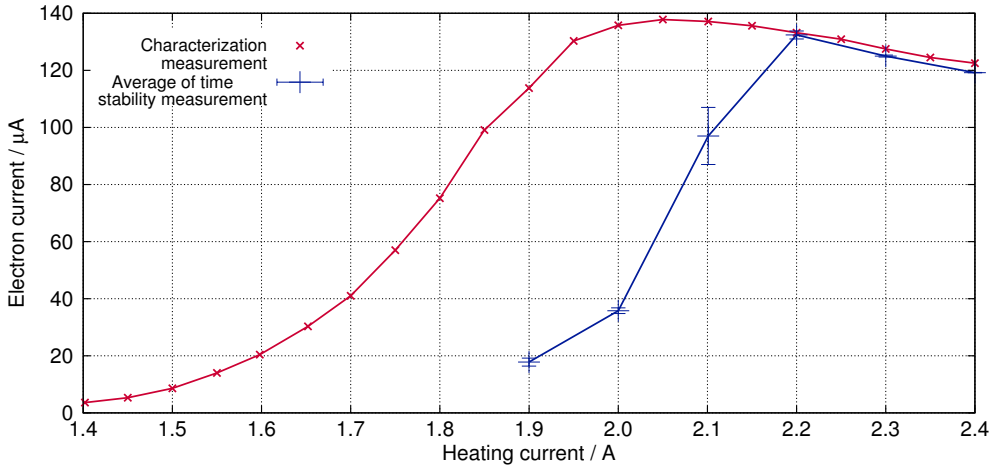

Figure 6.2: In red, electron current measured at the collimator-plate with different heating currents applied to the cathode. For each datapoint after increasing the heating current by 0.05 A, five minutes are spent waiting for the filament to reach its thermal equilibrium. In blue, the average of the stability measurement of each heating current, taken from Figure 6.1. The measurement for the red curve took place a few days after the measurement for the blue curve. The uncertainties of the datapoints are one standard deviation of the average of each time stability measurement.

A week later the characteristic emission curve of the filament is taken (see Figure 6.2). It qualitatively shows a behavior that is expected from Figure 6.1. The electron current measured at the collimator-plate rises with increased heating current, reaches its maximum and finally decreases a little bit. For an easier comparison the average for each individual heating current of Figure 6.1 is plotted in Figure 6.2. While the value of the actual characterization is taken five minutes after setting the heating current and represents only one measurement, the average of the time stability measurement includes possible drifts. At first glance, this comparison seems to be unreasonable, but the drift of the electron emission current in a range from five minutes to an hour in the stability measurement is less than 2 %. Hence the emitted electron current can be assumed as constant. At the steepest slope, the measurements are shifted by 0.3 A to higher heating currents, which is a relative shift of roughly 16 % in the heating current. This shift cannot be explained by measurement uncertainties. Here the characteristic curve of the filament has changed. The characteristic curve reaches approximately the same

maximum as in the stability measurement, but at different heating currents. At the same heating current both curves deviate by up to a factor of 7. This fluctuation from measurement to measurement in different weeks is probably based on fluctuations in the amount of thorium at the surface of the filament. After a short amount of time, mostly minutes, the filament reaches an equilibrium and is stable for the next hours, but through the cooldown and the next heating up the thorium atoms at the surface are rearranged or the thickness of the thoriated tungsten filament changes by thermal expansion. This leads to the conclusion that the electron emission of the tungsten filament is stable for several minutes to hours. Probably the electron emission current is even stable for a longer time than hours. This could offer the opportunity to keep the ion source running, while a mass measurement takes place and so the characteristic of the Penning-ion source does not change within one mass measurement. Then it should be possible to load the ions remotely from a computer. This has the advantage that loading the ions can be automatized.
Overall the Faraday cup has shown its principal functionality and the thoriated tungsten filament works nicely. It provides an intense beam of electrons that can reliably be detected with the Faraday cup. When the Penning-ion source is set up each time, the emission current is stable mostly within 5 %, and this is sufficient for the further investigations of the ion beam. This is an improvement compared to the barium cathode which was characterized by M. Tremer [Tre11]. There, the electron emission current fluctuated by a factor of two over two hours.

6.2 Ion beam optimization

After characterizing the cathode, further tests of the Penning-ion source with an electron beam are performed. It was tried to increase the emitted electron current as far as possible. The setup which provides the most intense electron beam is given in Table 6.1 in optimization step #0. It turns out that after some iterations the ratio of the electron beam measured at the cup- and collimator-plate is around 0.1 and the total

Table 6.1: Overview of the settings applied at the Penning-ion source during the optimization of the ion beam. Fields marked with "…" are scanned and with "–" are not set or applied in this optimization step. Measurement # 0 was done with an electron beam, all other measurement with 99.99 % of pure helium injected into the Penning-ion source. The Einzel lenses E_1–E_5 are given in Figure 3.4. For the measurements 5 and 6 the voltage V_1 is -185 V and V_2 is 13 V.

Optimization/#	Pressure mbar	Cup position mm	Heating current A	Solenoid current A
0	$1 \cdot 10^{-10}$	5.5	1.9…2.4	0
⋮	Optimizing for example the solenoid current, V_{Anode}			
5	$9 \cdot 10^{-7}$	0…24	2.6	1.5
6	$3 \cdot 10^{-7} \ldots 3 \cdot 10^{-4}$	4.5	2.25	1.5

Optimization/#	V_{Anode} V	V_{grid} V	$V_{electrons}$ V	V_{repel} V	V_{einzel} V	E_1 V	E_2 V	E_3 V	E_4 V	E_5 V
0	100	–	200	80	200	V_2	V_2	V_2	V_2	V_2
⋮	and the other parameters									
5	100	20	205	80	198	V_1	V_2	V_1	V_2	V_1
6	100	20	205	80	198	V_1	V_2	V_1	V_2	V_1

current measured at the collimator is around 70 µA. The Faraday cup is operated in the diagnostic position. The ratio is defined as $I_{cup} / I_{collimator}$. The area of the cup-plate that faces the beam in the diagnostic position is $1.05^2 \pi\,\text{mm}^2$. The area of the collimator is $(90 - 2\pi \cdot 1.05^2)\,\text{mm}^2$. For this it is approximated that the collimator-plate has an area of $90\,\text{mm}^2$ facing the beam, if it is in the diagnostic position, and from this the area of the holes must be subtracted. The ratio between the area of the cup- and collimator-plate is 0.04. Because the ratio is around 0.1, probably the electron beam is already focused or cut by the geometry of the einzel lenses.

Next, the electron beam is used to create ions and the ion current is optimized. For this 99.99 % pure helium gas is let in. Near the turbomolecular pump, which is located next to the Penning-ion source, a pressure of $9 \cdot 10^{-7}$ mbar is measured. It is higher in the ion source itself. The total current at the cup-plate as well as the ratio between the plates is observed while tuning the voltages of the electrodes. The important optimization steps can be seen in Table 6.1. After four iterations with inserting gas and before

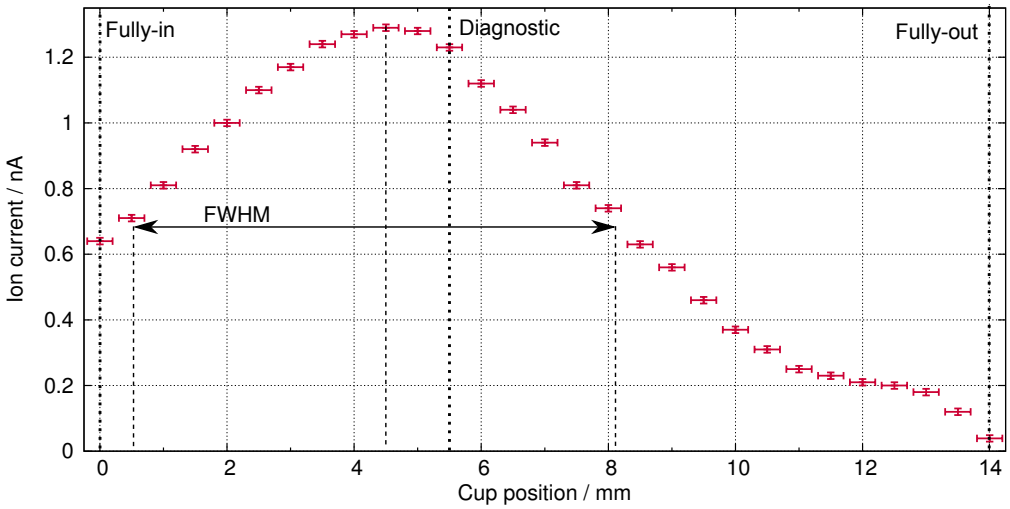

Figure 6.3: Ion current measured at the cup-plate as a function of displacement from the fully-in position (see Figure 3.5). At 5.5 mm the cup is in the center of the beam line. At 13.5 mm the Faraday cup enters the beam line. The uncertainty is ± 0.2 mm for the position of the cup and 0.01 nA for the current reading.

finding the optimal pressure for the ion source, the spatial distribution of the beam is measured. For this, the ion current at the cup-plate is measured at different positions of the Faraday cup in the beamline. First, the cup is in the fully-in position, denoted with 0 mm in Figure 6.3 and then moved out in 0.5 mm steps. The result is shown in Figure 6.3. A maximum is visible at 4.5(2) mm which is 1 mm off from the beamline axis and the full width at half maximum (FWHM) is 7.5(4) mm. Optimally, the beam should have its maximum at position 5.5 mm. Another hint for a tilted beam is that the same beam intensity read at 0 mm is reached again at 8 mm. Since the Faraday cup is used in a vacuum tube of 16 mm in diameter, this should occur at 13.5 mm. This is based on the following idea. If the Faraday cup is fully in, the center of the outer hole (right in Figure 3.5) of the collimator-plate is 2.5 mm away from the wall. Hence, if the Faraday cup is pulled out by 13.5 mm, this hole is at the opposite wall of the vacuum tube and 13.5 mm and 2.5 mm add up to the 16 mm of the beam tube diameter. Beyond 13.5 mm the beam current drops to almost zero as expected because the plates become fully covered by the vacuum tube. That the current does not completely drop to zero is caused by the fluctuating readout of the Keithley picoamperemeter. At the moment, it

cannot be said, if the reason for the poor FWHM is a misalignment perpendicular to the moving axis or a tilt of the whole beam line. It seems that some effort is needed before the first ion can be caught in the trap.

Because of the ion optical parameters, a much smaller FWHM of the ion beam is expected. The shift of the ion beam with respect to center of the beam tube by 1 mm can be explained by a misalignment of the Penning-ion source. There are screws available to adjust the alignment of the ion source with respect to the Faraday cup and the beam line. Unfortunately, to adjust the Penning-ion source the vacuum must be broken. Also a reason for the shift could be an inhomogeneous distribution of materials around the ion path. It has been already tested that if some amount of iron is placed at the beam line, it gets magnetized by the superconducting magnet and therefore influences the path of ions.

Because tritium is radioactive, the use of the gas should be minimized. Thus the pressure dependency of the ion source is of interest. To investigate this dependency, helium gas with 99.99 % purity is let in through an adjustable needle valve. The pressure in the ion source chamber is left to stabilize for a few minutes before the measurement is started. The results are plotted in Figure 6.4. The first value is taken with no gas inserted to observe the rest gas ionization. The beam current is largest in the pressure regime of $10^{-6} - 10^{-5}$ mbar. Overall, when the pressure is increased by a factor of 100, the beam current increases only by a factor of seven. The observed ratio of the currents measured at the cup and collimator-plate is around 0.05 regardless of the pressure. This is worse compared to the measurement with the electron beam only. This is caused by the heavier mass of the ions and the larger energy spread. Therefore, focusing is more difficult for ions than for electrons. Probably the whole beam is misaligned, as it is already indicated by Figure 6.3. The decreasing ion current for pressures larger than 10^{-5} mbar supports the hypothesis that the beam is weakly focused. At higher pressures more ions are created in the Penning-ion source, but due to ion-ion interaction and ion-atom collisions the beam spreads up faster and less ions reach the cup- and collimator-plate. But this pressure regime is not of interest for loading the trap because

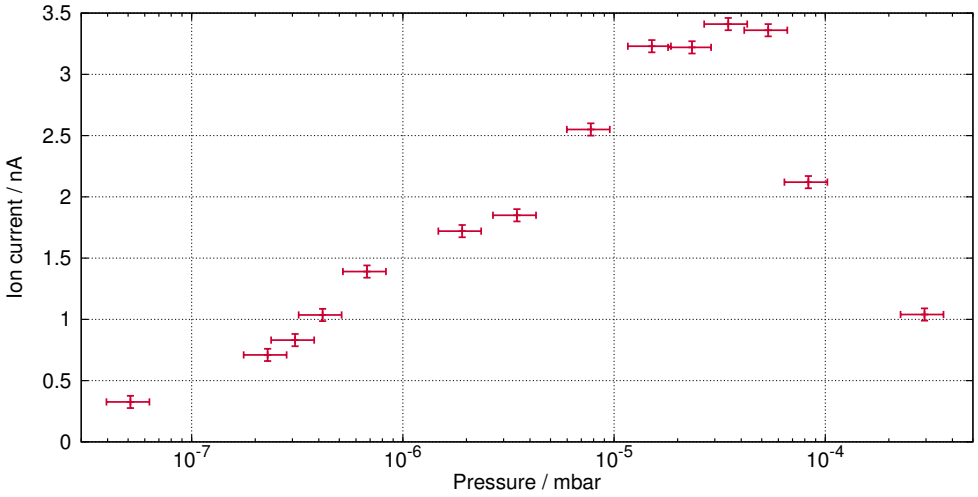

Figure 6.4: Pressure dependency of the ion current at the cup-plate. The pressure is measured at the turbomolecular pump. The uncertainty is 0.01 nA for the current reading. The error of the pressure is approximated by the repeatability of the slack of the needle valve.

it would spoil the vacuum in the center of the trap electrodes. This would lead to a short lifetime of the ions which is at the moment in the range of weeks to month and could drop to minutes or even less. Also this pressure of tritium gas would stop the experiment completely because the electrodes would get contaminated with tritium gas and the emitted β-electron would ionize rest gas in the trap. The resulting ion-ion interaction would prevent any further measurements at a 10^{-11} level.

6.3 Conclusion

The Faraday cup has proven its principal functionality, and the new thoriated tungsten filament works nicely. It makes the work with the ion source much easier compared with the barium tungsten dispenser cathode which was used before. The risk of poisoning the cathode by restgas is negligible and complex heating procedures as in Reference [Pin07] can be skipped.

The work with the helium ion beam is also successful. It was demonstrated that a helium ion beam can be created and its intensity measured with the Faraday cup. In the measurement of the spatial distribution of the Faraday cup it can be seen that the max-

imum is not very sharp which indicates that the beam has a rather defocused shape, evident from Figure 6.3. The ratio between the beam current measured close to the wall and the maximum is 1/2. The beam diverges after leaving the ion optics of the Penning-ion source because the ion optics focuses too weakly. Also the beam appears to be misaligned towards the arm of the Faradaycup feedthrough.

The measurement of the pressure dependency of the Penning-ion source helps the experiment as well. In the future, the idea is to insert helium-3 or tritium gas in pulses. So, it is important to know at which pressure the ion source works best, and it has to be taken care that the neutral gas is pumped away quickly. The regime, where the ion source works best, is too high for the operation with tritium because too much tritium gas would reach the trap. But with this measurement, it is also shown that the ion source works already at pressures slightly higher than 10^{-7} mbar. But already the rest gas level of $3 \cdot 10^{-7}$ mbar which is probably based on the released gas particles when the electron beam hits the electrodes in the ion source, will lead to a problem and reduce the lifetime of the ion. Additionally, helium and tritium are more difficult to pump than for example oxygen. Also a problem is that if an ion beam is created by ionizing mostly rest gas, the beam is not very pure and beside the gas contamination the contamination with other ions can occur. It should be also taken into account that the created ion beam of 1 nA, which means that roughly 10^{10} ions/s are sent downwards, can be enough to get a few ions into the ion capture segment. The efficiency of the ion transfer in a properly aligned beamline is at 10^{-2} to 10^{-3}, described by Reference [Pin07]. But observing the ratio of the current at the cup-plate to the current measured at the collimator-plate in this optimization indicates again that the beam is tilted or shifted. It is likely that this tilt will cause the loss of almost all ions and that here further investigations are needed. The experimental setup offers the opportunity to align the Penning-ion source with respect to the Penning-traps. One hope is also that the magnetic field of the superconducting solenoid helps to focus the beam because all we need is a single ion in the trap.

All in all, the Faraday cup has proven its functionality. It helps to optimize the ion source settings, while the source is mounted at the experiment and there is definitely a good chance to use the Penning-ion source at the experiment.

Chapter 7

Conclusion and outlook

The topics of this thesis were investigating the deviations of the electrostatic potential and magnetic field from the ideal case, and the optimization of the external Penning-ion source. The electrostatic field coefficients S_n, E_n, D_n and R_n of the polynomial approximation were derived with sufficient precision. The analysis code can easily be adapted for other projects. The numerical uncertainties have been lowered to insignificant levels. The current uncertainty of the coefficients is dominated by the uncertainties in the simulated model, such as thermal shrinking, guard electrode position and hole sizes in the endcap electrodes. Here mathematical relations between fit-coefficients and the model parameters are found. For example, the R_n depends on the third power of the hole radius in the endcap electrode. In Appendix A, the fit-coefficients of the polynomial approximation of the electrostatic potential are given with statistical and systematic uncertainties. The individual model uncertainties are chosen conservatively. If it is possible to decrease the model uncertainties, for example through a better knowledge of the THe-Trap electrode geometry, it is possible to give the final fit-coefficients with a higher accuracy by using the derived mathematical relations. For other experiments in the future, Comsol Multiphysics offers the opportunity to simulate the electrostatic properties in advance and, for example, take thermal shrinking into account.
The image charge simulation of the spherical case is successful and the deviation from the analytic solution is only about 1 %. Hence, the image charge simulation in a trap

with hyperbolic electrodes is reliable. The results obtained here depend only weakly on changes in the geometry, and even conservative approximations of the model uncertainties lead to less than 2 % uncertainty of the image charge effect. It is a very good result that the simulated image charge effect confirms the experimental value, which was measured in a similar trap and estimated for THe-Trap.

The image charge has been investigated in different Penning-traps by using different approaches Reference [Por01, SWB13], and it will be an interesting test to simulate these Penning-traps with Comsol Multiphysics and to compare the results. Measuring the image charge effect experimentally is challenging because tests with different number of ions in the trap have to be performed. Here, approximating the effects of ion-ion interactions and determining the number of ions in the trap is difficult. Maybe the simulation can help to increase the accuracy or at least give a strong test of the measurement results.

The magnetic field deviations from the homogeneous field case are approximated by higher order Legendre polynomials whose scaling factors are named $\tilde{B}_1$ and $\tilde{B}_2$. In the simulation of the magnetic field, it turned out that the experimentally seen $\tilde{B}_1$ and $\tilde{B}_2$ cannot be explained by the experimental setup and the known magnetic susceptibilities. The results themselves are reasonable and it does not seem that they are heavily influenced by statistical or systematic uncertainties. Even though the results are not as deeply investigated as in the electrostatic case, they are too far off from the measured $\tilde{B}_1$ of $17 \cdot 10^{-4}\,\mathrm{m}^{-1}$ to be explained by simulation problems. But if there is an improved knowledge of the magnetic susceptibilities of the individual components, or of the inhomogeneity of the magnetic field due to imperfections of the superconducting magnet itself, further simulations can help to understand the magnetic field of THe-Trap better. It should also be tried to simulate the whole model at once to avoid that uncertainties in the fit to determine $\tilde{B}_1$ and $\tilde{B}_2$ individually for each part of the geometry add up. To determine the dependency of these coefficients on the magnetic susceptibility, simulations with the same geometry but different magnetic susceptibilities should be performed. This can help to estimate the influence of the uncertainty of the magnetic

susceptibilities on $\tilde{B}_1$ and $\tilde{B}_2$.

The external Penning-ion source was characterized for the first time while being mounted on the experiment with a custom-designed Faraday cup, built within this thesis. The new thoriated tungsten filament has proven to create an intense electron beam. The Faraday cup is an improvement for the experiment. It was proven to work well, and it provides valuable information about the Penning-ion source, such as the intensity and the position of the beam. The characterization revealed the beam to be misaligned, either because of tilt or because of a parallel offset. This misalignment has to be minimized for shooting the ions down to the Penning-traps. One method of aligning the Penning-ion source with respect to the Penning-traps is to use the mounting screws of the Penning-ion source. Another option is to adjust the ball joint below the ion source. This ball joint allows to tilt the whole room temperature part with respect to the lower cryogenic part. The functionality of the Faraday cup as gas barrier will be tested by loading ions from the Penning-ion source. Monitoring the storage time of the ions in the trap gives an estimate of vacuum quality, and from this it can be concluded, whether the Faraday cup works as a gas barrier or not. This test has not been done yet, because at the moment the experiment is working well, ions are created by using the field emission point (FEP) and lifetimes of weeks to months are achieved. If the test fails, the experiment has to be pulled out of the magnet and heated up, pumped and cooled down to achieve a good vacuum again. Since a new cryogenic amplifier is tested at the moment and further changes in the electronics have to be done in the near future, testing the Faraday cup as a gas barrier will be performed soon before pulling the experiment. Comsol Multiphysics offers other tools that may help to estimate the gas flow from the ion source to the Penning-traps. With these tools, it should be also possible to simulate the ion flight from the Penning-ion source to the Penning-traps, but for this the knowledge on the magnetic field outside of the magnet has to be improved.

Bibliography

[AJ86] D. Atherton and D. Jiles: Effects of stress on magnetization. *NDT International* **19** (1986), 15 .
http://dx.doi.org/10.1016/0308-9126(86)90135-5

[AKC04] J. Angrik and KATRIN-Collaboration: (2004). KATRIN Design Report. *Technical Report*, Kalsruher Institut für Technologie (KIT).
http://bibliothek.fzk.de/zb/berichte/FZKA7090.pdf

[AM00] Y. Akulov and B. Mamyrin: Half-lives of atomic tritium and free triton determined from the chemical shift of the beta decay time constant. *Technical Physics Letters* **26** (2000), 458.
http://dx.doi.org/10.1134/1.1262876

[AWW+14] G. Audi, M. Wang, A. H. Wapstra, F. G. Kondev and M. MacCormick: The 2012 Atomic Mass Evaluation and the Mass Tables. *Nuclear Data Sheets* **120** (2014), 1.
http://dx.doi.org/10.1016/j.nds.2014.06.126

[BB36] H. A. Bethe and R. F. Bacher: Nuclear Physics A. Stationary States of Nuclei. *Reviews of Modern Physics* **8** (1936), 82.
http://dx.doi.org/10.1103/RevModPhys.8.82

[BBB+02] J. Bonn, B. Bornschein, L. Bornschein, L. Fickinger and B. Flatt: Results from the Mainz neutrino mass experiment. *Physics of Atomic Nuclei* **65** (2002), 2171.
http://dx.doi.org/10.1134/1.1530296

[BBC+01] F. Boehm, J. Busenitz, B. Cook, G. Gratta and H. Henrikson: Final results from the Palo Verde neutrino oscillation experiment. *Physical Review D* **64** (2001).
http://dx.doi.org/10.1103/PhysRevD.64.112001

[BCF+02] I. Bergström, C. Carlberg, T. Fritioff, G. Douysset, J. Schönfelder and R. Schuch: SMILETRAP—A Penning trap facility for precision mass measurements using highly charged ions. *Nuclear Instruments and Methods in Physics Research Section A: Accelerators, Spectrometers, Detectors and*

Associated Equipment **487** (2002), 618 .
http://dx.doi.org/10.1016/S0168-9002(01)02178-7

[BG86] L. S. Brown and G. Gabrielse: Geonium theory: Physics of a single electron or ion in a Penning trap. *Reviews of Modern Physics* **58** (1986), 233.
http://dx.doi.org/10.1103/RevModPhys.58.233

[Bla06] K. Blaum: High-accuracy mass spectrometry with stored ions. *Physics Reports* **425** (2006), 1 .
http://dx.doi.org/10.1016/j.physrep.2005.10.011

[BM08] B. Becker and P. Molitor: *Technische Informatik: Eine einführende Darstellung* (Oldenbourg Verlag, 2008).

[Bol01] G. Bollen: Mass measurements of short-lived nuclides with ion traps. *Nuclear Physics A* **693** (2001), 3.
http://dx.doi.org/10.1016/S0375-9474(01)00353-0

[Bor05] L. Bornschein: The KATRIN experiment: A direct measurement of the electron antineutrino mass in the sub-eV region. *Nuclear Physics A* **752** (2005), 14c.
http://dx.doi.org/10.1016/j.nuclphysa.2005.02.105

[Bos03] F. Bosch: Schottky mass-and lifetime-spectrometry of unstable, stored ions. *Journal of Physics B: Atomic, Molecular and Optical Physics* **36** (2003), 585.
http://dx.doi.org/10.1088/0953-4075/36/3/316

[Bra11] S. Brandt: *Datenanalyse für Naturwissenschaftler und Ingenieure: Mit statistischen Methoden und Java-Programmen* (Springer-Verlag, 2011). ISBN 978-3-642-37664-1.
http://www.springer.com/springer+spektrum/mathematik/stochastik/book/978-3-642-37663-4

[CBCM05] R. B. Cakirli, D. Brenner, R. Casten and E. Millman: Proton-neutron interactions and the new atomic masses. *Physical Review Letters* **95** (2005), 092501.
http://dx.doi.org/10.1103/PhysRevLett.94.092501

[Cla68] A. Clark: Low temperature thermal expansion of some metallic alloys. *Cryogenics* **8** (1968), 282.
http://dx.doi.org/10.1016/S0011-2275(68)80003-7

[Com14a] Comsol Multiphysics: Comsol Database (2013 – 2014).

[Com14b] Comsol Multiphysics: *Website* (2014).
http://www.comsol.com/

[Cor13] Corning: Macor. *Website* (2013).
http://www.corning.com/specialtymaterials/advanced_optics/specialty_glass_ceramics/products/macor/index.aspx

[CWr64] R. H. Carr, G. K. White and R. D. McCammon: Thermal expansion of copper at low temperatures. *Proceedings of the Royal Society of London. Series A, Mathematical and Physical Sciences* **280** (1964), 72.
http://dx.doi.org/10.1098/rspa.1964.0131

[DBH+11] C. Diehl, K. Blaum, M. Höcker, J. Ketter and D. B. Pinegar: Progress with the MPIK/UW-PTMS in Heidelberg. *Hyperfine Interactions* **199** (2011), 291.
http://dx.doi.org/10.1007/s10751-011-0324-6

[Deh90] H. Dehmelt: Experiments with an isolated subatomic particle at rest. *Reviews of Modern Physics* **62** (1990), 525.
http://dx.doi.org/10.1103/RevModPhys.62.525

[Dem35] A. J. Dempster: New methods in mass spectroscopy. *Proceedings of the American Philosophical Society* **75** (1935), 755.
http://www.jstor.org/stable/984592

[Dem05] W. Demtröder: *Experimentalphysik 3: Atome, Moleküle und Festkörper* (Springer, 2005). ISBN 978-3-642-03911-9.
http://www.springer.com/physics/atomic,+molecular,+optical+%26+plasma+physics/book/978-3-642-03910-2

[Duc50] H. E. Duckworth: A large dempster-type double-focusing mass spectrograph. *Review of Scientific Instruments* **21** (1950), 54.
http://dx.doi.org/10.1063/1.1745422

[Ear42] S. Earnshaw: On the nature of the molecular forces which regulate the constitution of the luminiferous ether. *Transactions of the Cambridge Philosophical Society* **7** (1842), 97.
https://archive.org/details/cbarchive_36266_onthenatureofthemolecularforce1833

[EEH+06] T. Eronen *et al.*: Q Values of the Superallowed β Emitters $^{26}\mathrm{Al}^{m}$, $^{42}\mathrm{Sc}$, and $^{46}\mathrm{V}$ and Their Impact on V_{ud} and the Unitarity of the Cabibbo-Kobayashi-Maskawa Matrix. *Physical Review Letters* **97** (2006), 232501.
http://dx.doi.org/10.1103/PhysRevLett.97.232501

[EEH+08] T. Eronen *et al.*: Q_{EC} Values of the Superallowed β Emitters $^{50}\mathrm{Mn}$ and $^{54}\mathrm{Co}$. *Physical Review Letters* **100** (2008), 132502.
http://dx.doi.org/10.1103/PhysRevLett.100.132502

[Ein05] A. Einstein: Ist die Trägheit eines Körpers von seinem Energieinhalt abhängig? *Annalen der Physik* **323** (1905), 639.
http://dx.doi.org/10.1002/andp.19053231314

[Eki06] J. Ekin: *Experimental Techniques for Low-Temperature Measurements : Cryostat Design, Material Properties and Superconductor Critical-Current Testing* (OUP Oxford, 2006). ISBN 9780191524691.

[EM07] R. H. Enns and G. C. McGuire: *Computer Algebra Recipes* (Springer New York, 2007). ISBN 978-0-387-25768-6.
http://dx.doi.org/10.1007/978-0-387-49333-6

[FFI+01] S. Fukuda *et al.*: Constraints on neutrino oscillations using 1258 days of Super-Kamiokande solar neutrino data. *Physical Review Letters* **86** (2001), 5656.
http://dx.doi.org/10.1103/PhysRevLett.86.5656

[Ger11] V. Gerginov: Time and frequency metrology at PTB: recent results. *Proceedings of SPIE – the International Society For Optical Engineering* **8132** (2011), 81320H.
http://dx.doi.org/10.1117/12.892675

[GN08] R. Glowinski and P. Neittaanmäki: *Partial Differential Equations* (2008). ISBN 978-1-4020-8757-8.
http://dx.doi.org/10.1007/978-1-4020-8758-5

[Gnu14] Gnuplot Documentation. *Website* (2014).
http://www.gnuplot.info

[Gor05] S. Goriely: Global microscopic models for nuclear astrophysics applications. *Nuclear Physics A* **752** (2005), 560.
http://dx.doi.org/10.1016/j.nuclphysa.2005.02.059

[HAA+03] F. Herfurth *et al.*: Mass measurements and nuclear physics – recent results from ISOLTRAP. *Journal of Physics B: Atomic, Molecular and Optical Physics* **36** (2003), 931.
http://dx.doi.org/10.1088/0953-4075/36/5/312

[Hof98] S. Hofmann: New elements – approaching $Z = 114$. *Reports on Progress in Physics* **61** (1998), 639.
http://dx.doi.org/10.1088/0034-4885/61/6/002

[HP49] G. Hanna and B. Pontecorvo: The β-Spectrum of H^3. *Physical Review* **75** (1949), 983.
http://dx.doi.org/10.1103/PhysRev.75.983.3

[Hö10] M. Höcker: Untersuchungen zum Ionentransfer im UW/MPIK Doppel-Penningfallen Experiment. Master Thesis, Heidelberg (2010). http://hdl.handle.net/11858/00-001M-0000-0011-72BA-F

[Hö15] M. Höcker: To be published. PhD Thesis, University of Heidelberg (2015).

[Jac62] J. D. Jackson: *Classical electrodynamics*, Volume 3 (Wiley New York etc., 1962).

[Kar08] S. G. Karshenboim: New recommended values of the fundamental physical constants (CODATA 2006). *Physics Uspekhi* **51** (2008), 1019. http://dx.doi.org/10.1070/PU2008v051n10ABEH006668

[KBB+05] C. Kraus *et al.*: Final results from phase II of the Mainz neutrino mass search in tritium decay. *The European Physical Journal C–Particles and Fields* **40** (2005), 447. http://dx.doi.org/10.1140/epjc/s2005-02139-7

[KBK+95] M. König, G. Bollen, H.-J. Kluge, T. Otto and J. Szerypo: Quadrupole excitation of stored ion motion at the true cyclotron frequency. *International Journal of Mass Spectrometry and Ion Processes* **142** (1995), 95. http://dx.doi.org/10.1016/0168-1176(95)04146-C

[KEH+14] J. Ketter, T. Eronen, M. Höcker, S. Streubel and K. Blaum: First-order perturbative calculation of the frequency-shifts caused by static cylindrically-symmetric electric and magnetic imperfections of a Penning trap. *International Journal of Mass Spectrometry* **358** (2014), 1. http://dx.doi.org/10.1016/j.ijms.2013.10.005

[Ket14] J. Ketter: Bildladungsverschiebung – Eigenfrequenzen, Invarianztheorem und Lock. Internal report (2014).

[KN03] T. Kinoshita and M. Nio: Revised α^4 Term of Lepton $g-2$ from the Feynman Diagrams Containing an Internal Light-By-Light Scattering Subdiagram. *Physical Review Letters* **90** (2003), 021803. http://dx.doi.org/10.1103/PhysRevLett.90.021803

[KT01] T. Kajita and Y. Totsuka: Observation of atmospheric neutrinos. *Reviews of Modern Physics* **73** (2001), 85. http://dx.doi.org/10.1103/RevModPhys.73.85

[Lan23] I. Langmuir: The electron emission from thoriated tungsten filaments. *Physical Review* **22** (1923), 0357. http://dx.doi.org/10.1103/PhysRev.22.357

[LFLM90] J. Lockhart, R. Fagaly, L. Lombardo and B. Muhlfelder: Magnetic susceptibility of instrument materials below 10 K. *Physica B: Condensed Matter* **165 – 166** (1990), 147 . Proceedings of the 19th International Conference on Low Temperature Physics.
http://dx.doi.org/10.1016/S0921-4526(90)80923-7

[Lob03] V. Lobashev: The search for the neutrino mass by direct method in the tritium beta-decay and perspectives of study it in the project KATRIN. *Nuclear Physics A* **719** (2003), C153.
http://dx.doi.org/10.1016/S0375-9474(03)00985-0

[LPT03] D. Lunney, J. Pearson and C. Thibault: Recent trends in the determination of nuclear masses. *Reviews of Modern Physics* **75** (2003), 1021.
http://dx.doi.org/10.1103/RevModPhys.75.1021

[Mye13] E. G. Myers: The most precise atomic mass measurements in Penning traps. *International Journal of Mass Spectrometry* **349** (2013), 107.
http://dx.doi.org/10.1016/j.ijms.2013.03.018

[NFB+06] S. Nagy, T. Fritioff, M. Bjorkhage, I. Bergstrom and R. Schuch: On the Q-value of the tritium beta-decay. *Europhysics Letters* **74** (2006), 404.
http://dx.doi.org/10.1209/epl/i2005-10559-2

[NH14] I. Newton and E. Halley: *Philosophiae naturalis principia mathematica*, Volume 62 (Jussu Societatis Regiae ac typis Josephi Streater, prostant venales apud Sam. Smith, 1714).
https://archive.org/details/philosophiaenat00newt

[OHR34] M. Oliphant, P. Harteck and Lord. E. Rutherford: Transmutation effects observed with heavy hydrogen. *Proceedings of the Royal Society of London. Series A* **144** (1934), 692.
http://dx.doi.org/10.1098/rspa.1934.0077

[Par14] D. S. Parno: The KATRIN experiment: status and outlook. *arXiv* **1307.5289** (2014), 77.
http://arxiv.org/abs/1307.5289

[Pau90] W. Paul: Electromagnetic traps for charged and neutral particles. *Reviews of Modern Physics* **62** (1990), 531.
http://dx.doi.org/10.1103/RevModPhys.62.531

[Pin07] D. Pinegar: Tools for a Precise Tritium to Helium-3 Mass Comparison. PhD Thesis, University of Washington (2007).
http://adsabs.harvard.edu/abs/2007PhDT.......146P

[PKTW01] B. Pfeiffer, K.-L. Kratz, F.-K. Thielemann and W. Walters: Nuclear structure studies for the astrophysical r-process. *Nuclear Physics A* **693** (2001),

282.
http://dx.doi.org/10.1016/S0375-9474(01)01141-1

[Por01] J. V. Porto: Series solution for the image charge fields in arbitrary cylindrically symmetric Penning traps. *Physical Review A* **64** (2001), 023403.
http://dx.doi.org/10.1103/PhysRevA.64.023403

[PTVF92] W. H. Press, S. A. Teukolsky, W. T. Vetterling and B. P. Flannery: *Numerical Recipes in C: The Art of Scientific Computing. Second Edition*, Volume 24 (Cambridge University Press, 1992).
http://dx.doi.org/10.1088/0143-0807/24/3/701

[PvR58] W. Paul, U. von Zahn and H. P. Reinhard: Das elektrische Massenfilter als Massenspektrometer und Isotopentrenner. *Zeitschrift für Physik* **152** (1958), 143.
http://dx.doi.org/10.1007/BF01327353

[PZVDJ07] D. B. Pinegar, S. L. Zafonte and R. S. Van Dyck Jr: The UW-PTMS: Recent measurements and technological progress. *Hyperfine Interactions* **174** (2007), 47.
http://dx.doi.org/10.1007/s10751-007-9563-y

[RAJ54] T. Rubin, H. W. Altman and H. L. Johnston: Coefficients of Thermal Expansion of Solids at Low Temperatures. I. The Thermal Expansion of Copper from 15 to 300° K. *Journal of the American Chemical Society* **76** (1954), 5289.

[RTM+05] S. Rainville *et al.*: A direct test of $E = mc^2$. *Nature* **438** (2005), 1096.
http://dx.doi.org/10.1038/4381096a

[Ryl13] T. Rylander: *Computational Electromagnetics* (Springer, Dordrecht, 2013). ISBN 978-1-4614-5350-5.
http://dx.doi.org/10.1007/978-1-4614-5351-2

[SBB+91] G. Savard *et al.*: A new cooling technique for heavy ions in a Penning trap. *Physics Letters A* **158** (1991), 247.
http://dx.doi.org/10.1016/0375-9601(91)91008-2

[Sch11] M. Schuh: Simulation von elektrostatischen Eigenschaften der THe-Trap Penningfalle. Bachelor Thesis, University of Heidelberg (2011).
http://hdl.handle.net/11858/00-001M-0000-0010-19D3-2

[SEH+14] S. Streubel, T. Eronen, M. Höcker, J. Ketter and M. Schuh: Toward a more accurate Q value measurement of tritium: status of THe-Trap. *Applied Physics. B, Lasers and Optics* **114** (2014), 137.
http://dx.doi.org/10.1007/s00340-013-5669-x

[Spr13] SpringerMaterials: The Landolt-Boernstein Database (2013).
http://www.springermaterials.com

[Str12] S. Streubel: Private communication. B_1 *Determination* (2012).

[Str14] S. Streubel: Kontrolle der Umwelteinflüsse auf THe-Trap am Beispiel der Bestimmung des Massenverhältnisses von Sauerstoff-16 zu Kohlenstoff-12. PhD Thesis, Universität Heidelberg (2014).
http://www.ub.uni-heidelberg.de/archiv/16870

[Stu12] S. Sturm: The g-factor of the electron bound in $^{28}Si^{13+}$. The most stringent test of bound-state quantum electrodynamics. PhD Thesis, Universität Mainz (2012).
http://ubm.opus.hbz-nrw.de/volltexte/2012/3108/

[SW75] L. G. Smith and A. Wapstra: Masses of isotopes of H, He, C, N, O, and F. *Physical Review C* **11** (1975), 1392.
http://dx.doi.org/10.1103/PhysRevC.11.1392

[SWB13] S. Sturm, G. Werth and K. Blaum: Electron g-factor determinations in Penning traps. *Annalen der Physik* **525** (2013), 620.
http://dx.doi.org/10.1002/andp.201300052

[Tho99] J. J. Thomson: On the Masses of the Ions in Gases at Low Pressures. *The Philosophical Magazine* **48** (1899), 547.
http://link.springer.com/article/10.1007%2Fs00897-997-0012-4

[Tre11] M. Tremer: Untersuchung und Optimierung des externen Ladens von Ionen bei THe-Trap. Master Thesis, Universität Heidelberg (2011).
http://hdl.handle.net/11858/00-001M-0000-0012-2FBD-2

[VDJ90] R. S. Van Dyck Jr: (1990). Trap Electrodes Technical Drawing. Internal Notes.

[VDJ91] R. S. Van Dyck Jr: (1991). Labbook.

[VDJFS93] R. S. Van Dyck Jr, D. Farnham and P. Schwinberg: Tritium–helium-3 mass difference using the Penning trap mass spectroscopy. *Physical Review Letters* **70** (1993), 2888.
http://dx.doi.org/10.1103/PhysRevLett.70.2888

[VDJMFS89] R. S. Van Dyck Jr, F. L. Moore, D. L. Farnham and P. B. Schwinberg: Number dependency in the compensated Penning trap. *Physical Review A* **40** (1989), 6308.
http://dx.doi.org/10.1103/PhysRevA.40.6308

[VDJPVLZ06] R. S. Van Dyck Jr, D. Pinegar, S. Van Liew and S. Zafonte: The UW-PTMS: Systematic studies, measurement progress, and future improvements. *International Journal of Mass Spectrometry* **251** (2006), 231 .
http://dx.doi.org/10.1016/j.ijms.2006.01.038

[VL04] S. Van Liew: An ultra-precise determination of the mass of helium-3 using Penning trap mass spectrometry. PhD Thesis, University of Washington, Seattle (2004).
http://adsabs.harvard.edu/abs/2004PhDT.....41V

[WD75] D. Wineland and H. Dehmelt: Principles of the stored ion calorimeter. *Journal of Applied Physics* **46** (1975), 919.
http://dx.doi.org/10.1063/1.321602

[WED73] D. Wineland, P. Ekstrom and H. Dehmelt: Monoelectron Oscillator. *Physical Review Letters* **31** (1973), 1279.
http://dx.doi.org/10.1103/PhysRevLett.31.1279

[Wei35] C. Weizsäcker: Zur Theorie der Kernmassen. *Zeitschrift für Physik A Hadrons and Nuclei* **96** (1935), 431.
http://link.springer.com/article/10.1007%2FBF01337700

[Whi73] G. K. White: Thermal-expansion of reference materials – copper, silica and silicon. *Journal of Physics D* **6** (1973), 2070.
http://dx.doi.org/10.1088/0022-3727/6/17/313

[Wol10] J. Wolf: The KATRIN neutrino mass experiment. *Nuclear Instruments & Methods in Physics Research. Section A, Accelerators, Spectrometers, Detectors and Associated Equipment* **623** (2010), 442.
http://dx.doi.org/10.1016/j.nima.2010.03.030

[WSV14] A. Wouwer, P. Saucez and C. Vilas: *Simulation of ODE/PDE Models with MATLAB®, OCTAVE and SCILAB: Scientific and Engineering Applications* (Springer, 2014).
http://www.springer.com/engineering/control/book/978-3-319-06789-6

Appendix A

Final fit-coefficients

This appendix gives the fit-coefficients S_n, E_n, D_n and R_n with their full statistical precision. The statistical uncertainty is denoted with $()_{\text{stat}}$ and the systematic with $()_{\text{sys}}$. The statistical uncertainty is the standard deviation of the weighted average of the fit-coefficients determined at the five highest resolutions. The systematic uncertainty is derived from violations of the linearity of the Maxwell equations. Further information about the statistical and systematic uncertainty is given in the Sections 4.1.2 and 4.1.3, respectively. The simulation model used is the same as in Section 4.1, including thermal shrinking and fillets at the inner edges of the guard electrodes. All given values have the unit of mm^{-n}, where n is the order of the fit-coefficient. Table A.4 gives the fit-coefficients of a trap geometry without holes in the endcap electrodes. Hence, no S_n are given. But maybe it is useful for other estimates and hence can be found here.

Table A.1: Final fit-coefficients of the electrostatic simulations of the capture trap, with a hole radius of 250 µm in the endcap electrodes.

	Value
S_0	$4.654\,967\,23(14)_{\text{stat}}(1957349)_{\text{sys}} \cdot 10^{-6}$
S_1	$2.470\,682\,456\,1(10)_{\text{stat}}(1543669)_{\text{sys}} \cdot 10^{-6}$
S_2	$3.037\,674\,9(16)_{\text{stat}}(126047)_{\text{sys}} \cdot 10^{-6}$
S_3	$8.411\,426\,88(86)_{\text{stat}}(53648)_{\text{sys}} \cdot 10^{-7}$
S_4	$8.726\,211(90)_{\text{stat}}(35398)_{\text{sys}} \cdot 10^{-7}$
S_5	$2.258\,293\,6(39)_{\text{stat}}(1423)_{\text{sys}} \cdot 10^{-7}$
S_6	$2.242\,22(42)_{\text{stat}}(889)_{\text{sys}} \cdot 10^{-7}$
E_0	$4.170\,518\,088\,424(86)_{\text{stat}}(18161047)_{\text{sys}} \cdot 10^{-1}$
E_1	$1.659\,441\,636\,22(17)_{\text{stat}}(46634)_{\text{sys}} \cdot 10^{-1}$
E_2	$1.098\,722\,203\,1(10)_{\text{stat}}(114064)_{\text{sys}} \cdot 10^{-1}$
E_3	$1.038\,216\,929(15)_{\text{stat}}(1671)_{\text{sys}} \cdot 10^{-2}$
E_4	$2.069\,703\,3(57)_{\text{stat}}(31512)_{\text{sys}} \cdot 10^{-4}$
E_5	$-1.809\,436\,3(68)_{\text{stat}}(426)_{\text{sys}} \cdot 10^{-4}$
E_6	$-2.341\,35(27)_{\text{stat}}(787)_{\text{sys}} \cdot 10^{-5}$
E_7	$9.512\,98(205)_{\text{stat}}(95)_{\text{sys}} \cdot 10^{-6}$
E_8	$-3.920\,3(59)_{\text{stat}}(142)_{\text{sys}} \cdot 10^{-6}$
D_0	$1.135\,580\,853\,5(52)_{\text{stat}}(91577)_{\text{sys}} \cdot 10^{-2}$
D_1	$3.180\,855\,666\,7(12)_{\text{stat}}(417635)_{\text{sys}} \cdot 10^{-3}$
D_2	$-2.459\,313\,7(61)_{\text{stat}}(1120)_{\text{sys}} \cdot 10^{-4}$
D_3	$-6.015\,029\,89(10)_{\text{stat}}(8570)_{\text{sys}} \cdot 10^{-4}$
D_4	$-5.333\,737(34)_{\text{stat}}(63)_{\text{sys}} \cdot 10^{-4}$
D_5	$-3.207\,641\,0(47)_{\text{stat}}(563)_{\text{sys}} \cdot 10^{-5}$
D_6	$2.591\,9(16)_{\text{stat}}(14)_{\text{sys}} \cdot 10^{-5}$
D_7	$6.981\,92(14)_{\text{stat}}(20)_{\text{sys}} \cdot 10^{-6}$
D_8	$2.296(36)_{\text{stat}}(20)_{\text{sys}} \cdot 10^{-6}$
R_0	$5.715\,883\,205\,15(32)_{\text{stat}}(1045153)_{\text{sys}} \cdot 10^{-1}$
R_2	$-1.096\,289\,399\,3(37)_{\text{stat}}(74077)_{\text{sys}} \cdot 10^{-1}$
R_4	$3.256\,313(21)_{\text{stat}}(2111)_{\text{sys}} \cdot 10^{-4}$
R_6	$-2.680\,8(98)_{\text{stat}}(437)_{\text{sys}} \cdot 10^{-6}$
R_8	$1.598\,4(222)_{\text{stat}}(82)_{\text{sys}} \cdot 10^{-6}$

Table A.2: Final fit-coefficients of the electrostatic simulations of the experiment trap, with a hole radius of 200 µm in the endcap electrodes.

	Value
S_0	$7.766\,920\,77(36)_{\text{stat}}(973908)_{\text{sys}} \cdot 10^{-7}$
S_1	$4.116\,722\,773(19)_{\text{stat}}(1148389)_{\text{sys}} \cdot 10^{-7}$
S_2	$5.094\,028\,5(42)_{\text{stat}}(62991)_{\text{sys}} \cdot 10^{-7}$
S_3	$1.412\,236\,34(17)_{\text{stat}}(39171)_{\text{sys}} \cdot 10^{-7}$
S_4	$1.477\,123(23)_{\text{stat}}(1795)_{\text{sys}} \cdot 10^{-7}$
S_5	$3.831\,685\,1(76)_{\text{stat}}(10399)_{\text{sys}} \cdot 10^{-8}$
S_6	$3.839\,0(11)_{\text{stat}}(49)_{\text{sys}} \cdot 10^{-8}$
E_0	$4.171\,838\,695\,273(64)_{\text{stat}}(4043184)_{\text{sys}} \cdot 10^{-1}$
E_1	$1.660\,318\,075\,07(26)_{\text{stat}}(30242)_{\text{sys}} \cdot 10^{-1}$
E_2	$1.099\,576\,820\,91(74)_{\text{stat}}(255099)_{\text{sys}} \cdot 10^{-1}$
E_3	$1.041\,161\,935(23)_{\text{stat}}(1093)_{\text{sys}} \cdot 10^{-2}$
E_4	$2.311\,288\,5(41)_{\text{stat}}(7199)_{\text{sys}} \cdot 10^{-4}$
E_5	$-1.731\,817(10)_{\text{stat}}(28)_{\text{sys}} \cdot 10^{-4}$
E_6	$-1.733\,05(19)_{\text{stat}}(187)_{\text{sys}} \cdot 10^{-5}$
E_7	$1.134\,480(312)_{\text{stat}}(58)_{\text{sys}} \cdot 10^{-5}$
E_8	$-2.545\,3(43)_{\text{stat}}(40)_{\text{sys}} \cdot 10^{-6}$
D_0	$1.135\,216\,317\,0(58)_{\text{stat}}(83161)_{\text{sys}} \cdot 10^{-2}$
D_1	$3.179\,500\,990\,3(18)_{\text{stat}}(411277)_{\text{sys}} \cdot 10^{-3}$
D_2	$-2.482\,813\,5(68)_{\text{stat}}(652)_{\text{sys}} \cdot 10^{-4}$
D_3	$-6.019\,557\,09(16)_{\text{stat}}(8218)_{\text{sys}} \cdot 10^{-4}$
D_4	$-5.340\,307(38)_{\text{stat}}(13)_{\text{sys}} \cdot 10^{-4}$
D_5	$-3.219\,582\,8(72)_{\text{stat}}(474)_{\text{sys}} \cdot 10^{-5}$
D_6	$2.576\,2(18)_{\text{stat}}(24)_{\text{sys}} \cdot 10^{-5}$
D_7	$6.953\,68(22)_{\text{stat}}(11)_{\text{sys}} \cdot 10^{-6}$
D_8	$2.273(40)_{\text{stat}}(35)_{\text{sys}} \cdot 10^{-6}$
R_0	$5.714\,618\,782\,18(26)_{\text{stat}}(1551992)_{\text{sys}} \cdot 10^{-1}$
R_2	$-1.097\,108\,181\,8(30)_{\text{stat}}(115870)_{\text{sys}} \cdot 10^{-1}$
R_4	$3.024\,944(17)_{\text{stat}}(3371)_{\text{sys}} \cdot 10^{-4}$
R_6	$-8.511\,2(80)_{\text{stat}}(845)_{\text{sys}} \cdot 10^{-6}$
R_8	$2.74(18)_{\text{stat}}(28)_{\text{sys}} \cdot 10^{-7}$

Table A.3: Final fit-coefficients of the electrostatic simulations of the experiment trap, with a hole radius of 152 µm in the endcap electrodes without countersink.

	Value
S_0	$6.100\,520\,06(11)_{\text{stat}}(1099466)_{\text{sys}} \cdot 10^{-8}$
S_1	$3.238\,398\,200(13)_{\text{stat}}(2240403)_{\text{sys}} \cdot 10^{-8}$
S_2	$4.016\,230\,9(12)_{\text{stat}}(72245)_{\text{sys}} \cdot 10^{-8}$
S_3	$1.117\,264\,02(11)_{\text{stat}}(76974)_{\text{sys}} \cdot 10^{-8}$
S_4	$1.172\,796\,2(69)_{\text{stat}}(21009)_{\text{sys}} \cdot 10^{-8}$
S_5	$3.055\,196\,9(52)_{\text{stat}}(20861)_{\text{sys}} \cdot 10^{-9}$
S_6	$3.074\,62(32)_{\text{stat}}(544)_{\text{sys}} \cdot 10^{-9}$
E_0	$4.172\,602\,085\,044(19)_{\text{stat}}(4061394)_{\text{sys}} \cdot 10^{-1}$
E_1	$1.660\,823\,655\,26(17)_{\text{stat}}(87531)_{\text{sys}} \cdot 10^{-1}$
E_2	$1.100\,074\,902\,08(23)_{\text{stat}}(252105)_{\text{sys}} \cdot 10^{-1}$
E_3	$1.042\,882\,914(14)_{\text{stat}}(3024)_{\text{sys}} \cdot 10^{-2}$
E_4	$2.454\,329\,9(13)_{\text{stat}}(7169)_{\text{sys}} \cdot 10^{-4}$
E_5	$-1.685\,625\,2(66)_{\text{stat}}(813)_{\text{sys}} \cdot 10^{-4}$
E_6	$-1.365\,707(60)_{\text{stat}}(1870)_{\text{sys}} \cdot 10^{-5}$
E_7	$1.245\,85(20)_{\text{stat}}(20)_{\text{sys}} \cdot 10^{-5}$
E_8	$-1.695\,7(14)_{\text{stat}}(41)_{\text{sys}} \cdot 10^{-6}$
D_0	$1.135\,008\,333\,8(51)_{\text{stat}}(56239)_{\text{sys}} \cdot 10^{-2}$
D_1	$3.178\,719\,253\,0(12)_{\text{stat}}(412749)_{\text{sys}} \cdot 10^{-3}$
D_2	$-2.496\,591\,6(59)_{\text{stat}}(295)_{\text{sys}} \cdot 10^{-4}$
D_3	$-6.022\,238\,10(10)_{\text{stat}}(9114)_{\text{sys}} \cdot 10^{-4}$
D_4	$-5.344\,283\,2(332)_{\text{stat}}(74)_{\text{sys}} \cdot 10^{-4}$
D_5	$-3.226\,766\,2(46)_{\text{stat}}(685)_{\text{sys}} \cdot 10^{-5}$
D_6	$2.563\,39(155)_{\text{stat}}(16)_{\text{sys}} \cdot 10^{-5}$
D_7	$6.936\,377(139)_{\text{stat}}(35)_{\text{sys}} \cdot 10^{-6}$
D_8	$2.221\,7(350)_{\text{stat}}(69)_{\text{sys}} \cdot 10^{-6}$
R_0	$5.713\,896\,250\,91(57)_{\text{stat}}(289609)_{\text{sys}} \cdot 10^{-1}$
R_2	$-1.097\,578\,571\,0(67)_{\text{stat}}(23674)_{\text{sys}} \cdot 10^{-1}$
R_4	$2.889\,889(37)_{\text{stat}}(711)_{\text{sys}} \cdot 10^{-4}$
R_6	$-1.197\,7(17)_{\text{stat}}(14)_{\text{sys}} \cdot 10^{-5}$
R_8	$-5.41(39)_{\text{stat}}(25)_{\text{sys}} \cdot 10^{-7}$

Table A.4: Final fit-coefficients of the electrostatic simulations of the experiment trap without a hole in the endcap electrodes.

	Value
E_0	$4.173\,199\,428\,872\,4(70)_{\text{stat}}(174955)_{\text{sys}} \cdot 10^{-1}$
E_1	$1.661\,223\,441\,58(15)_{\text{stat}}(518)_{\text{sys}} \cdot 10^{-1}$
E_2	$1.100\,467\,924\,537(82)_{\text{stat}}(220)_{\text{sys}} \cdot 10^{-1}$
E_3	$1.044\,260\,217\,0(127)_{\text{stat}}(99)_{\text{sys}} \cdot 10^{-2}$
E_4	$2.568\,908\,23(46)_{\text{stat}}(103)_{\text{sys}} \cdot 10^{-4}$
E_5	$-1.648\,036\,60(584)_{\text{stat}}(11)_{\text{sys}} \cdot 10^{-4}$
E_6	$-1.065\,985\,7(214)_{\text{stat}}(18)_{\text{sys}} \cdot 10^{-5}$
E_7	$1.338\,383\,6(1774)_{\text{stat}}(15)_{\text{sys}} \cdot 10^{-5}$
E_8	$-9.860\,93(481)_{\text{stat}}(19)_{\text{sys}} \cdot 10^{-7}$
D_0	$1.134\,842\,449\,6(45)_{\text{stat}}(43021)_{\text{sys}} \cdot 10^{-2}$
D_1	$3.178\,099\,216\,9(10)_{\text{stat}}(404445)_{\text{sys}} \cdot 10^{-3}$
D_2	$-2.507\,578\,2(53)_{\text{stat}}(76)_{\text{sys}} \cdot 10^{-4}$
D_3	$-6.024\,372\,551(89)_{\text{stat}}(76284)_{\text{sys}} \cdot 10^{-4}$
D_4	$-5.347\,469(30)_{\text{stat}}(37)_{\text{sys}} \cdot 10^{-4}$
D_5	$-3.232\,593\,1(41)_{\text{stat}}(434)_{\text{sys}} \cdot 10^{-5}$
D_6	$2.556\,2(14)_{\text{stat}}(11)_{\text{sys}} \cdot 10^{-5}$
D_7	$6.922\,028(124)_{\text{stat}}(55)_{\text{sys}} \cdot 10^{-6}$
D_8	$2.270(31)_{\text{stat}}(75)_{\text{sys}} \cdot 10^{-6}$
R_0	$5.713\,315\,411\,56(45)_{\text{stat}}(32409)_{\text{sys}} \cdot 10^{-1}$
R_2	$-1.097\,960\,328\,6(52)_{\text{stat}}(57)_{\text{sys}} \cdot 10^{-1}$
R_4	$2.778\,601(29)_{\text{stat}}(34)_{\text{sys}} \cdot 10^{-4}$
R_6	$-1.490\,3(14)_{\text{stat}}(11)_{\text{sys}} \cdot 10^{-5}$
R_8	$-1.285(31)_{\text{stat}}(76)_{\text{sys}} \cdot 10^{-6}$

Appendix B

Multidimensional least square fit

This appendix introduces the fit algorithm used for fitting the results of the electrostatic simulations (see Section 4) and quantifying the higher-order Legendre terms. Due to the lack of suitable tools for fitting multidimensional Legendre polynomials as Equation (2.13), an own fit routine is developed. The code is based on ideas from Reference [Bra11]. It should be noted that the evaluated Legendre polynomials are scalars, but with two variables z and ρ. For the self coded fitting routine, the least square method is chosen. The principal idea of the least square fit is that the squared distance between the points and the fit function is minimized. The fit functions $f_j\left(\vec{x}\right)$ can be arbitrary and take note that the function itself will not be changed during the process, only the coefficient in front the function are determined. Hence, even complicated functions can be chosen for fitting and it is still a linear fit concerning the coefficients. The index j denotes one of the applied fit functions. In one fit, many functions can be chosen. The full fit function is given by

$$g(\vec{x}_i) = \sum_{j=1}^{m} c_j f_j(\vec{x}_i) \quad , \tag{B.1}$$

where m is the number of chosen individual functions f_j, and c_j are the coefficients of the fit function which need to be determined The sum over the squared distance

between the points and the full fit function $g(\vec{x}_i)$ is

$$\chi^2 = \sum_{i=1}^{n} w_i \left(g(\vec{x}_i) - y_i\right)^2 \quad , \tag{B.2}$$

where n is the total number of points in the fit, y_i is the measured data at position $\vec{x}_i$. It is not necessary that it denotes the order of the function. The parameter w_i is a weight factor and defined as $w_i = \frac{1}{\sigma_{y_i}^2}$, where σ_{y_i} is the standard deviation of y_i.
In the least square fit the squared distance must be minimized:

$$\frac{\partial \chi^2}{\partial c_k} \stackrel{!}{=} 0 \Rightarrow \sum_{j=1}^{m} c_j \sum_{i=1}^{n} w_i f_j(\vec{x}_i)\, f_k(\vec{x}_i) = \sum_{i=1}^{n} w_i y_i f_k(x_i) \quad . \tag{B.3}$$

Equation (B.3) is a linear Equation system (hereafter LES), where c_j are the unknown variables. This LES needs to be solved and for that, a shorter notation is introduced

$$a_{k,j} = \sum_{i=1}^{n} w_i f_j(\vec{x}_i)\, f_k(\vec{x}_i) = (A)_{k,j} \tag{B.4}$$

$$b_k = \sum_{i=1}^{n} w_i y_i f_k(\vec{x}_i) \tag{B.5}$$

$$c_j = (\vec{c})_j \quad . \tag{B.6}$$

Equation (B.4) is called fitmatrix from now on. With these new notations (Equations (B.4), (B.5) and (B.6)), the LES is rewritten as

$$A \cdot \vec{c} = \vec{b} \Leftrightarrow \vec{c} = A^{-1} \cdot \vec{b} \quad , \tag{B.7}$$

where A is a $m \times m$-matrix. From Equation (B.7) it turns out that the coefficients of the fit functions are:

$$c_j = \sum_{k=1}^{m} a_{j,k}^{-1} b_k \quad , \tag{B.8}$$

and they can be calculated by inverting the fitmatrix (see Equation (B.4)).

B.1 Uncertainty calculation

The uncertainty calculation of the fit is based on the idea how much the coefficient c_j changes if y_l is varied. For this, c_j is derived with respect to y_l

$$\frac{\partial c_j}{\partial y_l} = \sum_{k=1}^{m} a_{j,k}^{-1} \frac{\partial b_k}{\partial y_l} = \sum_{k=1}^{m} a_{j,k}^{-1} w_l f_k(x_l) \quad . \tag{B.9}$$

For the uncertainty, it is now necessary to calculate the covariance matrix which is defined as

$$\operatorname{cov}(c_i, c_j) = \sum_{l=1}^{n} \frac{\partial c_i}{\partial y_l} \frac{\partial c_j}{\partial y_l} \sigma_{y_l}^2 \quad . \tag{B.10}$$

Inserting Equation (B.10) in Equation (B.9) leads, after some transformations, to

$$\operatorname{cov}(c_i, c_j) = a_{i,j}^{-1} \Rightarrow \sigma_{c_i} = \sqrt{a_{i,i}^{-1}} \quad . \tag{B.11}$$

In the simulations, the error of y_i is unknown, but it can be assumed that the error is constant for all y_i. The error will be chosen so that the reduced χ^2 which is $\frac{\chi^2}{ndf}$, is equal to one because then the fit is statistically optimal. *ndf* stands for the number of degrees of freedom and is the number of individual fit coefficients m, see Equation (B.1) subtracted from the number of fit points n, see Equation (B.2), so $ndf = n - m$. For this again a new notation is introduced, assuming that the weight factor w is the same for all $\vec{x}_i$

$$\chi^2 = w \sum_{i=1}^{n} \left(g(\vec{x}_i) - y_i \right)^2 \equiv w D^2 \quad , \tag{B.12}$$

$$\tilde{A} = \sum_{i=1}^{n} f_j(x_i) f_k(x_i) \equiv \frac{A}{w} \quad , \tag{B.13}$$

$$\tilde{b}_k = \sum_{i=1}^{n} y_i f_k(x_i) \equiv \frac{b_k}{w} \quad . \tag{B.14}$$

If the reduced χ^2 should be equal to one, then

$$\chi^2 = wD^2 \stackrel{!}{=} ndf \Rightarrow w = \frac{ndf}{D^2} \quad . \tag{B.15}$$

The weight factor w is set, so that the fit is best. This is a reasonable choice in this case because the fit functions are Legendre polynomials. They are the solution of the simulated cases and hence should be the best fit for the problem. Based on this optimization of the weight, the uncertainty of the determined fit-coefficients can be calculated as

$$A^{-1} = \frac{1}{w}\tilde{A}^{-1} = \frac{D^2}{ndf}\tilde{A}^{-1} \quad , \tag{B.16}$$

$$\Rightarrow \mathrm{cov}\left(c_i, c_j\right) = \frac{D^2}{ndf}\tilde{a}^{-1}_{i,j} \quad , \tag{B.17}$$

$$\Rightarrow \sigma_{c_i} = \sqrt{\mathrm{cov}\left(c_i, c_i\right)} = \sqrt{\frac{D^2}{ndf}\tilde{a}^{-1}_{i,i}} \tag{B.18}$$

Hence, the fit error of the coefficients is calculated by Equation (B.18).

Acknowledgment

Obviously, this thesis would not have been possible without support from others. First, I want to thank my supervisor Prof. Dr. Klaus Blaum. Klaus, you gave me the chance to join the experiment and made it possible that I could prepare in parallel for the Paralympics in London 2012. The indescribable flexibility in time of my work at the MPIK is unique in the world of sport. Here, I want to thank the whole THe-Trap group, which supports the combination of high level sport and research.

Huge thanks to Dr. Tommi Eronen. Without him it would have been impossible to design the Faraday cup and to characterize the Penning-ion source so quickly. Also, he corrected my first attempts of writing this thesis and his corrections helped immensely to improve my thesis.

Thanks to Jochen Ketter. He read my thesis a little later and he helped me to improve it even further. Without him some inconsistencies in the simulation of the image charge effect would have not been solved on time. But mainly, he made the connection between the simulation results and the frequencies which are measured in the experiment.

Thanks to Dr. Sebastian Streubel for the introduction to the experiment and the always valuable second opinion.

Thanks to Martin Höcker who I bother with my beginner's questions until today and after my daily training I sometimes do not understand the explanations as quickly as I should.

Thanks to Stiftung Deutsche Sporthilfe for supporting me with the Deutsche Bank Sport-Stipendium during my studies.

Erklärung

Ich versichere, dass ich diese Arbeit selbstständig verfasst und keine anderen als die angegebenen Quellen und Hilfsmittel benutzt habe.

Heidelberg, 31.10.2014, ...